



Doctoral Thesis

Gravity-driven perfusion systems for the physiological culturing of arrays of microtissues

Author(s):

Lohasz, Christian

Publication Date:

2020

Permanent Link:

<https://doi.org/10.3929/ethz-b-000419480> →

Rights / License:

[In Copyright - Non-Commercial Use Permitted](#) →

This page was generated automatically upon download from the [ETH Zurich Research Collection](#). For more information please consult the [Terms of use](#).

DISS. ETH NO. 26595

***GRAVITY-DRIVEN PERFUSION SYSTEMS FOR THE
PHYSIOLOGICAL CULTURING OF ARRAYS OF
MICROTISSUES***

A thesis submitted to attain the degree of
DOCTOR OF SCIENCES of ETH ZURICH
(Dr. sc. ETH Zurich)

presented by
CHRISTIAN LOHASZ
M.Sc. Biological Sciences, University of Konstanz

born on 01.02.1990

citizen of

Germany

accepted on the recommendation of

Prof. Dr. Andreas Hierlemann

Prof. Dr. Petra S. Dittrich

Dr. Olivier Frey

2020

ABSTRACT

This thesis focuses on the design, realization and application of gravity-driven microfluidic systems to create a physiological culture environment for the experimentation with 3D microtissues. As the pharmaceutical industry is facing a prediction dilemma in substance testing, new testing methods are required to bridge the gap between conventional 2D cell culture methods, animal testing, and human physiology. Advanced 3D cell culture techniques in combination with microfluidic technology bear the potential to increase the predictive power of preclinical testing methods and to better characterize the effects of substances on the human organism. However, such systems have yet to be adapted to industrial requirements in terms of material properties, user-friendliness, and experimental throughput. In this thesis, two gravity-driven chip systems and the respective proof-of-concept applications are presented:

- (i) A scalable, polystyrene-based microfluidic chip was used for combining multiple tissue types in an *in vitro* system. Primary human liver microtissues and colon cancer microtissues were cultured together and fluidically connected through cell culture medium. Upon co-administration of anticancer therapeutics and other compounds, liver-related drug-drug interactions were detected.
- (ii) Dynamically changing dosing curves were generated by applying a specific microfluidic channel layout. Colon cancer microtissues were exposed to physiologically-relevant pharmacokinetic dosing curves, and their time-dependent response was assessed.

By relying on standardized 3D microtissues and gravity-driven perfusion, the systems presented in this thesis are scalable, robust, and easy to use so that a transfer to industrial settings is conceivable. The overall goal is to devise *in vitro* systems that closely mimic human physiology.

ZUSAMMENFASSUNG

Diese Dissertation befasst sich mit der Konzipierung, der Realisierung und der Anwendung von Mikrofluidiksystemen, die mit Hilfe der Schwerkraft perfundiert werden und physiologische Kulturbedingungen für das Experimentieren mit 3D-Mikrogewebe schaffen. Da in der pharmazeutischen Industrie die Effekte neuer Substanzen aktuell nur schwer prognostiziert werden können, sind innovative Testmethoden erforderlich, um die Lücken zwischen herkömmlichen 2D-Zellkulturmethoden, Tierversuchen und der Physiologie des Menschen zu schließen. Die Kombination von hochentwickelten 3D-Zellkulturtechniken mit mikrofluidischen Technologien hat das Potential, die Vorhersagekraft präklinischer Testmethoden zu erhöhen und die Auswirkungen neuer Substanzen auf den menschlichen Organismus besser zu charakterisieren. Solche Systeme müssen jedoch hinsichtlich Materialeigenschaften, Benutzerfreundlichkeit und experimentellem Durchsatz noch an die industriellen Anforderungen angepasst werden. In dieser Dissertation werden zwei Chipsysteme, in denen der Medienfluss schwerkraftgetrieben ist, und deren Anwendungen vorgestellt:

- (i) Ein mikrofluidischer Chip auf Polystyrolbasis wurde hergestellt und charakterisiert, in dem mehrere Gewebetypen *in vitro* durch mikrofluidische Kanäle verbunden wurden. Humane Leber-Mikrogewebe aus Primärmaterial und Darmkrebs-Mikrogewebe wurden zusammen kultiviert und kommunizierten durch das gemeinsame Zellkulturmedium. Nach der Verabreichung von Kombinationen aus Krebsmedikamenten und anderen Substanzen wurden leberabhängige Arzneimittel-Wechselwirkungen detektiert.
- (ii) Die mikrofluidische Kanalstruktur wurde dann verändert, so dass dynamische Dosierungsprofile erzeugt werden konnten. Darmkrebs-Mikrogewebe wurden physiologisch relevanten pharmakokinetischen Dosierungskurven ausgesetzt, und ihre zeitabhängige Reaktion wurde erfasst.

Durch die Verwendung standardisierter 3D-Mikrogewebe und Schwerkraft-basierter Perfusion sind die in dieser Dissertation vorgestellten Systeme skalierbar, robust und einfach zu bedienen

und können dazu benutzt werden, in einer industriellen Umgebung *in vitro* Experimente durchzuführen, die der menschlichen Physiologie nahe kommen.

ACKNOWLEDGEMENTS

I want to thank Prof. Andreas Hierlemann for the opportunity to conduct my PhD in his Bio Engineering Laboratory. His scientific support and his encouragement to share ideas and results with other scientists in the field made these past years a very valuable experience. Moreover, I am grateful for the freedom to develop and follow up ideas and to engage in collaborations with partners outside the group.

I am grateful to Dr. Olivier Frey and Dr. Kasper Renggli for their supervision throughout the years. I want to thank them for introducing me (a biologist) to the field of microfluidic engineering – which I remember being initially not too easy. Plenty of fruitful discussions and troubleshooting finally resulted in a successful outcome, which would not have been possible without them.

Special thanks goes to Flavio Bonanini, who pushed the progress of this work forward during his master project.

I also want to thank all the people of the BEL, who made the daily lab work more enjoyable. I want to thank them for their support and discussions in meetings and during coffee breaks. The variety of different scientific backgrounds of the group members always fostered out-of-the-box ideas and made it very interesting to be a part of the group.

A big thank also goes to all members of the D-BSSE facilities and administration, who were always very helpful with technical and organizational issues.

A very big and special thank goes to my non-scientific counterpart in life, which is my family. Especially, I want to thank my wife Lea and my daughter Helena for always being supportive and for providing a healthy amount of distraction at the end of a day in the lab. Further, I want to extend my thanks to my parents, Alexandra and Paul, and my sister Alica for their support. Without all these people, I would not be where I am today.

AUTHOR CONTRIBUTIONS

Flavio Bonanini

Chapter 3: Co-developed the chip application, planned and performed experiments, analyzed data and contributed to the manuscript.

Chapter 4: Fabricated chips and performed experiments.

Dr. Olivier Frey

Chapter 2-4: Conceived and developed the microfluidic chip used in chapters 2 and 3. For chapter 4 he devised the Y-junction concept for temporally varying nonlinear concentration changes. He helped through general consulting and guidance and revised and edited all enclosed manuscripts.

Prof. Dr. Andreas Hierlemann

Chapter 2-4: Helped through consulting and guidance and revised and edited all chapters of this thesis.

Christian Lohasz

Chapter 2: Co-developed the chip setup for robust operation. Planned and performed all experiments, analyzed the data and wrote the manuscript.

Chapter 3: Co-developed the chip application, planned and performed experiments, analyzed data and wrote the manuscript.

Chapter 4: Developed the microfluidic chip for temporal concentration gradients. Designed and fabricated the device, planned and performed experiments, analyzed the data and wrote the manuscript.

Dr. Kasper Renggli

Chapter 2-4: Helped through general consulting and guidance and revised and edited all enclosed manuscripts.

Nassim Rousset

Chapter 2: Ran computational simulations of the flow characteristics in the chip and contributed to the manuscript.

CONTENTS

1	INTRODUCTION	4
1.1	CURRENT GAPS IN DRUG DISCOVERY AND DEVELOPMENT	4
1.2	3D CELL CULTURE AND 3D MICROTISSUES	5
1.3	MICROPHYSIOLOGICAL MULTI-ORGAN SYSTEMS	6
1.4	SCOPE AND STRUCTURE OF THIS THESIS	8
1.5	SUMMARY OF MAJOR RESULTS	9
1.6	REFERENCES.....	11
2	SCALABLE MICROFLUIDIC PLATFORM FOR FLEXIBLE CONFIGURATION OF AND EXPERIMENTS WITH MICROTISSUE MULTIORGAN MODELS.....	15
2.1	ABSTRACT	16
2.2	INTRODUCTION	16
2.3	MATERIALS AND METHODS	19
2.3.1	<i>Microfluidic chip design.....</i>	<i>19</i>
2.3.2	<i>Chip loading and operation</i>	<i>21</i>
2.3.3	<i>Flow rate measurements</i>	<i>23</i>
2.3.4	<i>Computational modeling.....</i>	<i>23</i>
2.3.5	<i>Absorption experiments.....</i>	<i>24</i>
2.3.6	<i>Oxygen measurements.....</i>	<i>24</i>
2.3.7	<i>Cell culture.....</i>	<i>25</i>
2.3.8	<i>Biochemical assays</i>	<i>26</i>
2.3.9	<i>Imaging.....</i>	<i>26</i>
2.4	RESULTS AND DISCUSSION	26
2.4.1	<i>Material properties</i>	<i>26</i>
2.4.2	<i>Operation by tilting</i>	<i>29</i>
2.4.3	<i>The Standing Drop Port and MT compartment</i>	<i>33</i>
2.4.4	<i>On-chip microtissue culture.....</i>	<i>38</i>
2.5	CONCLUSION	42
2.6	ACKNOWLEDGEMENTS	43
2.7	SUPPORTING INFORMATION	43
2.7.1	<i>Supplementary Figures</i>	<i>44</i>
2.7.2	<i>Supplementary Movies</i>	<i>48</i>

2.8	REFERENCES.....	49
3	PREDICTING METABOLISM-RELATED DRUG-DRUG INTERACTIONS USING A MULTI-TISSUE MICROPHYSIOLOGICAL SYSTEM.....	52
3.1	ABSTRACT	53
3.2	INTRODUCTION	53
3.3	MATERIALS AND METHODS.....	56
3.3.1	<i>Cell culture</i>	56
3.3.2	<i>Microfluidic chip operation</i>	56
3.3.3	<i>Drug treatment of microtissues</i>	57
3.3.4	<i>Biochemical assays</i>	58
3.3.5	<i>CYP activity measurements</i>	58
3.3.6	<i>Imaging</i>	58
3.3.7	<i>Mass Spectrometry</i>	59
3.3.8	<i>Statistics</i>	59
3.4	RESULTS	59
3.4.1	<i>Microfluidic chip system</i>	59
3.4.2	<i>Characterization of microtissue models</i>	60
3.4.3	<i>Interaction of multiple organs on chip</i>	63
3.4.4	<i>In vitro prediction of drug-drug interactions</i>	65
3.5	DISCUSSION	68
3.5.1	<i>Metabolic competence of the liver in the testing system</i>	69
3.5.2	<i>Tumor as drug target tissue and multi-tissue configuration</i>	70
3.5.3	<i>Identification of DDIs between IFF and RTV</i>	71
3.5.4	<i>Potential of the testing system</i>	74
3.6	CONCLUSION	76
3.7	ACKNOWLEDGEMENTS	76
3.8	SUPPORTING INFORMATION	76
3.9	REFERENCES.....	85
4	TUBING-FREE MICROFLUIDIC CULTURE SYSTEM FEATURING GRADUAL, IN VIVO-LIKE SUBSTANCE EXPOSURE PROFILES	90
4.1	ABSTRACT	91
4.2	INTRODUCTION	91
4.3	MATERIALS AND METHODS.....	94
4.3.1	<i>Design principle</i>	94

4.3.2	<i>Chip fabrication</i>	97
4.3.3	<i>Device operation</i>	98
4.3.4	<i>Measurements of concentration curves</i>	99
4.3.5	<i>Cell culturing</i>	100
4.3.6	<i>Dosing experiments</i>	100
4.3.7	<i>Biochemical assays</i>	101
4.3.8	<i>Imaging</i>	101
4.4	RESULTS	102
4.4.1	<i>Modulation of the concentration profile</i>	102
4.4.2	<i>Design integration into a microfluidic microtissue culture chip</i>	104
4.4.3	<i>Concentration profile characterization</i>	106
4.4.4	<i>Dosing experiments</i>	108
4.5	DISCUSSION	110
4.5.1	<i>Future Perspective</i>	111
4.6	CONCLUSION	112
4.7	ACKNOWLEDGEMENTS	113
4.8	SUPPORTING INFORMATION	114
4.8.1	<i>Supplementary Figures</i>	114
4.8.2	<i>Supplementary Movies</i>	118
4.9	REFERENCES	119
5	CONCLUSION	122
6	OUTLOOK	126

1 INTRODUCTION

1.1 Current gaps in drug discovery and development

Today's drug discovery and development is a highly inefficient process that requires approx. 5,000 potential drug candidates, 10 – 12 years of development time, and \$2.5 billion to obtain a single FDA-approved drug.¹ These high costs are mostly related to the high attrition rates of compounds that reveal their inefficacy or toxicity during the clinical trial phases (Figure 1). The expenses in all clinical trial phases in drug development sum up to approx. 70 % of the entire costs to launch a drug. To render the drug development process more efficient, compounds and their mode of action need to be better characterized, so that inefficient or toxic compounds can be eliminated already during early drug discovery and at preclinical stages.^{2,3} The gold standard for the initial characterization of novel compounds includes conventional *in vitro* 2D cell-culture techniques and *in vivo* animal studies. 2D culture models are well established and scalable, and, therefore, provide an inexpensive tool to perform a broad compound screening. However, 2D models, grown on a hard plastic surface, do not represent key features of organ physiology, e.g., the complex 3D tissue architecture. Moreover, those simple models usually do not include multiple cell types and do not include interconnection and communication between different tissue types.⁴

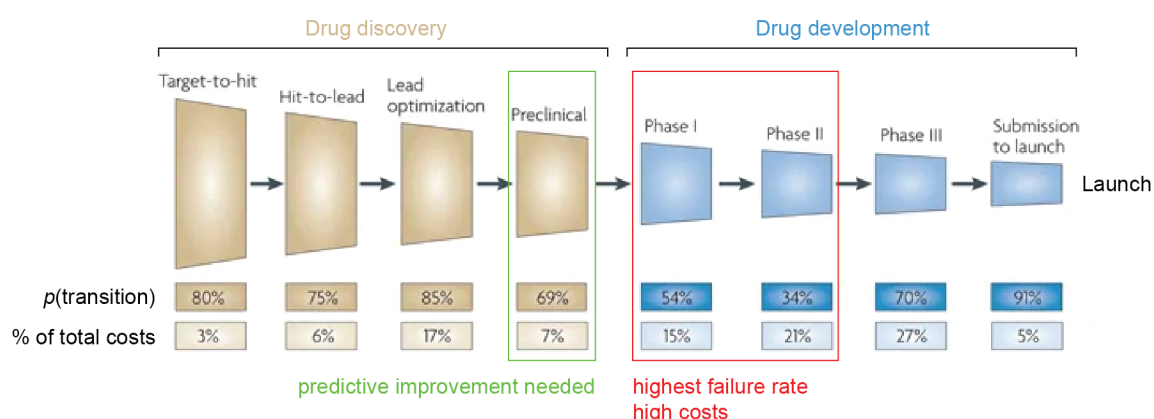


Figure 1: Illustration of the drug discovery and development pipeline. Numbers in boxes at the bottom indicate the probability of a substance to transition from one stage to the next ($p(\text{transition})$), and the percentage of costs for each stage for bringing a substance through the overall process and to the market. As the failure rate is highest during the expensive clinical phase I and phase II trials (red), there is a need for a predictive improvement at preclinical stages (green) to reduce development costs. The figure was adapted and modified from Paul, Mytelka.²

Animal experimentation offers insights into the complex organ-interplay on a whole-organism level. Nevertheless, inter-species differences, especially in disease-related pathways, limit their translatability to human physiology and, thus, their predictive value.⁵ Given the low predictive power of current compound testing strategies, there is a clear need for more representative, human-cell- or tissue-based methods for implementation in preclinical drug discovery.

1.2 3D cell culture and 3D microtissues

3D cell-culture techniques are considered a promising approach to overcome the limitations of conventional cell culture methods in well plates or Petri dishes. 3D techniques are aimed at mimicking human organs by arranging the necessary organ-specific cell types in a physiologically relevant architecture. The methods to create 3D organ constructs range from precisely controlled bioprinting approaches to self-organizing multicellular structures.⁶⁻⁸ Most 3D cell culturing techniques require scaffolds, such as hydrogels^{6, 9} and porous membranes¹⁰ that support the orientation of cells in an organotypic architecture. However, by using scaffolds the *in vitro* cells or organs are firmly embedded in the respective culturing platform, so that analysis methods have to be adapted to these specific platforms. One well-established, scaffold-free 3D model consists of spherical microtissues (MTs). 3D MTs can be generated by transferring suspended primary cells or immortalized cells into hanging drops,¹¹ or into ultra-low adhesion microwells.¹² Both methods prevent that cells attach to a substrate and promote cell-cell interaction. Within few days, cells adhere to each other and self-organize into spherical constructs. This allows for the generation of a wide range of different human *in vitro* organ models with tissue-specific architecture and functions.¹³⁻¹⁶ The absence of artificial scaffolds, e.g., hydrogels or porous membranes, in 3D MTs facilitates their straightforward handling, analysis, and transfer for use with other culturing platforms.

A prime example of a widely used type of 3D MT is the liver. Liver MTs consisting of primary human hepatocytes have been shown to maintain their organotypic functionality over extended time periods in culture.^{17, 18} Furthermore, liver MTs representing specific diseased states were shown to be a valuable tool to study drug efficacy *in vitro*.^{19, 20} Tumor MTs represent another commonly used type of 3D MTs. They feature *in vivo*-like oxygen and nutrient gradients within the tissue and are, therefore, more representative than 2D monolayers of cancer cells.²¹ The complexity of tumor MTs depends on the cell types that are used for their formation. Cell line-based MTs can be formed in monoculture or in co-culture with cancer-associated fibroblasts

for compound screenings.^{22, 23} Alternatively, patient-derived primary cells can be used to study personalized responses to drug treatment using a set of patient-derived 3D constructs.²⁴ The physiological relevance of 3D MTs in combination with their robust and scalable production in standardized well-plate formats render them a tool that is well-suited for implementation in industrial settings.²²

1.3 Microphysiological multi-organ systems

To fully exploit the physiological characteristics of advanced 3D cell-culture models, such 3D models are increasingly used in combination with microfluidic technology. So-called microphysiological systems (MPS) can be used to precisely control the microenvironment of cellular constructs *in vitro* by providing mechanical cues and architectural support, and by the precise spatiotemporal control of the delivery of soluble molecules.²⁵ Over the last years, a tremendous number of MPS have been published, which included a broad range of different approaches to culture solid tissues (e.g., white adipose tissue; Figure 2A),^{26, 27} barrier tissues (e.g., lung, Figure 2B),^{10, 28} or multiple interconnected tissues (e.g., intestine-skin-liver-kidney, Figure 2C).²⁹⁻³¹ In particular multi-organ systems offer the potential to capture complex physiological processes or disease mechanisms that rely on the interaction of several organs.³² 3D spherical MTs provide suitable building blocks and organ components in multi-organ MPSs.^{33, 34} Their scaffold-free nature allows for robust off-chip generation, maturation, and enables to perform a quality-control step before transfer into the MPS. The possibility to harvest 3D MTs from the MPS after the experiment allows for organ-specific downstream analyses.

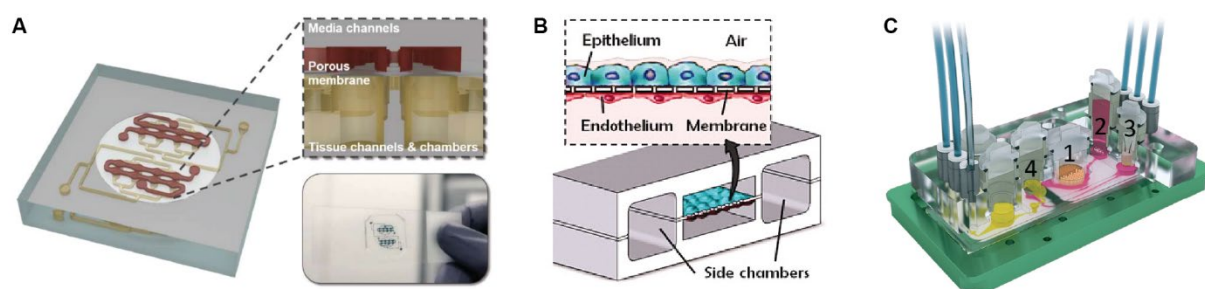


Figure 2: Examples of different MPS concepts. **(A)** White adipose tissue chip as a representative solid-tissue chip. Figure adapted and modified from Rogal et. al.²⁷ **(B)** Lung chip as a representative barrier-tissue chip. Figure adapted and modified from Huh et. al.¹⁰ **(C)** 4-organ chip including intestinal, skin, liver and kidney tissue as a representative multi-organ chip. Figure adapted and modified from Maschmeyer et. al.³¹

Furthermore, the similar shape and size of microtissues across most tissue types facilitates the design of flexible platforms, which can be used for culturing of different MT types.

To manufacture MPS, several materials can be used, among which poly(dimethylsiloxane) (PDMS) is most prominently used for academic devices.³⁵ The elastic material allows for straightforward chip fabrication using standard soft-lithography methods at micrometer resolutions. However, disadvantages of PDMS include the ad- and absorption of hydrophobic substances in the soft polymer material and a comparably low fabrication throughput, so that thermoplastic materials are preferably used to manufacture MPS. Polystyrene (PS) is a thermoplastic material, which is commonly used to manufacture cell-culture equipment, e.g., microwell plates and culture dishes. PS is well-characterized for use with biological material and features significantly lower absorption than PDMS.³⁶ Furthermore, PS devices can be produced at high throughput and with high reproducibility at low costs by using injection molding. PS-based MPS are well-suited for standard screening scenarios in the pharmaceutical industry.

There is a plethora of approaches to actuate flow and to supply nutrients to the cells and microtissues in microfluidic systems.³⁷ Flow actuation can be categorized into active and passive perfusion methods. Active perfusion is initiated using pneumatic,²⁶ syringe,³⁸ or peristaltic pumps,³⁹ or by centrifugation of the platform⁴⁰ and relies on the use of external precision equipment with the cell culturing platform. Passive perfusion, in contrast, makes use of physical properties of liquids, such as capillary forces,⁴¹ surface tension,⁴² and hydrostatic pressure differences⁴³⁻⁴⁶ to achieve flow. Exploiting gravity for perfusion of MPSs proved to be an effective and user-friendly option. Gravity-driven flow is achieved by tilting of the platform to induce a height difference between the inlet and outlet reservoirs of a microfluidic channel

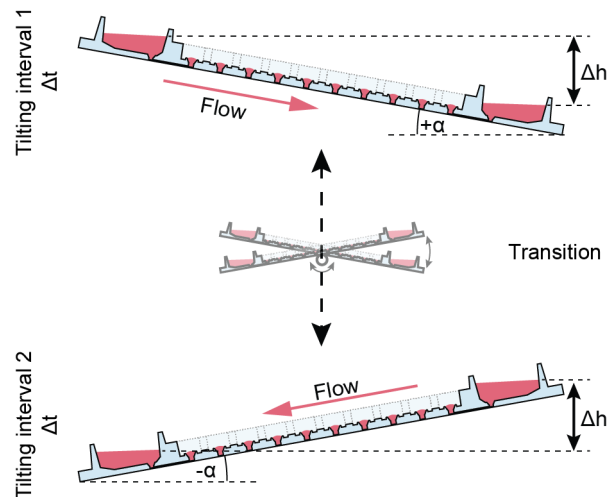


Figure 3: Gravity-driven flow is actuated by tilting of a microfluidic chip by an angle, α . The height difference, Δh , between the reservoirs at both ends of the channel results in a hydrostatic pressure difference, so that the medium flows from the upper reservoir to the lower reservoir. Continuous flow is achieved by repeated tilting.

Figure 3).^{43, 44} The resulting hydrostatic pressure difference between the two ends of the channel then drives the liquid from the upper reservoir to the lower reservoir. The flow speed and flow configuration can be controlled by applying distinct channel designs, e.g., by modifying flow resistance and connections to reservoirs or by altering the hydrostatic pressure difference between inlet and outlet.^{45, 46} The use of gravity-driven flow obviates the need for expert knowledge on how to connect and operate expensive and complex off-chip equipment, such as precision pumps. Furthermore, parallelization of experiments is straightforward, as a number of identical chips, or chips arranged in plates, can be stacked on the same tilting platform to obtain the same experimental flow conditions in all channels. The technology of gravity-driven flow actuation as well as the respective MPSs can be easily transferred to labs that do not possess sophisticated microfluidic and pumping equipment and to industrial settings.

1.4 Scope and structure of this thesis

This thesis focuses on the development, characterization, and application of gravity-driven microfluidic systems that enable the culturing and interconnection of 3D microtissues. First, a scalable, polystyrene-based microfluidic chip was described and characterized. Second, this chip was used to study drug-drug interactions in a liver-tumor co-culture configuration. Third, by modifying parts of the channel structure, temporally varying concentration gradients were generated using gravity-driven flow.

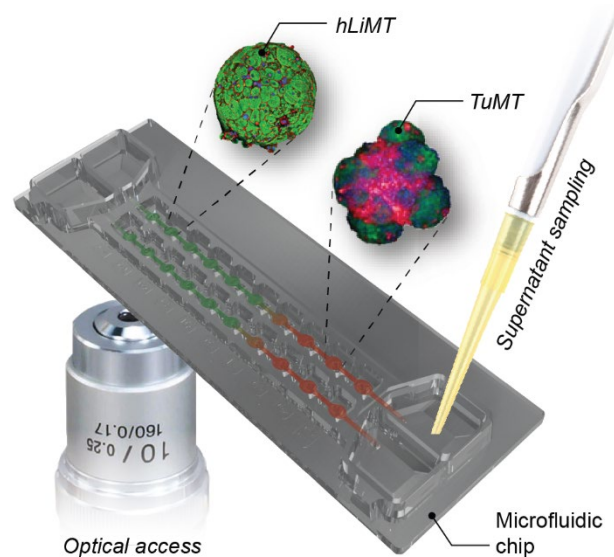
This thesis contains three journal articles:

1. **Scalable microfluidic platform for flexible configuration of and experiments with microtissue multiorgan models.** Christian Lohasz, Nassim Rousset, Kasper Renggli, Andreas Hierlemann and Olivier Frey. *SLAS Technology* 24(1), 79–95 (2018).
2. **Predicting metabolism related drug-drug interactions using a multi-tissue microphysiological system.** Christian Lohasz,* Flavio Bonanini,* Kasper Renggli, Olivier Frey, and Andreas Hierlemann. In preparation for submission.
3. **Tubing-free microfluidic culture system featuring gradual, in vivo-like substance exposure profiles.** Christian Lohasz, Olivier Frey, Flavio Bonanini, Kasper Renggli and Andreas Hierlemann. *Frontiers in Bioengineering and Biotechnology*, 7, 72 (2019).

1.5 Summary of major results

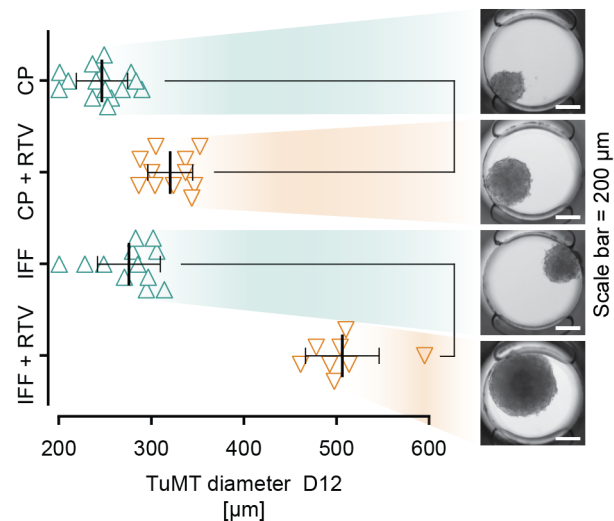
Realization of a robust, scalable system for the culture of 3D microtissues

A polystyrene-based microfluidic chip was developed. With polystyrene as chip material, the chip possessed superior ad- and absorption properties (less ad- and no absorption) as compared to similar PDMS-based chip systems. Fabrication by injection molding and operation by gravity-driven flow yielded a chip system for large-scale, parallelized experimentation with up to ten interconnected 3D microtissues per channel.



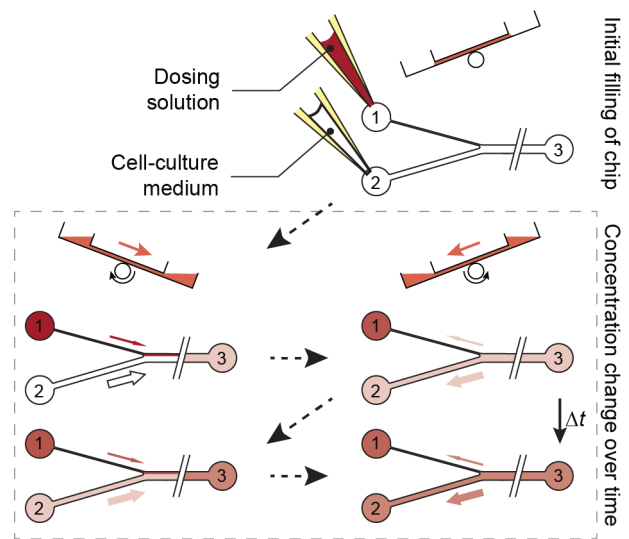
Detection of drug-drug interactions *in vitro*

The gravity-driven chip system was used in a liver-tumor co-culture setup to detect metabolism-related drug-drug interactions. The impact of certain drugs on hepatic metabolism and their interference with anticancer therapy was successfully detected using both, liver and tumor microtissues in the same platform. The developed system holds great promise for testing drug combinations and detecting undesired drug-drug interactions under physiological conditions.



Pump-less generation of temporally varying concentration gradients

The channel structure of the gravity-driven microfluidic chip was modified to enable temporally varying concentration changes. A Y-junction and two channels of different diameter were introduced on one side. This configuration enabled to slowly release a drug solution to the 3D microtissue culture site over time. The resulting system enabled the exposure of 3D microtissues to concentration profiles that resembled the ones in a human body upon administration of a drug.



1.6 References

1. DiMasi, J.A., H.G. Grabowski, and R.W. Hansen, Innovation in the pharmaceutical industry: New estimates of R&D costs. *J Health Econ*, **47**, 20-33 (2016).
2. Paul, S.M., et al., How to improve R&D productivity: the pharmaceutical industry's grand challenge. *Nature reviews. Drug discovery*, **9**, 203-214 (2010).
3. Zhang, B. and M. Radisic, Organ-on-a-chip devices advance to market. *Lab Chip*, **17**, 2395-2420 (2017).
4. Esch, E.W., A. Bahinski, and D. Huh, Organs-on-chips at the frontiers of drug discovery. *Nature reviews. Drug discovery*, **14**, 248-260 (2015).
5. Mak, I.W., N. Evaniew, and M. Ghert, Lost in translation: animal models and clinical trials in cancer treatment. *American journal of translational research*, **6**, 114-118 (2014).
6. Sato, T. and H. Clevers, Growing self-organizing mini-guts from a single intestinal stem cell: mechanism and applications. *Science*, **340**, 1190-1194 (2013).
7. Kolesky, D.B., et al., 3D bioprinting of vascularized, heterogeneous cell-laden tissue constructs. *Adv Mater*, **26**, 3124-3130 (2014).
8. Skylar-Scott, M.A., et al., Biomanufacturing of organ-specific tissues with high cellular density and embedded vascular channels. *Sci Adv*, **5**, eaaw2459 (2019).
9. Trietsch, S.J., et al., Microfluidic titer plate for stratified 3D cell culture. *Lab on a Chip*, **13**, 3548-3554 (2013).
10. Huh, D., et al., Reconstituting organ-level lung functions on a chip. *Science*, **328**, 1662-1668 (2010).
11. Kelm, J.M., et al., Method for generation of homogeneous multicellular tumor spheroids applicable to a wide variety of cell types. *Biotechnol Bioeng*, **83**, 173-180 (2003).
12. Lin, R.Z. and H.Y. Chang, Recent advances in three-dimensional multicellular spheroid culture for biomedical research. *Biotechnol J*, **3**, 1172-1184 (2008).
13. Hong, E.J. and E.B. Jeung, Assessment of Developmental Toxicants using Human Embryonic Stem Cells. *Toxicological research*, **29**, 221-227 (2013).
14. Ramachandran, K., et al., Assessment of re-aggregated human pancreatic islets for secondary drug screening. *British journal of pharmacology*, **171**, 3010-3022 (2014).
15. Polonchuk, L., et al., Cardiac spheroids as promising in vitro models to study the human heart microenvironment. *Sci Rep*, **7**, 7005 (2017).

16. Klingelhutz, A.J., et al., Scaffold-free generation of uniform adipose spheroids for metabolism research and drug discovery. *Sci Rep*, **8**, 523 (2018).
17. Messner, S., et al., Multi-cell type human liver microtissues for hepatotoxicity testing. *Arch Toxicol*, **87**, 209-213 (2013).
18. Vorrink, S.U., et al., Endogenous and xenobiotic metabolic stability of primary human hepatocytes in long-term 3D spheroid cultures revealed by a combination of targeted and untargeted metabolomics. *FASEB J*, **31**, 2696-2708 (2017).
19. Bell, C.C., et al., Characterization of primary human hepatocyte spheroids as a model system for drug-induced liver injury, liver function and disease. *Scientific Reports*, **6**, 25187 (2016).
20. Kozyra, M., et al., Human hepatic 3D spheroids as a model for steatosis and insulin resistance. *Scientific Reports*, **8**, 14297 (2018).
21. Hirschhaeuser, F., et al., Multicellular tumor spheroids: an underestimated tool is catching up again. *J Biotechnol*, **148**, 3-15 (2010).
22. Drewitz, M., et al., Towards automated production and drug sensitivity testing using scaffold-free spherical tumor microtissues. *Biotechnology Journal*, **6**, 1488-1496 (2011).
23. Huber, J.M., et al., Evaluation of assays for drug efficacy in a three-dimensional model of the lung. *Journal of Cancer Research and Clinical Oncology*, **142**, 1955-1966 (2016).
24. Bolck, H.A., et al., Tracing Clonal Dynamics Reveals that Two- and Three-dimensional Patient-derived Cell Models Capture Tumor Heterogeneity of Clear Cell Renal Cell Carcinoma. *European urology focus*, (2019).
25. Marx, U., et al., Biology-inspired microphysiological system approaches to solve the prediction dilemma of substance testing. *ALTEX*, **33**, 272-321 (2016).
26. Domansky, K., et al., Perfused multiwell plate for 3D liver tissue engineering. *Lab on a Chip*, **10**, 51-58 (2010).
27. Rogal, J., et al., WAT's up!? – Organ-on-a-chip integrating human mature white adipose tissues for mechanistic research and pharmaceutical applications. *bioRxiv*, 585141 (2019).
28. Beaurivage, C., et al., Development of a Gut-On-A-Chip Model for High Throughput Disease Modeling and Drug Discovery. *Int J Mol Sci*, **20**, (2019).
29. Maschmeyer, I., et al., A four-organ-chip for interconnected long-term co-culture of human intestine, liver, skin and kidney equivalents. *Lab Chip*, **15**, 2688-2699 (2015).

30. Miller, P.G. and M.L. Shuler, Design and demonstration of a pumpless 14 compartment microphysiological system. *Biotechnol Bioeng*, **113**, 2213-2227 (2016).
31. Edington, C.D., et al., Interconnected Microphysiological Systems for Quantitative Biology and Pharmacology Studies. *Sci Rep*, **8**, 4530 (2018).
32. Esch, M.B., et al., How multi-organ microdevices can help foster drug development. *Advanced drug delivery reviews*, **69-70**, 158-169 (2014).
33. Bauer, S., et al., Functional coupling of human pancreatic islets and liver spheroids on-a-chip: Towards a novel human ex vivo type 2 diabetes model. Vol. 7.(2017)
34. Boos, J.A., et al., Microfluidic Multitissue Platform for Advanced Embryotoxicity Testing In Vitro. *Advanced Science*, **6**, 1900294 (2019).
35. Wang, Y.I., et al., Multiorgan Microphysiological Systems for Drug Development: Strategies, Advances, and Challenges. *Adv Healthc Mater*, **7**, (2018).
36. Berthier, E., E.W. Young, and D. Beebe, Engineers are from PDMS-land, Biologists are from Polystyrenia. *Lab Chip*, **12**, 1224-1237 (2012).
37. Byun, C.K., et al., Pumps for microfluidic cell culture. *Electrophoresis*, **35**, 245-257 (2014).
38. Frey, O., et al., Reconfigurable microfluidic hanging drop network for multi-tissue interaction and analysis. *Nature communications*, **5**, 4250 (2014).
39. Benam, K.H., et al., Small airway-on-a-chip enables analysis of human lung inflammation and drug responses in vitro. *Nat Methods*, **13**, 151-157 (2016).
40. Schneider, O., et al., User-Friendly and Parallelized Generation of Human Induced Pluripotent Stem Cell-Derived Microtissues in a Centrifugal Heart-on-a-Chip. *Tissue engineering. Part A*, **25**, 786-798 (2019).
41. Zimmermann, M., et al., Capillary pumps for autonomous capillary systems. *Lab on a Chip*, **7**, 119-125 (2007).
42. Walker, G. and D.J. Beebe, A passive pumping method for microfluidic devices. *Lab Chip*, **2**, 131-134 (2002).
43. Sung, J.H., C. Kam, and M.L. Shuler, A microfluidic device for a pharmacokinetic-pharmacodynamic (PK-PD) model on a chip. *Lab Chip*, **10**, 446-455 (2010).
44. Kim, J.Y., et al., 3D spherical microtissues and microfluidic technology for multi-tissue experiments and analysis. *J Biotechnol*, **205**, 24-35 (2015).
45. Esch, M.B., et al., Modular, pumpless body-on-a-chip platform for the co-culture of GI tract epithelium and 3D primary liver tissue. *Lab Chip*, **16**, 2719-2729 (2016).

46. Wang, Y.I. and M.L. Shuler, UniChip enables long-term recirculating unidirectional perfusion with gravity-driven flow for microphysiological systems. *Lab Chip*, **18**, 2563-2574 (2018).

2 SCALABLE MICROFLUIDIC PLATFORM FOR FLEXIBLE CONFIGURATION OF AND EXPERIMENTS WITH MICROTISSUE MULTIORGAN MODELS

Christian Lohasz, Nassim Rousset, Kasper Renggli, Andreas Hierlemann and Olivier Frey. Scalable Microfluidic Platform for Flexible Configuration of and Experiments with Microtissue Multiorgan Models. *SLAS Technology* 24(1), 79–95 (2018).

DOI: 10.1177/2472630318802582

2.1 Abstract

Microphysiological systems hold the promise to increase the predictive and translational power of *in vitro* substance testing owing to their faithful recapitulation of human physiology. However, the implementation of academic developments in industrial settings remains challenging. We present an injection-molded microfluidic microtissue (MT) culture chip that features two channels with ten MT compartments each and that was designed in compliance with microtiter-plate standard formats. Polystyrene as chip material enables reliable, large-scale production and precise control over experimental conditions due to low ad- or absorption of small, hydrophobic molecules at/into the plastic material in comparison to predecessor chips made of polydimethylsiloxane. The chip is operated by tilting, which actuates gravity-driven flow between reservoirs at both ends of every channel, so that the system does not require external tubing or pumps. The flow rate can be modulated by adjusting the tilting angle on demand. The top-open design of the MT compartment enables efficient MT loading using standard or advanced pipetting equipment, it ensures oxygen availability in the chip and allows for high-resolution imaging. Every channel can be loaded with up to ten identical or different MTs, as demonstrated by culturing liver and tumor MTs in the same medium channel on the chip.

2.2 Introduction

Microphysiological systems (MPS), mimicking human physiology and disease states, are a promising solution to improve the predictive power of *in vitro* testing in pharmaceutical, chemical and cosmetic industries and bridge the gap to clinical tests and real-life scenarios. A variety of microfluidics-based MPS have recently been developed. Roughly, they can be split into three categories: (i) single-organ or “organ-on-a-chip” systems, (ii) multi-organ systems, and (iii) “body-on-a-chip” systems.¹ “Organ-on-a-chip” systems include a realistic representation of an organ’s multicellular microarchitecture and functionality.^{2, 3} Multi-organ systems with two or more organs reproduce specific tissue-tissue interactions and interplay, which enables more systemic insights into compound action.^{4, 5} Finally, “Body-on-a-chip” systems are aimed at recapitulating important characteristics of human physiology as closely as possible, featuring up to ten organs and a higher degree of complexity.⁶ The advantages of using MPSs for advanced *in-vitro* testing include (i) more predictive and reproducible toxicity and efficacy testing, (ii) early exclusion of drug candidates in the drug development pipeline, (iii)

the possibility to perform substance testing on relevant human disease models and (iv) a reduction of animal studies. Therefore, implementing MPS in industrial settings has the promise to achieve lower development costs, to shorten development time and to achieve more meaningful and representative test results.

While in the past two decades a lot of efforts to explore the potential of MPS have been made on the academic level, the technology development now moves towards industry-compatible solutions. MPS commercialization has begun,^{1, 7-9} but a broad industrial implementation faces challenges of (i) system and experimental robustness and reproducibility, (ii) compatibility with existing analytical methods, (iii) scalability and seamless integration into industrial workflows, and (iv) capability to mimic tissue characteristics and disease states faithfully. We want to work out these four challenges in more detail. (i) A reliable fabrication of robust MPSs is necessary to generate reproducible experimental data.¹⁰ Complex and time-consuming – often manual – fabrication processes usually have negative impacts on the systems' robustness. Furthermore, material properties and fabrication methods may influence the reliability of the chip fabrication and/or the reproducibility of experimental results.^{11, 12} (ii) Compatibility with currently used and common read-out systems improves the adoption of new MPS-based systems. New systems will be more readily accepted and implemented if common read-out methods, such as biochemical assays and microscopy, can be used to benchmark results. (iii) Scalability and seamless integration into industrial standard processes imposes requirements on liquid-handling and cell-culture techniques. To enable MPS integration into high-throughput pipelines of industrial compound testing, compatibility with standard pipetting equipment and lab automation tools is critical. (iv) The capability to accurately and reproducibly mimic the behavior of a certain tissue in healthy or diseased state is a key requirement for any method of substance testing.¹⁰ The cellular components and culturing environment of the system have to recapitulate the *in vivo* situation as much as possible. Specific organ functions, as well as the physiologically relevant interactions between organs have to be represented in order to enable meaningful interpretation of experimental outcomes.¹³ In addition, the predictive power of an *in vitro* system is entirely dependent on translating its outcomes to *in vivo* scenarios or establishing correlation to clinical data.^{14, 15, 10}

We have presented a predecessor microfluidic device for culturing of three-dimensional (3D) microtissues (MTs).^{16, 17} Microtissues are scaffold-free, cellular constructs that have the several advantages: (i) superior organ-specific functionality as compared to conventional 2D culturing

methods, (ii) standardized formation methods with high reproducibility in medium to high throughput formats, and (iii) a wide range of different tissue types can be generated.^{18, 19} In comparison to other 3D cell culture approaches, microtissues are more straight-forward to generate, more uniform, and less expensive.²⁰⁻²² The previous device could be operated without the need for a pump and relied on gravity-driven perfusion. The flow speed could be modulated by adjusting the tilting angle. Different types of MTs were produced off-chip and then loaded into four MT compartments along the channels. The bidirectional flow allowed for fluidic “communication” between the MTs, which was shown by combining rat liver and colorectal cancer MTs in the same channel. The pro-drug cyclophosphamide was bio-activated by the liver MTs and showed significant effects on growth and viability of the cancer MTs.¹⁷ Scaling was achieved by arranging up to 11 separate channels, each with six MT compartments, on stackable chips in a microtiter plate format. Reservoirs and MT compartments were arranged at a pitch of 9 mm and were, therefore, conveniently addressable with standard multichannel pipettes for 96-well microtiter plates.¹⁶

In this article, we present pivotal advancements of the existing tilting chip design in an effort to make it industry-compatible and push it towards commercialization. Using polystyrene (PS) instead of polydimethylsiloxane (PDMS) as material, the chip can be mass-produced by injection molding at high reproducibility. Furthermore, issues with absorption of small, hydrophobic molecules in PDMS²³⁻²⁵ were eliminated by replacing PS for PDMS as chip material, which will broaden the spectrum of the chip’s possible applications. A redesign of the MT compartment in view of current standards of lab automation equipment was done so as to ensure full compatibility with common industrial routines. Conical access ports, herein called *Standing Drop Ports*, ensure the accessibility of the MT compartments directly from the top, which can then be addressed individually by automated liquid handling systems. We demonstrate fully automated MT loading. The number of MT compartments was increased to ten MTs per channel, which provides a larger number of replicates per condition and the possibility to apply a larger number of different endpoint measurements. Furthermore, a thin optically transparent PS layer closing the channels at the bottom enables the use of high-resolution imaging tools and methods. Culturing both, human liver and colorectal cancer MTs in the same channel and chip demonstrates its use as a single- and multi-organ MPS, a central advantage of the microfluidic microtissue culture chip.

Versatility and ease of operation of the system represent, besides parallelization and automation potential, key features of the developed microfluidic microtissue culture system, which is suited for both, academic research and highly standardized and regulated industrial applications (from mid- to high-throughput).

2.3 Materials and Methods

2.3.1 Microfluidic chip design

The microfluidic chip design builds on previously published microfluidic platforms that permit combined culturing of different microtissue types.^{16, 17} Its footprint matches that of standard microscope slides ($25 \times 75 \text{ mm}^2$) and the microtissue (MT) compartment pitch matches that of microtiter plates. The design comprises of two separate microfluidic channels, featuring ten MT compartments each, and medium reservoirs at both ends of each channel (Figure 1A, B).

The central feature of the chip is the MT compartment. It is designed as a cylinder with a funnel-like structure that opens to the top and is surrounded by a hydrophobic rim (Figure 1C). Capillary pinning at the rim stabilizes standing drops that cap the MT compartment upon filling the chip with liquid. A wall was structured around each MT compartment opening and acts as a cross-contamination barrier between the two channels (Figure 1B). The top-open design of the compartment has several advantages: (i) the funnel acts as a vent and prevents bubble formation during the initial filling process; (ii) it enables direct access to the compartment for efficient loading of microtissues into the chip, MT manipulation during experiments or removal of MTs for downstream analysis; (iii) no compartment closure is needed that may be tedious to realize, will render the device prone to bubble inclusion, and will interfere with the MT and the fluidic system (pump effect due to closure pressing); (iv) dead volume can be kept minimal; (v) gas exchange is ensured in proximity to the culturing site; and (vi) optical transparency of the material enables high-quality for optical readouts. Protective barrier structures, patterned perpendicularly to the perfusion channel protect microtissues against flow shear stress, while they allow for a constant exchange of medium around the spheroid (Figure 1D). Microfluidic channels end in medium reservoirs that hold up to 200 μL of cell culture medium (Figure 1A). All reservoirs are easily accessible for supernatant sampling and medium exchange throughout experiments. Four chips can be assembled in a handling frame (Microfluidic ChipShop, Jena,

Germany), resulting in a platform with SBS (Society for Biomolecular Sciences) standard formats (footprint dimensions of 128.8 mm × 85.5 mm and well spacing of 4.5 mm; Figure 1E, F).^{26, 27} Thus, one assembled platform enables culturing of ten microtissues – of identical or different type – under eight identical or different conditions.

All MT compartments have a diameter of 800 μm , a height of 1.3 mm and a volume of 1.04 μL , as shown in Figure 1. The interconnecting perfusion channels are 600 μm wide, 100 μm high and 52.4 mm long. A single channel and the respective ten MT compartments have a combined volume of 16.5 μL , which remains in the chip during medium exchange. The dead volume in the funnel structure above the ten MT, which is not directly replaced by perfusion, has a volume of 1.02 μL (10.2 μL in total per channel). MT compartments are spaced in a SBS

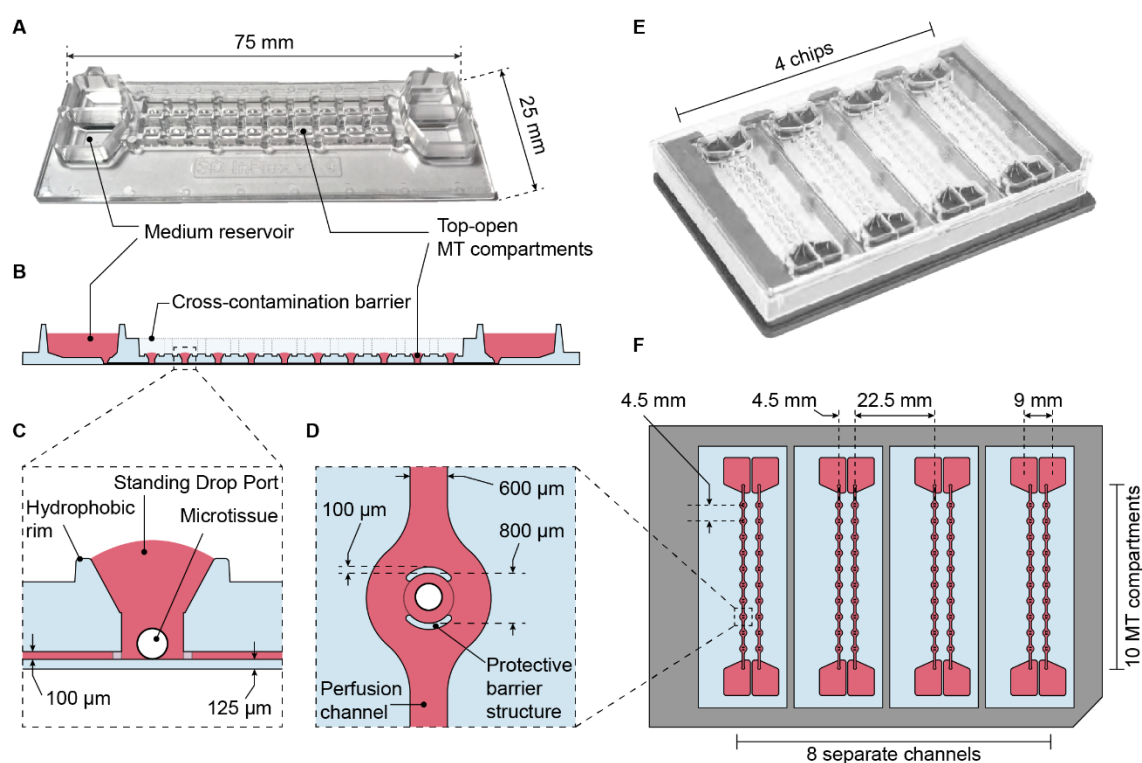


Figure 1: Layout of the microfluidic chip. **(A)** Single chips have the size of microscopy slides and feature two individual perfusion channels with ten top-open MT compartments and medium reservoirs at both ends. Chips were fabricated by injection molding of polystyrene. **(B)** Cross-section of the chip along one channel. The cross-contamination barrier prevents interaction between the two separated channels. **(C)** Side view of the MT compartment. Spheroids are cultured at the bottom of the MT compartment. The “Standing Drop Port” is generated by a hydrophobic rim around the top of the MT compartment, which prevents liquid from flowing out of the channels. **(D)** Top view of the MT compartment indicating the barrier structures that protect spheroids from flow-induced shear stress. **(E)** Four chips can be assembled in one handling frame, which **(F)** is compliant with SBS standard formats. Reservoirs and MT compartments coincide with positions on 96-well or 384-well microtiter plates.

fashion to coincide with the positions of the wells of a 384-well microtiter plate (4.5 mm pitch). Medium reservoir positions match the wells of a 96-well plate (9 mm pitch). The top-open design of the MT compartments and the use of standard formats enable the use of common multichannel pipettes and enable automated chip and frame operation.

The chips were produced by injection molding of polystyrene, and the channels were sealed with a 125 μm thick polystyrene membrane (Figure 1C). Microfluidic chips with a long-term stable hydrophilic and cell-repellent surface coating in the channels, compartments and reservoirs are commercially available from InSphero AG (Schlieren, Switzerland).

2.3.2 Chip loading and operation

Chips are single-use and provided in a sterile state. To fill channels with cell culture medium, the assembled plate with four chips is tilted along its long axis, and medium (37°C) is filled into the upper reservoir. The height difference between the two reservoirs drives the flow through the channel to the lower reservoir (Figure 2B).

The plate is then placed in a horizontal position for MT loading. Previously formed MTs are aspirated from microtiter plates and are loaded into the MT compartments by contact-transfer via the *Standing Drop Ports* (see below). MT loading can be performed (i) individually with a single-channel pipette, (ii) in parallel with multichannel pipettes for up to 96 channels, or (iii) automatically with a robotic liquid handling system. The medium is fully exchanged after loading to compensate for medium evaporation during the MT loading procedure. The loaded plate is covered with a lid (Microfluidic ChipShop) fitting the handling frame (Figure 2A).

To minimize medium evaporation during the experiment, three measures were applied: (i) all MT compartments were sealed with an adhesive, custom-cut polyester film with holes for oxygen exchange, sticking to the aforementioned cross-contamination barrier; (ii) the reservoirs were sealed with a custom-cut, pressure-sensitive film with holes that provide access to the reservoirs for sampling of supernatant and medium exchange; and (iii) the plate was stacked onto a PBS-filled 96-well microtiter plate to increase water saturation of the air in direct proximity to the chips (Figure 2A).

Channel perfusion is gravity-driven. Tilting of the assembled plate around its long axis results in a height difference between the two reservoirs connected to each channel. The hydrostatic

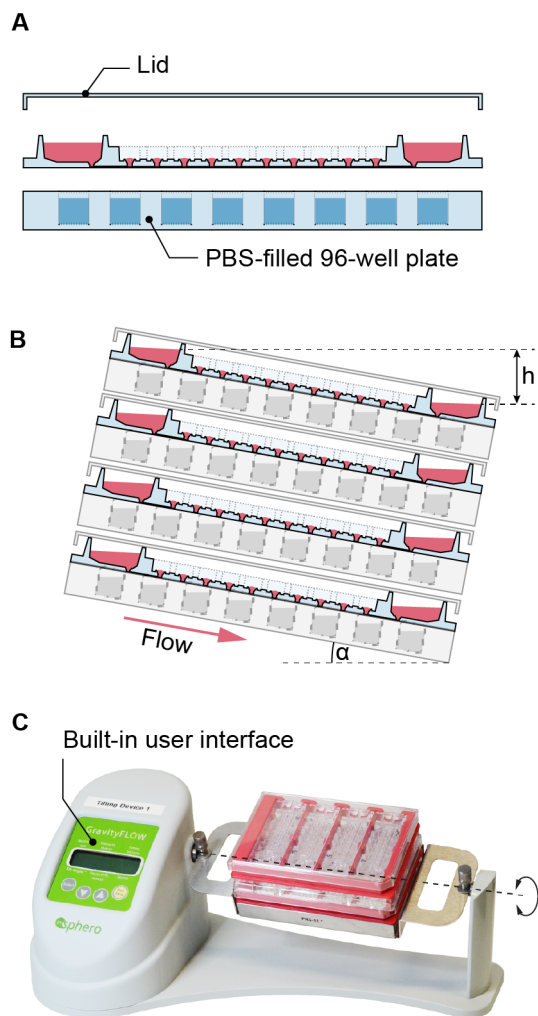


Figure 2: Operation of the microfluidic device. **(A)** For experiments, handling frames with four chips were covered with a lid and were stacked on PBS-filled 96-well microtiter plates to increase humidity around the chip and limit reservoir evaporation. **(B)** Perfusion is generated by tilting the assembled platform along its long axis. A tilting angle α generates a height difference h between the two reservoirs at the ends of the channels. Up to four plates can be stacked for parallel experiments. **(C)** The small tilting stage with a built-in user interface fits into bench-top cell culture incubators.

with up to 320 MTs. Further parallelization can be achieved by increasing the number of tilting stages in the same incubator. All handling and operation steps can be performed under sterile conditions.

pressure difference between the reservoirs then pushes medium from the upper to the lower reservoir through the channels. Upon tilting the plate back and forth, medium is shuffled continuously between the two reservoirs. Capillary forces at the reservoir-channel junction retain liquid in the channels in the event that the upper reservoir would fall dry. This effect prevents complete drainage of the channel, which would lead to (i) introduction of bubbles into the channel or (ii) drying out of the MTs. The assembled and loaded plate was operated on a programmable tilting stage (InSphero AG). The stage allows for adjustment of the positive and negative tilting angle, resting times at tilted or horizontal positions, and transition times between positive and negative angles. The entire setup (Figure 2C) fits into a standard benchtop cell culture incubator, where experiments can be performed in a controlled environment over several days. The microfluidic plate can be handled like a conventional microtiter plate for sampling of supernatant, medium exchange and imaging. A short interruption of the tilting and removal of the plates from the incubator is required for any of these activities. For parallelization of experiments, up to four plates can be stacked onto each other on the same tilting stage, which yields 32 different experimental conditions

2.3.3 Flow rate measurements

Measuring the flow rate in the chip at various tilting angles was achieved by setting an assembled platform on a tilting stage at a defined angle α . Channels and MT compartments were filled with medium to ensure steady flow from the beginning of the experiment. Ensuring that the lower reservoir was empty, 150 μL of cell culture medium were added in the upper reservoir at time 0. The resulting hydrostatic pressure drove the flow from the upper reservoir into the lower reservoir. After a given time interval (1 to 25 minutes), all accumulated liquid volume in the lower reservoir was collected and measured on a precision scale (XS204, Mettler-Toledo GmbH, Greifensee, Switzerland; sensitivity: 0.1 mg). A liquid volume of 16.5 μL remained in the channels and MT compartments during medium exchange. It was identical before adding the 150 μL of cell culture medium and after the measurement.

The previously determined volume V_{i-1} at time t_{i-1} , was then subtracted from the volume V_i collected at a sampling time t_i , which yielded a value for the flow rate $Q_i = (V_i - V_{i-1}) / (t_i - t_{i-1})$. Flow-rate measurements under cell-culture conditions at 37 °C in a humidified incubator were not feasible for two reasons: (i) a repeated opening and closing of the incubator for sampling would not have allowed for maintaining a stable atmosphere (humidity, temperature) within the incubator; (ii) since the evaporation rate would have been higher in an incubator, evaporation control measurements – as described in *Chip loading and Operation* – could not have been applied at the required sampling frequency. To minimize systematic errors, all measurements were, therefore, performed at room temperature (20°C). Evaporation was taken into account as a source of error and quantified by weighing a medium-filled chip over time. For each experimental tilting angle, 12 measurements were performed in 4 separate channels and repeated over two days.

2.3.4 Computational modeling

The purpose of operating the chip at defined tilting angles is to ensure continuous perfusion throughout the experiment. Numerical models of gravity-driven flow and capillary effects provide insights on the operational limits of the chip to avoid drying out reservoirs or inducing leakage at the *Standing Drop Ports*. Since flow rates at 37 °C could not be measured, a model, based on previous analytical techniques^{28, 29} was developed to calculate flow rates, which was validated with 20 °C flow rate measurements at various time points (Fig 5A – C). The model

included the combination of a matrix implementation of the hydraulic-electric analogy with Kirchhoff's law and a time-stepping with the forward Euler method to establish a transient flow rate through all components of the chip. More detailed information can be found in the Supplementary Methods to this article.

2.3.5 Absorption experiments

Two different chip materials – polydimethylsiloxane (PDMS) and polystyrene (PS) – were compared with regard to their absorption characteristics of different molecules. PDMS chips were fabricated according to previously published techniques.¹⁶ PDMS chips and PS chips were filled with 150 μL of cell culture medium containing biologically – for *in vitro* experiments – relevant concentrations of one substance per condition: diazepam (1 μM), acetaminophen (5 mM), testosterone (4.5 μM ; all obtained from Sigma-Aldrich, Buchs, Switzerland) and albumin (5 $\mu\text{g ml}^{-1}$; Bethyl Laboratories Inc, Montgomery, TX, USA). The filled microfluidic chips were placed in an incubator and were operated by tilting for the duration of the experiment. Medium (5 μL) was sampled out of the reservoirs at several time points between 0 h and 48 h to track molecule concentrations in the channels. No fresh medium was added at these time points. Diazepam, testosterone and acetaminophen were externally quantified by UPLC-MS (Admescope Oy, Oulu, Finland). Albumin concentrations were measured using an enzyme-linked immunosorbent assay (ELISA) as described later.

Nile Red (Sigma-Aldrich) and CyTM3-coupled antibody (CyTM3 AffiniPure Donkey Anti-Chicken IgY, Jackson ImmunoResearch Europe Ltd., Cambridgeshire, UK) concentrations were monitored by fluorescence microscopy (λ_{Ex} 565 nm/ λ_{Em} 610/75 nm) over 24 h.

2.3.6 Oxygen measurements

The 2D oxygen distribution in the channel and MT compartments was measured over time to assess oxygenation via the *Standing Drop Ports*. An oxygen sensor foil (PreSens Precision Sensing GmbH, Regensburg, Germany) was used to close the channels of the chip at the bottom. Cell culture medium was loaded into the chip, and the chip was placed into a chamber with constant nitrogen perfusion to deplete the medium of oxygen. After 20 min, one of the channels was sealed with a polyester foil, and nitrogen perfusion was turned off. To limit oxygen distribution only to diffusion from medium reservoirs or the *Standing Drop Ports*, the chips

were maintained without tilting. The oxygen-dependent fluorescence signal of the sensor foil was tracked by taking images every 15 s during 20 min using the VisiSens TD detector (PreSens). The relative oxygen concentration within the channels was calculated in reference to oxygen-depleted medium containing sodium sulfite (Na_2SO_3 ; Sigma-Aldrich) and medium, equilibrated with ambient air. The data was evaluated using VisiSens Scientific Software (PreSens).

2.3.7 Cell culture

All spheroids used for experiments were produced off-chip and were then transferred into the MT compartments of the chip. Human liver microtissues (hLiMTs) were obtained from InSphero AG, Schlieren, Switzerland, and delivered ready to use in AkuraTM 96-microtissue plates. They were maintained in human liver maintenance medium AF (hLiMM-AF; InSphero AG), and medium was exchanged every two to three days until MT transfer and usage on the chip system.

TuMTs were formed using the HCT116 human colon carcinoma cell line or the GFP-tagged MDA-MB-361 breast adenocarcinoma cell line, both provided by InSphero AG. 300 cells in 70 μL cell culture medium were seeded into each well of AkuraTM 96-microtissue plates (InSphero AG) and spun down at $250 \times g$ for 2 min. To accumulate cells in one corner of the well and enhance spheroid formation, the plate was placed in a cell-culture incubator in a slightly tilted position. After three days of formation, spheroids with a diameter of 250 μm could be transferred into the microfluidic chip. RPMI-1640 medium (Gibco, Fisher Scientific, Illkirch Cedex, France), supplemented with 10% fetal bovine serum (FBS, Sigma-Aldrich, Buchs, Switzerland) and 1% penicillin and streptomycin, was used for TuMT formation and maintenance.

For on-chip microtissue culture, assembled and loaded plates were tilted by 20° with tilting intervals of 7 min and transition times of 50 s. Co-culture experiments combining both spheroid types were performed using hLiMM-AF as common medium.

2.3.8 Biochemical assays

Urea, a biomarker for liver functionality, was quantified in the cell-culture supernatant using the QuantiChrom™ Urea Assay Kit (BioAssay Systems, Hayward, CA, USA) according to the manufacturer's protocol. The viability of all spheroids was assessed at the end of experiments measuring intracellular adenosine triphosphate (ATP) with the CellTiter-Glo® 3D Cell Viability Assay (Promega AG, Dübendorf, Switzerland). To this end, spheroids were harvested from chip and transferred back into Akura™ 96 microtissue plates before performing the assay according to the manufacturer's guidelines. Human albumin was quantified using ELISA (Bethyl Laboratories Inc, Montgomery, TX, USA) according to the manufacturer's protocol.

2.3.9 Imaging

Bright-field and fluorescence images were acquired using an inverted microscope (DMI-6000B; Leica Microsystems AG, Heerbrugg, Switzerland) with a 5× objective, a CCD camera (DFC-340-FX; Leica) and a stage top incubator enabling long-term live imaging. To focus on the elevated microfluidic chips in the handling frame, a distance ring (Thorlabs GmbH, Dachau, Germany) was used to increase the parfocal length of the objective. All images were analyzed using ImageJ software.

High-resolution images were recorded on an Olympus FV-MPERS system, equipped with a Newport SpectraPhysics DS+ 2-photon-laser. A XLPLN25XSVMP (25x, NA 1.0) water-immersed lens was used for imaging. The excitation wavelength was set to 900 nm. The spatial resolution was $0.63 \times 0.63 \times 2 \mu\text{m}^3$. 119 images were acquired along the z-direction to cover the entire spheroid.

2.4 Results and Discussion

2.4.1 Material properties

A major improvement from previous prototypes is the complete replacement of PDMS. Since the chip does not feature any on-chip valves and pumps, no elastic material – i.e., PDMS – was needed, and polystyrene (PS) could be used. PS is a validated material for cell-culture applications and features a range of favorable advantages over PDMS.

Part of this study focuses on comparing absorption of biologically relevant substances in PDMS and PS by tracking their concentration over time. To highlight substance-material interaction, hydrophobic and hydrophilic molecules were chosen from three classes: (i) drug compounds, delivered to the cellular model – e.g., diazepam (hydrophobic) and acetaminophen (hydrophilic), which are commonly used compounds to gain insights into transcellular permeability and liver toxicity. (ii) Hormones and proteins, secreted by cells to communicate with other cell types, serving as viability, functionality or responsiveness readouts – e.g., testosterone (hydrophobic) and albumin (hydrophilic), which are molecules, secreted by Leydig cells and liver. (iii) On-chip staining compounds serving as labels for fluorescence imaging – e.g., Nile Red (hydrophobic) and Cy3-coupled antibodies (hydrophilic). The fluorescent compounds were chosen to demonstrate material-dependent staining efficiency and imaging quality on chip. All measured compound concentration values were normalized to the initial concentration before loading.

The selected drug compounds show different material-dependent concentration changes. The hydrophobic diazepam (Figure 3A) remained at a constant concentration within the PS chip, whereas its concentration drastically decreased in the PDMS chip. Already after 4 h, only 5% of the initial concentration was present in the PDMS channel. Concentrations of the hydrophilic acetaminophen (Figure 3B), on the other hand, did not decrease in channels of both materials. Whereas the acetaminophen concentration remained constant in the PS chip, its concentration even increased in the PDMS chip. The hydrophobic testosterone showed similar characteristics as diazepam: its concentration in PDMS channels rapidly decreased over the course of the experiment and, after 4 h, only about 10% of the initial concentration in the solution was detectable. The concentrations of the large, hydrophilic molecule albumin did not change much in both materials. Again, a slight increase was observed in PDMS channels. The observation of increased concentrations in PDMS can be explained by evaporation of water through the porous polymer material,³⁰ which is not the case for using PS. Fluctuations of compound concentrations in the PS chip can be explained by the manual sampling of a liquid volume of 5 μ L and the subsequent two dilution steps to then conduct the analysis, as small inaccuracies in sampling volume potentiate upon dilution. Furthermore, unequal evaporation in the two technical replicates may have introduced experimental errors.

The distribution of Nile Red and Cy3-coupled antibodies was monitored by fluorescence microscopy. The microfluidic channel was imaged at three time points: directly after loading, after 1 h, and 24 h. Bright-field images indicate the outline of the respective channels and fluorescence images (Suppl. Figure 1) show the distribution of substances across the chips. The fluorescence signal intensity was analyzed along a cross section orthogonally to the channel. Nile Red is a small hydrophobic dye that is used to stain lipids. It showed fast leakage into the PDMS material directly after loading of the chip (Figure 3E). During incubation time, the corresponding fluorescence signal within the channel region steadily decreased and reached approx. 40% after 24 h, while Nile Red penetrated deeper into the material and spread away from the channel. The intensity profile along the channel cross section illustrates this shift of fluorescence intensity over time. In the channels of the PS chips (Figure 3E), on the other hand, the fluorescence signal remained localized inside the channel structure with clear drops in the intensity profile that coincided with channel walls. No decrease of fluorescence intensity within the channel regions was observed. The fluorescence signal of Cy3-labeled antibodies inside the channel structures did not change for both, PDMS and PS chips (Figure 3F). The clear edges at

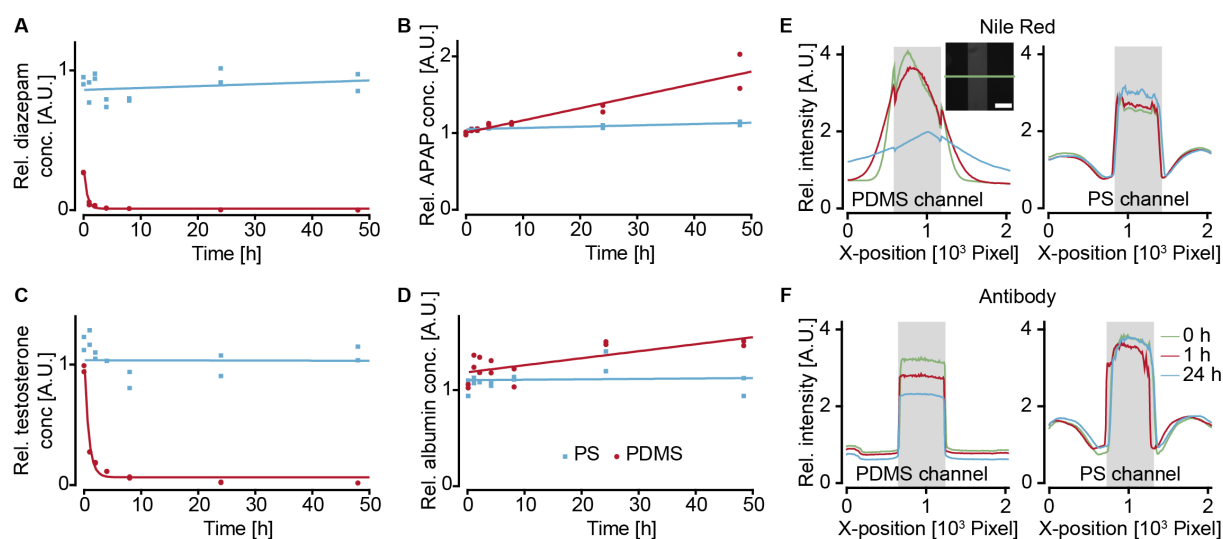


Figure 3: Absorption of substances in polydimethylsiloxane (PDMS) and polystyrene (PS). (A) Diazepam, (B) acetaminophen and (C) testosterone and (D) human albumin were loaded into chips with similar channel structures and were incubated for 48 h. Concentrations of samples taken over time were quantified by (A)-(C) UPLC-MS, or (D) ELISA. (E) Nile Red and (F) Cy3-conjugated antibodies were loaded into PDMS and PS chips and were incubated for 24 h. Bright-field and fluorescence ($\lambda_{\text{Ex}} = 565 \text{ nm}/\lambda_{\text{Em}} = 610/75 \text{ nm}$) images were taken. Fluorescence intensity profiles illustrate the distribution of the substances within the channels and the wall materials over time. The fluorescence image in (E) illustrates the image analysis method. Sampling at $t = 0 \text{ h}$ was performed as fast as possible after filling the channels, but there was already diffusion into the wall material visible. For more fluorescence images and graphs, see Suppl. Fig. 1.

the channel borders indicated that there was no diffusion of the molecule into the chip material. A difference that was observed between the two chip materials included a decreasing signal over time in the in the PDMS chip. The signal reduction in the PDMS chip might be a result of unspecific adsorption in MT compartments and reservoirs.

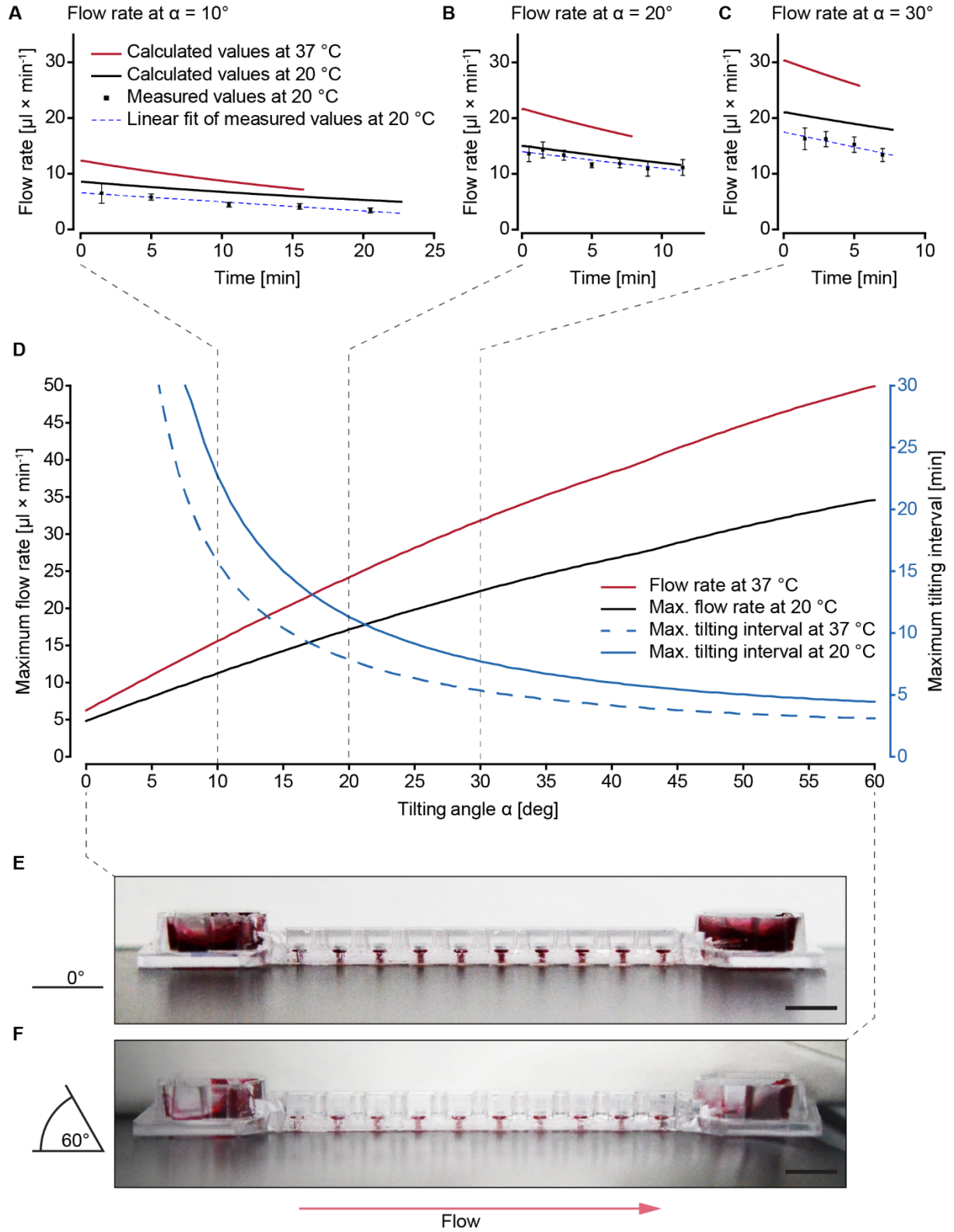
Comparing the chips made from two different materials, we found that several substances were ab- or adsorbed in PDMS, whereas their concentrations did not change in PS. The absorption of substances into PDMS depended mainly on their molecular size and hydrophobicity and could be estimated to a certain degree. Precise concentration control cannot be guaranteed in a PDMS-based microfluidic system, in particular with advanced experimental protocols including repeated compound dosing and extended exposure times. Our results, therefore, evidence a clear advantage of PS over the commonly used PDMS as a microfluidic chip material.

2.4.2 Operation by tilting

Control of the flow rate is crucial to reliably operate microfluidic microtissue culture chips. Here, flow was driven by reservoir height differences and channel parameters – i.e., through gravity and hydraulic resistance. Flow rates at tilting angles of 10°, 20° and 30° were modeled numerically until complete drainage of the upper reservoir into the lower one. Measurements were performed for the same tilting angles over defined time intervals. Thus, the graphs of both, calculated and measured flow rates end at the time point when the respective upper reservoirs fell dry (Figure 4A – C).

Sub1 – Numerical model

Medium flow through the channels and into the standing drops was determined for various temperatures T and tilting angles α . Temperature affects both, density ρ and dynamic viscosity η of the cell culture medium, whereas the tilting angle affects the height difference Δh between the reservoirs as a function of inter-reservoir distance L : $\Delta h = L \sin \alpha$. The gravity-induced hydrostatic pressure ΔP through the chip depends on the tilting angle and the fluid height at each reservoir $h_{in/out}$: $\Delta P = \rho g [L \sin \alpha + h_{in} - h_{out}]$. In principle, the flow rate Q through the device is proportional to ΔP for a given channel hydraulic resistance R_{hyd} . An analytical



solution exists for the simple case of two reservoirs interconnected by a simple channel: $Q = \Delta P / R_{\text{hyd}}$. However, the contribution of each standing drop along the channel leads to a decrease of the expected flow rate value in a non-trivial way.

Figure 4: Tilting angle-dependent perfusion of the chip using an initial liquid volume of 150 μL . **(A)-(C)** Flow rate as a function of time at tilting angles α of **(A)** 10°, **(B)** 20° and **(C)** 30°. Measured values at 20 °C ($n = 12$ measurements) match the calculated flow rates over time and allow for extrapolation to an experimentally relevant temperature of 37 °C. Slopes of the decreasing flow rates over time at 20 °C amounted to -0.16 ± 0.018 , -0.30 ± 0.037 and $-0.54 \pm 0.104 \mu\text{L min}^{-2}$ for the measured values and to -0.16 ± 0.001 , -0.30 ± 0.001 and $-0.41 \pm 0.001 \mu\text{L min}^{-2}$ for the calculated values at tilting angles of 10°, 20° and 30°, respectively. For additional bar graphs of the flow rates, see Suppl. Fig. 2. **(D)** The maximum flow rate and tilting interval until drainage of the top reservoir at 20 °C and 37 °C as a function of the tilting angle. Respective curves for initial liquid volumes of 100 μL and 200 μL can be found in Suppl Fig. 3 Representative side views of the chip at **(E)** 0° and **(F)** 60° show the stability of the standing drops at large tilting angles (scale bars = 5 mm).

The hydraulic-electric analogy was used to determine the flow rate over time at various tilting angles with the following components: (i) a hydraulic resistance R_{hyd} for channels that interconnect the MT compartments; (ii) a negligible hydraulic resistance r_{hyd} for the MT compartment loading ports due to their large size relative to the interconnecting channels; (iii) a Laplace pressure ΔP_{cap} (due to surface tension γ) at the standing drop ports – the standing drops' curvatures R change as they fill or empty: $\Delta P_{\text{cap}} = 2\gamma/R$. The upper reservoir h_{in} empties and the lower reservoir h_{out} fills up, which decreases the hydrostatic pressure driving flow over time. Updating the values of reservoir filling heights and Laplace pressures with time-stepping returns: (i) the inlet flow rate over time, including the maximum flow rate; and (ii) the maximum tilting interval – i.e., the time that a given tilting angle can be held until the inlet reservoir is emptied, which results in zero flow.

Sub2 – Experimental measurements

The measured values were compared to predicted values obtained by computational modeling (Figure 4A – C). The flow rates decreased over time, due to drainage of the upper reservoir and filling of the lower reservoir, resulting in a decreasing gravity-induced hydrostatic pressure. The slope of the measured flow rates correlated with the calculated ones (Suppl. Fig. 2), the values being generally slightly lower. The slopes of the decreasing flow rates over time at 20 °C amounted to -0.16 ± 0.018 , -0.30 ± 0.037 and $-0.54 \pm 0.105 \mu\text{L min}^{-2}$ for the measured values and to -0.16 ± 0.001 , -0.30 ± 0.001 and $-0.41 \pm 0.001 \mu\text{L min}^{-2}$ for the modeled values at tilting angles of 10°, 20° and 30°, respectively. The discrepancy between computational models and experimental results can be explained by several effects: (i) the density and viscosity of the cell-

culture medium differs slightly from that of water, especially when using FBS-supplemented medium³¹; (ii) the polystyrene chip shrunk by a couple of micrometers during the fabrication process, decreasing channel dimensions, which entailed increased channel hydraulic resistance and lower flow rates; (iii) capillary wetting effects in the reservoirs reduce the effective hydrostatic pressure, leading to decreased flow rates, especially at larger tilting angles; (iv) modeling of the distribution of incoming liquid in the lower reservoir becomes challenging with increasing tilting angles. Nevertheless, the correlation between the measured values and the computational models at 10° and 20° shows that flow rate and tilting time at different angles can be approximated. The same computational model was then used to extrapolate flow rates for microtissue culture conditions (37 °C) in Figure 4A – D. Compared to room temperature, culture conditions decrease the viscosity and density of liquids. This decrease has a multiplicative effect on the flow rate, which leads to proportionally higher flow rates, i.e., less time before drainage of the upper reservoir at culture conditions.

Figure 4D summarizes the effect of the tilting angle at 20 °C and 37 °C on the maximum flow rate and maximum tilting interval with an initial medium volume of 150 µL (respectively maximum flow rate value and maximum time in Figure 4A – C). Exceeding the maximum tilting interval results in an interruption of the flow through the chip. Since continuous perfusion should be maintained throughout the experiment, interval time must be carefully considered when programming the tilting scheme. Furthermore, the viscosity of cell culture medium changes with its contents. FBS-supplemented medium or flowing cells can therefore also influence the flow rate in the chip.³¹ The range of applicable flow rates in the chip is only limited by the stability of the standing drops and the risk that the standing drop will burst – i.e., liquid flows out of the standing drops – due to excessive hydrostatic pressure at large tilting angles. Monitoring the drops from the side while steadily increasing the tilting angle shows that angles of up to 60° do not result in standing drop bursting (Figure 4E, F). Variations in the initially loaded liquid volume also effects resulting flow rates and applicable tilting intervals, as shown in Suppl. Figure 3. The bidirectional flow upon repeated tilting is shown in Suppl. Figure 4.

The ability to conveniently define the operation conditions – e.g. the flow rate – by controlling the tilting angle of the device, and the large range of applicable tilting angles, render the developed chip system flexible and straightforward to use. In addition, the obtained flow rates are in good agreement with computational-model guided values to ensure molecule concentration uniformity within MPS.³²

2.4.3 The Standing Drop Port and MT compartment

The key features of the chip are the *Standing Drop Ports* and MT compartments. The top-open MT compartments, spaced in compliance to SBS-standard formats, enable the usage of a wide range of standard pipetting equipment – from manual/automatic single/multi-channel pipettes to fully automated liquid handling robots – to load MTs into the chip. Figure 5A shows a schematic of the MT transfer from their production plates into the chip system using five channels of an 8-channel multichannel pipette or a robotic pipetting system. Several spheroids are taken up from microtiter plates in parallel – one per pipette tip – by aspirating 3-10 μL of cell culture medium. Upon sedimentation of the MT to the opening of the pipette tip, these are transferred into the *Standing Drop Port* by contact transfer. Touching the drop with the pipette tip lets the spheroid settle through the standing drop liquid interface and – guided by the funnel structure – down into the designated MT compartment. No pumping action is required, which minimizes liquid carry-over. This transfer method also entails a minimum of potentially damaging fluid shear stress, as each MT is subjected to only one pipetting step and as neighboring MT compartments are not disturbed upon pipetting into a target compartment.

Sub 1 – Chip MT loading

Figure 5 illustrates that the number of simultaneously transferred MTs depends on the operation mode, i.e., the use of mono- or co-culture scenarios on the chip. For a monoculture configuration, we used a 9-mm pitch multichannel pipette, which enables a transfer of five MTs per pipetting step – requiring two pipetting steps per microfluidic channel (Figure 5A). Since different MT types are received on separate microtiter plates, the use of a co-culture configuration entails a transfer of one to five MTs per pipetting step, – which requires up to ten pipetting steps in total for a completely heterogeneous configuration. Figure 5B illustrates the pipetting scheme for a co-culture configuration of four TuMTs and six hLiMTs. The use of externally fabricated MTs offers several advantages, e.g., the robustness of the procedure and the possibility to introduce quality control steps, but also requires an efficient loading method. Table 1 compares characteristic parameters for chip loading procedures for single- and multi-tissue configurations. We distinguished between the overall loading time, i.e., the time for the entire loading procedure, and the bench time, i.e., the time needed for active user manipulations. The transfer efficacy was used as a measure of how many MTs were successfully transferred to their target locations. Empty MT compartments were afterwards manually populated.

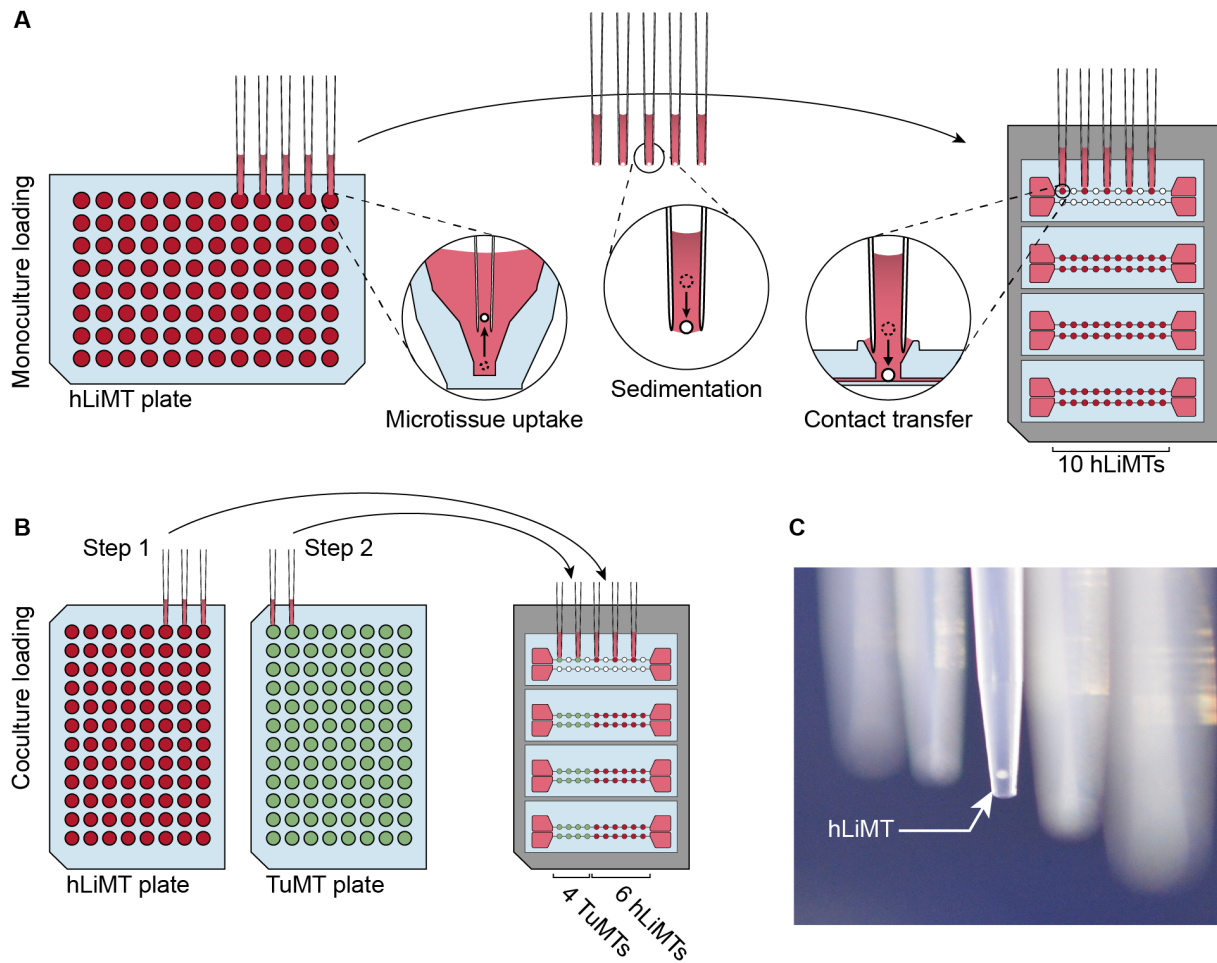


Figure 5: Schematic of the MT loading procedure with an 8-channel pipette or an automated pipetting system. Spheroids are picked up in parallel from production plates and sediment to the opening of the pipette tips. Approaching the Standing Drop Port with the pipette tip, the two liquids combine, and the MT is transferred into the compartment. **(A)** For monoculture configurations, up to five MTs can be transferred simultaneously in two pipetting steps per channel. **(B)** Co-culture configurations with two MT types, e.g., hLiMTs and TuMTs, which come from separate production plates require four pipetting steps with 2 – 3 MTs in parallel. **(C)** Representative image of a hLiMT sedimenting inside a pipette tip.

Transfer with a manual single-channel pipette required the largest amount of bench time, with 20 pipetting steps per chip, but offered a high degree of control over the process, leading to a high transfer efficacy. By using an electronic 8-channel pipette with 9-mm pitch, the loading throughput could be increased, with four to eight pipetting steps per chip, but the loading efficacy was lowered, since pipetting five MTs simultaneously needed precise tip placement, which was tedious when manually performed. 96-channel semi-automated pipetting systems (VIAFLO 96/384, Integra Biosciences, Zizers, Switzerland) offered guided tip positioning and

Table 1: Characteristic parameters for chip loading using different pipetting equipment.

Loading procedure	Loading time per plate [min]	Actual bench time [min] ^a	Pipetting steps per plate	Loading efficiency [%] ^b
Manual single-channel pipette				
Single-organ configuration	38:00 (± 5 min)	38:00 (± 5 min)	20	100
Two-organ configuration	38:00 (± 5 min)	38:00 (± 5 min)	20	100
Multi-channel pipette^c				
Single-organ configuration	9:00 (± 60 s)	9:00 (± 60 s)	16	80
Two-organ configuration	13:00 (± 90 s)	13:00 (± 90 s)	32	90
Electronic 96-channel pipette^d				
Single-organ configuration	8:00 (± 40 s)	8:00 (± 40 s)	8 ^e	95-100
Two-organ configuration	18:00 (± 2 min)	18:00 (± 2 min)	16	95-100
Liquid-handling robot				
Single-organ configuration	20:40	0:15	16	100
Two-organ configuration	42:20	0:15	32	100

^aActual time during which the process needs full attention of the scientist to perform the process after preparing the bench with all necessary plates and reagents.

^bPercentage of MTs present in the designated MT compartment after one loading attempt. Missing MTs were afterwards transferred individually.

^cWe used an electronic single-row, 96-well, 8-channel pipette from Vaudaux-Eppendorf AG, Schönenbuch, Switzerland. Higher efficiencies may be obtained with multi-channel pipettes with adjustable tip spacing (e.g. Voyager pipette, Integra Biosciences, Zizers, Switzerland).

^dThe mechanical guiding limits the movement of the pipette head and does not allow to address all wells on the production plate resulting in larger numbers of left-over spheroids per plate. Maximal 20 tips were inserted into the 96-well head for parallel transfer of up to 20 MTs.

^eEach transfer was performed twice to increase loading efficiency. A single transfer (4 pipetting steps in total) would result in ~80-85% loading efficiency and at a loading time of only 5 min per plate.

loading of all 4 chips in parallel (Suppl. Movie 1). Loading time could, therefore, be further reduced, while loading efficiency was still high. Transfer with a fully automated liquid handling robot (Hamilton STAR, Hamilton Bonaduz AG, Bonaduz, Switzerland), equipped with eight

pipetting channels, enabled to use the same pipetting patterns as with the 8-channel pipette, i.e., the transfer of two to five MTs simultaneously and a filling of the chip in four to eight pipetting steps (Suppl. Movie 2). In contrast to the other loading methods, the loading time here markedly differed from the actual bench time. User manipulation was reduced to setting up the liquid handling robot with corresponding microtiter plates and empty chips. After robot initiation, all MTs were transferred to their designated MT compartment autonomously. Transfer efficiency between two 96-well plates reached 100%, without any damage to the MTs, by adapting the liquid handling robots' pipetting speed and volume for MT pickup (Suppl. Figure 5).

Sub 2 – Chip MT harvesting

The same procedures as used for loading can be applied to harvest MTs for off-chip analyses at the end of an experiment. Each MT can be individually targeted and analyzed, which expands the readout options for a single experiment. To remove MTs, pipette tips were positioned at the *Standing Drop Ports*, and the MTs were taken up with 3-5 μ L of medium (Figure 6A). They were then transferred into microtiter plates, where they could be individually processed. For example, the viability of individual MTs could be determined by MT lysis and quantification of intracellular adenosine-triphosphate (ATP) concentrations. At the same time, remaining MTs of the same experiment and channel could be fixed and stained individually. Routinely applied methods for static MT cultures can be applied. Especially for multi-tissue configurations, it is, however, crucial to separate the respective organ-MTs and perform tissue-specific readouts.

Sub 3 – MT monitoring

The top-open design and the 125 μ m-thin PS membrane at the bottom of the MT compartments render the chip compatible with high resolution imaging. Figure 6B and Suppl. Movie 3 show a slice through and the full stack of a MT consisting of GFP-tagged MDA-MB-361 breast adenocarcinoma cells. The on-chip live image was taken with an inverted multiphoton microscope and demonstrates the suitability of the chip for use with high-resolution imaging techniques. The 125 μ m distance in between the objective and the MT enable the use of high NA immersion objectives.

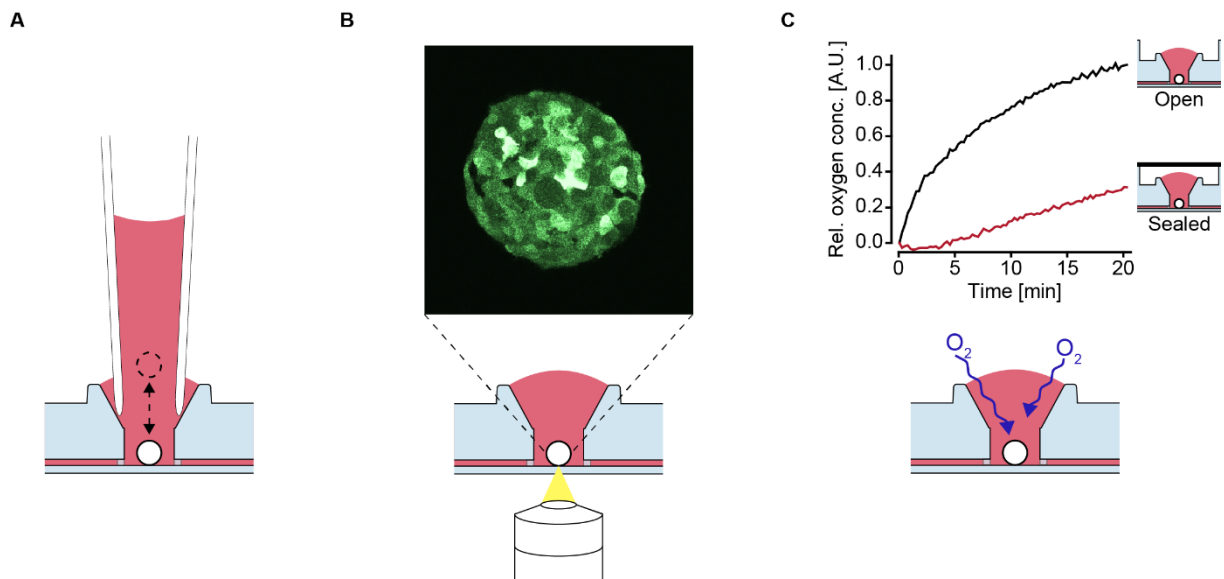


Figure 6: Advantages of the Standing Drop Port. **(A)** Direct accessibility from the top facilitates MT loading and harvesting. **(B)** The thin membrane at the bottom of the MT compartment enables high-resolution imaging. The image shows a MT consisting of GFP-tagged MDA-MB-361 breast adenocarcinoma cells and was acquired using a multiphoton microscope. **(C)** The top-open design of the Standing Drop Port increases the medium surface area and ensures sufficient oxygenation for cell culture applications.

Sub 4 – MT oxygen supply

A further advantage of the top-open design of the MT compartment is the increased surface area of the medium and its exposure to air. Polystyrene is, in contrast to PDMS, not permeable to gas. This property can lead to oxygen limitations at the cell or MT culture sites in closed microfluidic systems.

To assess oxygenation of the medium at the microtissue culturing sites, the medium in the chip was depleted of oxygen and its recovery was monitored over 20 min. The oxygenation was compared to a separate, hermetically sealed channel, simulating a closed microfluidic environment. The oxygen concentration in the open channel quickly increased upon exposure to ambient air (Figure 6C), approaching equilibrium within approximately 20 min. In contrast, the oxygenation in the closed channel was substantially delayed. An increase of dissolved oxygen was only observed after 5 min, and the concentration reached approximately 30% after 20 min. The delayed increase of oxygen within the closed channel can be explained by the fact that diffusion of oxygen only can occur through the open medium reservoirs at the ends of the

channel, so that the oxygen supply in the closed chip is very limited, especially in the central MT compartments of the channel.

In combination with the open reservoirs at the ends of the channels, the open *Standing Drop Ports* improve the culture conditions for cell types that are sensitive to low oxygen levels (Figure 6C).

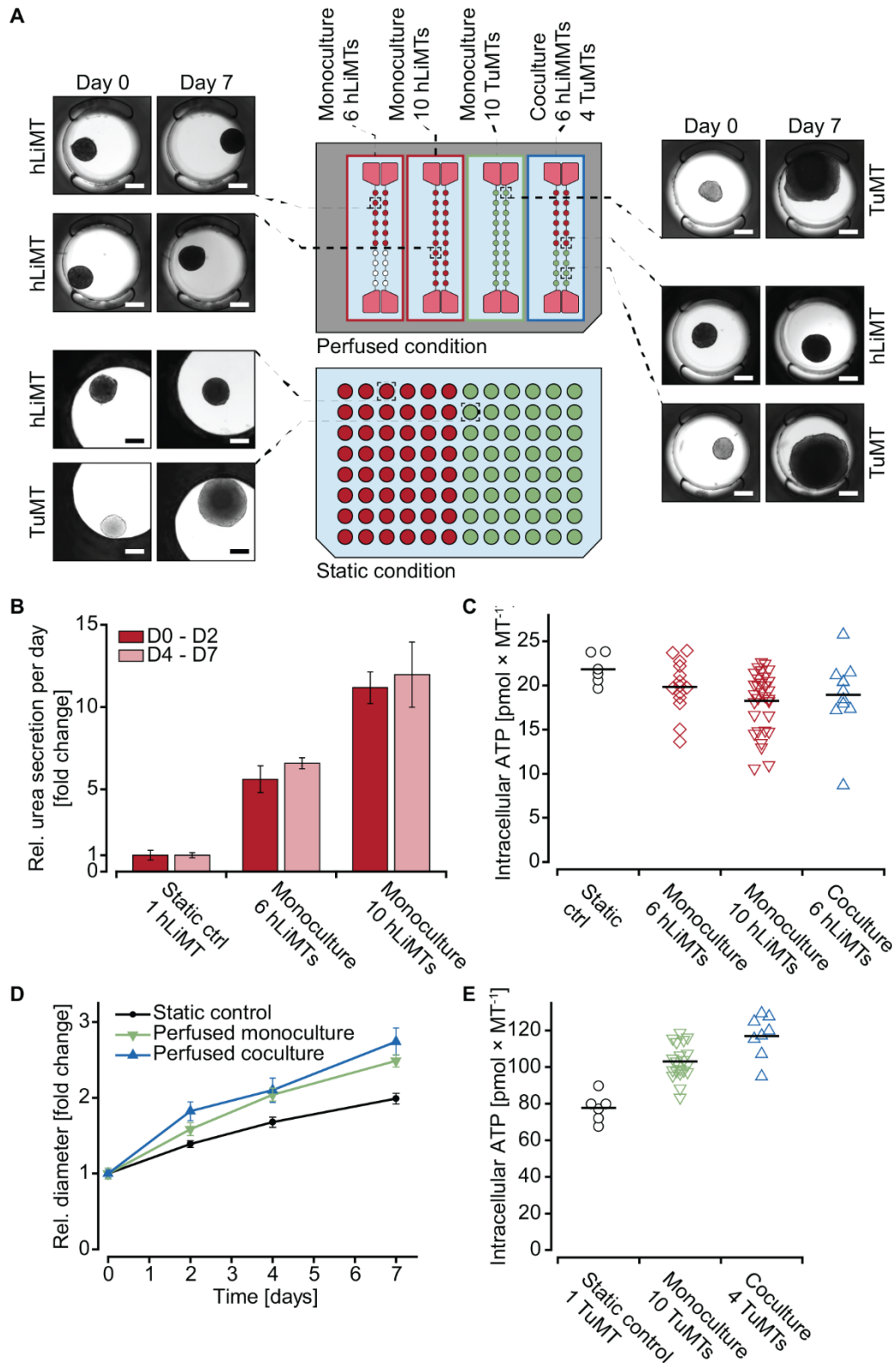
2.4.4 On-chip microtissue culture

Two different spheroid types, hLiMTs and TuMTs, were co-cultured over seven days. Several identical (monoculture) or different (co-culture) spheroids were interconnected under conditions of constant perfusion on a chip and their characteristics were compared to those of spheroids cultured under static conditions in a 96-well microtiter plate – one MT per well, i.e. no interconnections. For monoculture experiments on chip, six hLiMTs, ten hLiMTs, or ten TuMTs were cultured in the same channel. Co-culture configurations included six hLiMTs and four TuMTs in one channel (Figure 7A). Spheroid imaging, sampling of the supernatant, and medium exchange were performed on days 0, 2, 4 and 7 for all culture conditions. On day seven, the spheroids were harvested, and intracellular adenosine-triphosphate (ATP) concentrations were measured to assess their viability. Images of spheroids were taken to observe potential morphological changes, which may indicate harmful effects of the perfusion conditions. Liver MTs (Figure 7A) showed similar morphology for all different culturing conditions and for all time points. Sizes and shapes of the spheroids were similar under static and perfusion culturing conditions and did not change over the duration of the experiment. To assess the functionality of hLiMTs, urea was quantified in the freshly sampled supernatant on days two and seven. Urea is a waste product of the human body, used for ammonia detoxification, and is primarily synthesized by the liver. Quantification of the molecule in cell-culture supernatants is used as an indicator for the metabolic activity of cells. The amount of urea, produced by one spheroid under static conditions, was compared to that produced by six or ten spheroids in the same channel under perfusion (Figure 7B). Measured values showed an enrichment of urea in the supernatant, proportional to the number of hLiMTs in the system: in channels with six and ten hLiMTs, the amount of measured urea was approximately six- and ten-fold higher than in a single-MT well under static conditions with secretion rates of 82.0-97.8 ng MT⁻¹ day⁻¹ on day 2 and 44.0-52.6 ng MT⁻¹ day⁻¹ on day 7. Lower urea secretion rates on day 7 can be explained by decreasing secretion rates of the cellular model over time, which has been described

previously for different primary hepatocyte models.^{33, 34} Consistent tissue-number-dependent amounts of urea on both days, however, evidenced that there weren't any negative effects of the culturing of hLiMTs in the microfluidic chips. Measurements of intracellular ATP concentrations on the last day of the experiment (Figure 7C) revealed that hLiMTs, cultured under static conditions or in perfused monoculture or co-culture configurations, all remained similarly viable. The size of hLiMTs remained stable over time under all conditions, which was expected based on their non-proliferative nature (Suppl. Figure 6). Further, the reproducibility of these experimental results could be shown by culturing up to 80 hLiMTs over 7 – 14 days independently in two different labs with different persons operating the chip system. Chips with 10 hLiMTs per channel were maintained for 14 days. The MT size was tracked over the experimental period, and intracellular ATP was measured on day 7 and 14. The results were in good agreement with other independently conducted experiments and demonstrated the robustness and reproducibility of the microfluidic microtissue culture chip (Suppl. Figure 7).

Also, the tumor model was cultured as single spheroids in static 96-well microtiter plates and under perfusion in monoculture and co-culture configurations with hLiMTs. On day 0, all TuMTs were similar in size (approx. 210 to 250 μm) and morphology (Figure 7A) for the three different culture conditions. On day 7, TuMTs had grown considerably (approx. 480 to 610 μm), nearly overgrowing the MT compartments in some cases. TuMT growth was tracked by measuring their diameter on days 0, 2, 4 and 7 (Figure 7D). Uniform growth was seen for all spheroids cultured under perfusion (approx. 50 $\mu\text{m day}^{-1}$ in diameter), while static conditions led to a considerably lower growth rate (approx. 35 $\mu\text{m day}^{-1}$). These observations can be explained by the fact that perfusion entails a constant delivery of nutrients to the MT compartments, whereas static culturing conditions are diffusion-limited within the culture well volume. Standard deviations of TuMTs growth were remarkably low, indicating a high uniformity among TuMTs for the same condition, within the same or different channels. These observations were represented as ATP contents of TuMTs on day seven (Figure 7E), which were lower in the smaller spheroids cultured under static conditions in well plates as compared to perfusion conditions. However, TuMTs showed similar ATP/cell mass ratios for all conditions with $148.7 \pm 16.1 \text{ pmol mm}^{-3}$ for monoculture perfusion, $144.8 \pm 29.1 \text{ pmol mm}^{-3}$ for co-culture perfusion, and $147.5 \pm 16.6 \text{ pmol mm}^{-3}$ for static conditions.

Up to ten hLiMTs were cultured in a volume of 150 μL without observing any negative impacts on their morphology, functionality or viability. Furthermore, urea secretion by hLiMTs



indicated that also other metabolites or cytokines could be enriched in the device between two medium exchanges as a result of the higher cell-to-medium ratio. Such up-concentration can be advantageous for readouts that are not feasible in standard microtiter plates. Single spheroids

Figure 7: Culturing of hLiMTs (red) and TuMTs (green) in monoculture and co-culture (blue) configuration on chip and under static conditions in well microtiter plates. **(A)** Six to ten spheroids per channel were loaded into the chips and were cultured for 7 days (tilting angle = 20°, tilting intervals = 7 min). Representative bright-field images show spheroids for all conditions and the static controls in the well microtiter plates at days 0 and 7 (scale bars = 200 μ m). **(B)** Urea secretion of hLiMTs under static and perfused mono-culture conditions, presented as fold change of static control (ctrl) hLiMT (n = 4 samples). **(C)** ATP-dependent viability of hLiMTs in mono- and co-cultures on day 7 (n = 6 – 40 hLiMTs; — = mean values). **(D)** Growth of TuMTs under static and perfused monoculture and co-culture conditions (n = 6 – 20 TuMTs; data represented as mean \pm SD). **(E)** ATP-dependent viability of TuMTs in mono- and co-cultures on day 7 (n = 6 – 20 TuMTs; — = mean values).

in the comparably large medium volumes of 96-well microtiter plates may not produce enough of certain biomarkers to exceed the respective lower limit of detection. Additionally, this up-concentration effect may also have advantages when combining different spheroids, since the concentrations of cytokines and metabolites produced by one tissue type are more likely to reach thresholds to act on the other target tissues.

By combining hLiMTs and TuMTs in the same channel, we showed that co-culture experiments are generally possible for at least seven days. Noteworthy, combinations are not limited to these two spheroid types, but can be adapted as needed by the experimenter. Fine-tuning of medium formulations fitting the needs of all organ models, however, needs to be considered. Combinations of different spheroid types – or of spheroids with circulating cells, such as immune cells or circulating tumor cells – enable a range of studies, in which tissue communications and interaction play a major role. Combinations of liver models with other organs of choice, for example, are interesting for drug toxicity and efficacy screenings. Since the liver is the first organ to experience drugs that enter the human body, it is the main organ of first-pass metabolism, but also the primary victim of drug-induced toxicity. The liver, therefore, has a large influence on the concentration of drugs and their metabolites in the system and makes drug testing in combination with other target organs such as heart, brain, pancreas or tumors more representative and predictive. Other promising and feasible applications of the developed system could include (i) disease models involving inflammation, e.g., inflammatory bowel disease, by combining an intestinal model with circulating cells of the immune system, or (ii) cancer progression by implementing circulating tumor cells and possible target MTs. The use of patient-derived cell material will be relevant in the field of personalized medicine.

2.5 Conclusion

Here, we presented a microfluidic chip system and its characterization, which holds great potential for the large-scale integration into industrial applications. We demonstrated the advantages of using polystyrene for chip production with respect to the absorption of metabolite or compound molecules over current academic devices made of PDMS.

Operation of the chip relies on gravity-driven flow and does not require specialized equipment, such as external tubing or expensive precision pumps. Nevertheless, flow rates could reliably be established and modulated, and a wide range of flow rates could be applied on demand.

Key feature of the chip was the newly designed MT compartment with its *Standing Drop Port*. The top-open design was one of the pivotal features for application of the chip in high-throughput settings, since it allows for direct access to the microtissue culturing site with automated pipetting equipment. The versatility of using the microfluidic chip system with standard lab equipment to handle and load the chip with cellular models renders the chip system suitable for usage in different settings. Depending on the equipment available in the lab and the throughput needed, standard, low cost solutions are as suitable to work with the device as are expensive, fully automated systems.

The performance of the microfluidic device in combination with the two cellular models, liver and cancer, demonstrates the flexibility of the system and the wide range of possible applications. A variety of different organ models in the form of microtissues can be generated off-chip with a high degree of reproducibility. External spheroid formation before loading and experimentation with the spheroids in the chip systems allows for introducing additional quality control steps to ensure optimal performance. Microtissue numbers, combinations and flow regimens can be modified on demand. The chip and its general operation remain the same, which allows to standardize handling and operation to a large extent. Variations of the spheroid numbers in the system did not have any impact on the functionality of individual spheroids, as was evidenced by the urea measurements. The presented features and the high flexibility in available tissue models render the presented chip system an ideal candidate for drug discovery and diagnostic applications.

2.6 Acknowledgements

The work was financially supported by the Swiss CTI grant 18024.1 PFLS-LS. The authors thank Martin Rausch, Novartis AG, for the high resolution images taken for the study. We acknowledge David Fluri and Fabrizio Hürlimann for setting up MT transfer schemes with different pipetting equipment.

2.7 Supporting Information

Computational Modeling

The numerical model combines a matrix implementation of hydraulic-electric analogy with Kirchhoff's law to find flow rates and pressures in each channel and at each point in the device. Subsequently, a time-stepping scheme is implemented with the forward Euler method to establish the flow transients through all components of the chip.

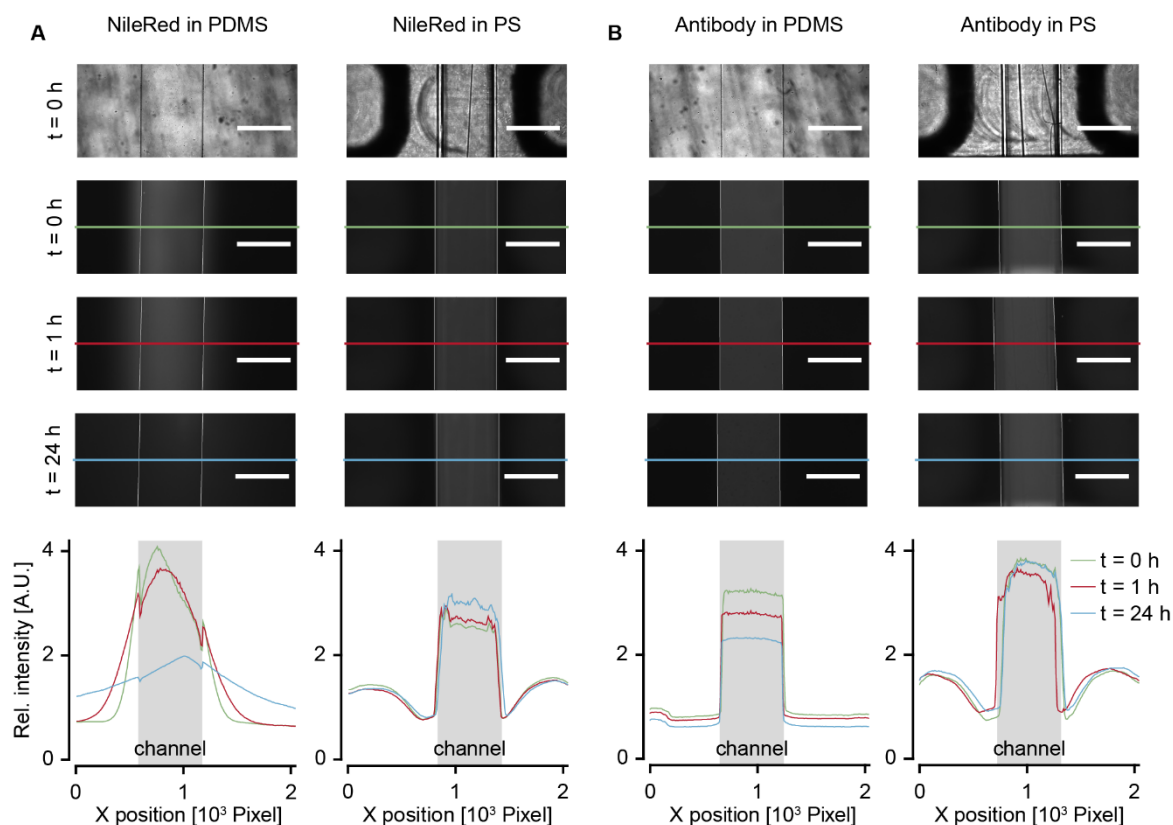
The hydraulic-electric analogy models (i) each channel as a hydraulic resistance, (ii) each drop with a given curvature as a pressure source due to their Laplace pressure, and (iii) all components with a height greater than that of the channel – from the inlet-outlet to each individual MT compartment – as pressure sources due to gravity. (i) Hydraulic resistances are found by importing the device structure in COMSOL Multiphysics® and using the Laminar Flow module. (ii) The volume in the drop dictates its radius, R , which, with surface tension γ , generates a Laplace pressure $\Delta P_{\text{Lap}} = \gamma/2R$. (iii) Due to gravity g and the liquid density, ρ , the height h above the channel generates a pressure $\Delta P_g = \rho gh$.

The equivalent circuit is composed of pressure sources at open drops and reservoirs, nodes at each MT compartment, and hydraulic resistances between all nodes and pressure sources. Each pressure source has a known pressure given by the volume contained in it: Standing drops have a pressure given by their capillary radius, dependent on the volume, and by the height of the MT compartment; the inlet and outlet exert a certain pressure on the system depending on the tilting angle and on how much volume they contain. Writing the equations in a matrix form (Kirchhoff's law) enables to find the unknown inter-nodal flow rates and nodal pressures for a given volume contained in drops and reservoirs.

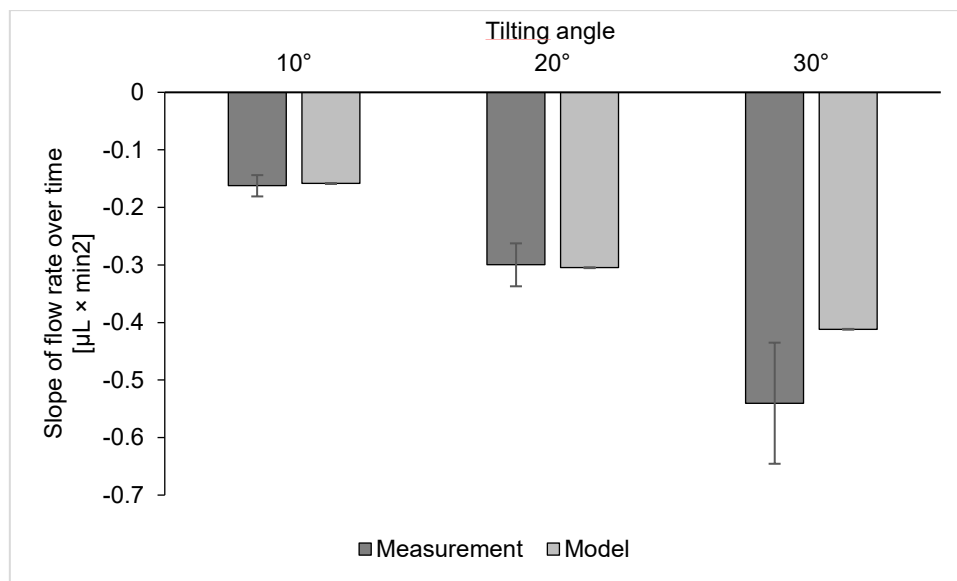
The time-stepping scheme uses the previously established flow rates to update the volume in drops and reservoirs iteratively over time. In turn, this affects the pressure in the system, i.e.,

the resulting flow rate. Ultimately, the flow transients for a given tilting angle are found, with which we derive the maximum flow rate and the time during which a specific angle can be held (Figure 4 simulation results).

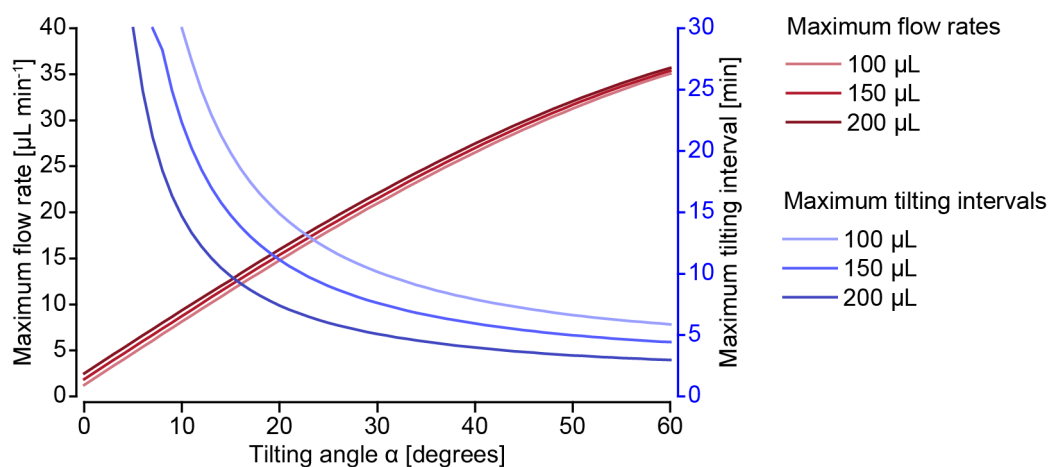
2.7.1 Supplementary Figures



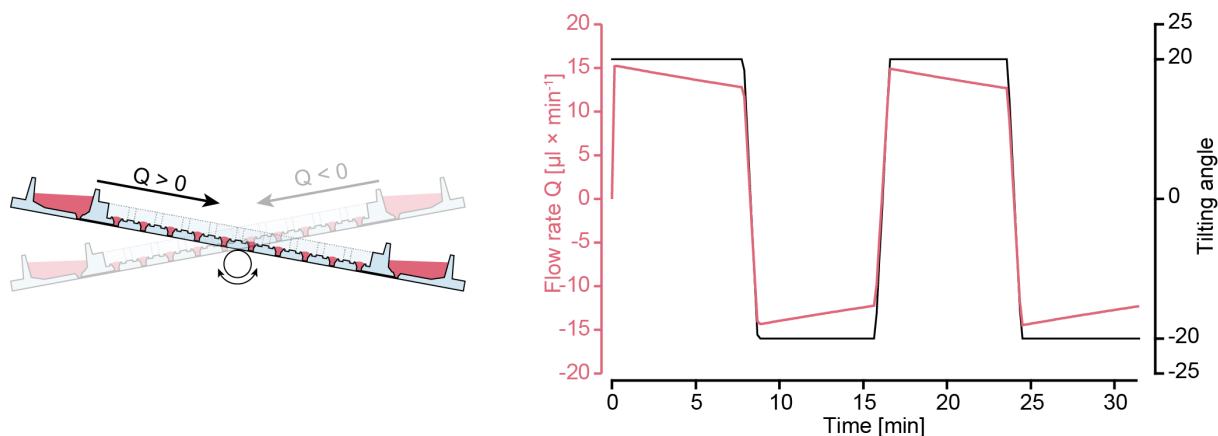
Supplementary Figure 1: Absorption of substances in polydimethylsiloxane (PDMS) and polystyrene (PS). (A) NileRed and (B) Cy3-conjugated antibodies were loaded into PDMS and PS chips and were incubated for 24 h. Bright-field and fluorescence ($\lambda_{\text{Ex}} = 565$ nm/ $\lambda_{\text{Em}} = 610/75$ nm) images were taken. Fluorescence intensity profiles illustrate the distribution of the substances within the channels and into the wall materials over time. Sampling at $t = 0$ h was performed as fast as possible after filling the channels, but there was already diffusion into the wall material visible.



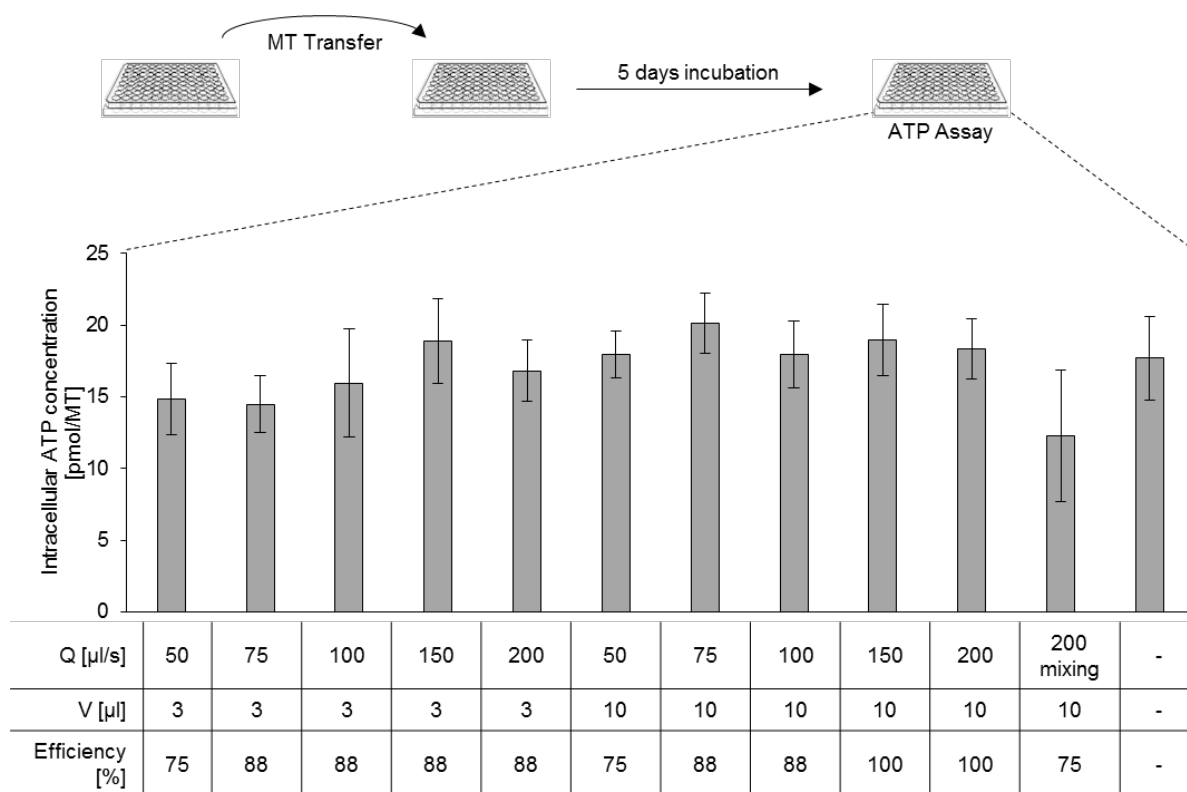
Supplementary Figure 2: Slopes of measured and modeled flow rates as a function of time at different tilting angles. The slopes of the measured flow rates match the modeled flow rates for tilting angles of 10° and 20°. The measured slope at 30° is steeper than the modeled one but also has a larger standard deviation than all other slopes.



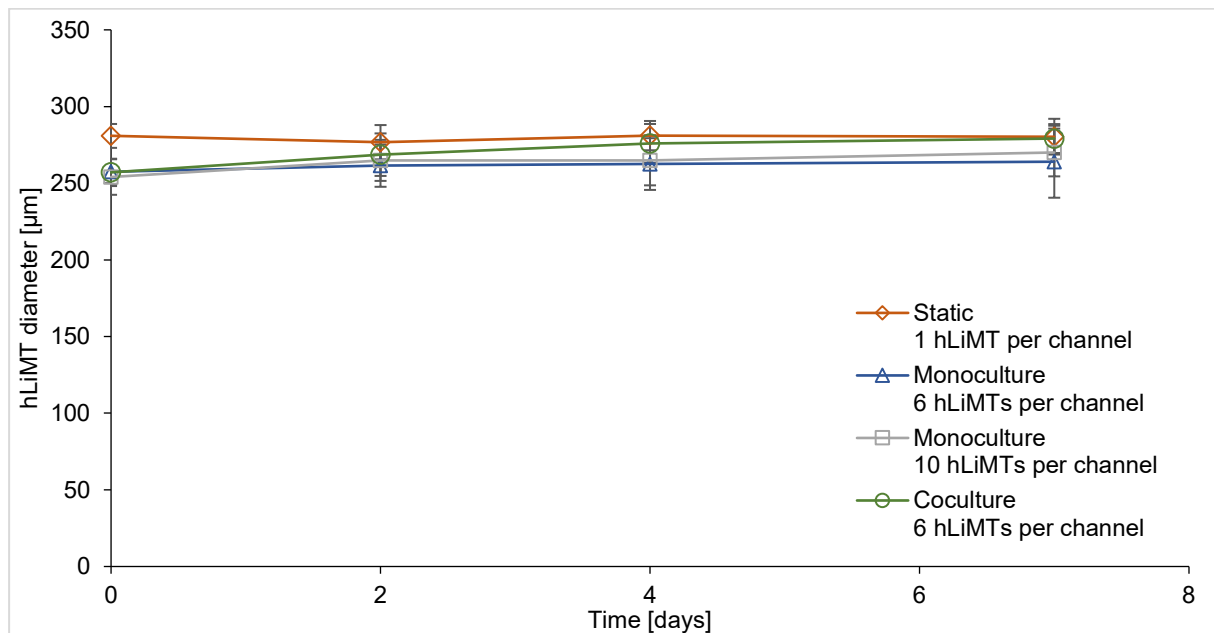
Supplementary Figure 3: The maximum flow rate and tilting interval until drainage of the top reservoir at 37 °C as a function of the tilting angle was calculated for initial liquid volumes of 100, 150 and 200 μL . Lower liquid volumes result in lower flow rates and shorter applicable tilting intervals.



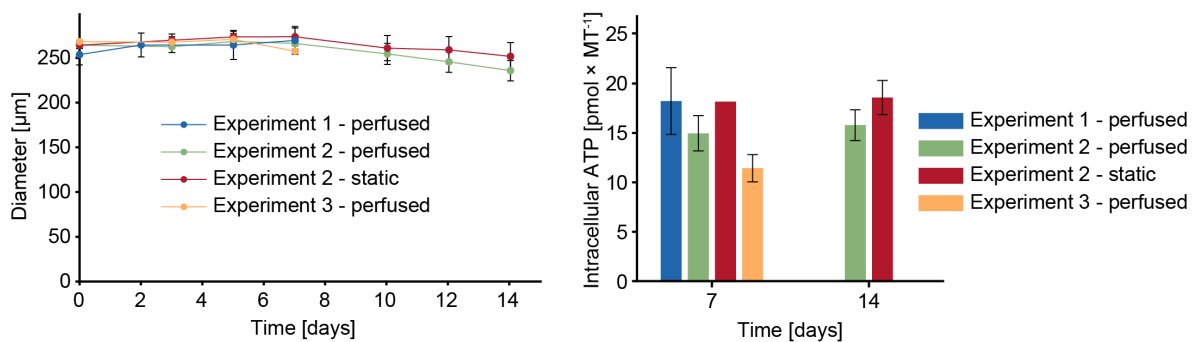
Supplementary Figure 4: Bidirectional flow rate through the channel upon repeated tilting over two tilting cycles with following parameters: tilting angle $\alpha = 20^\circ$, tilting interval = 7 min, transition time = 50 s.



Supplementary Figure 5: Viability of human liver microtissues (hLiMTs) after transfer between two microtiter plates. hLiMTs were taken up with different uptake flow rates Q and uptake volumes V using an automatic liquid handling system (Hamilton STAR, Hamilton Bonaduz AG, Bonaduz, Switzerland). ATP-dependent viability shows no negative impact of high flow rates on hLiMTs during transfer as compared to the negative control that did not experience transfer. Transfer efficiency of up to 100 % could be achieved by taking up a volume V of 10 μL with a flow rate Q of 150 – 200 $\mu\text{l/s}$ ($n = 8$ hLiMTs per data point; data represented as mean \pm SD).



Supplementary Figure 6: Diameter of hLiMTs under static and perfused conditions over time. hLiMTs were cultured as one MT per well on a microtiter plate (orange) or as multiple MTs per channel on chip. Monoculture conditions included six (blue) or ten (grey) hLiMTs, and co-culture conditions (green) included six hLiMTs with four tumor MTs. The size of hLiMTs remained constant under all conditions over the experiment time ($n = 8 - 40$ hLiMTs per data point; data represented as mean \pm SD).



Supplementary Figure 7: Reproducibility of microtissue culturing within the microfluidic chip. 10 hLiMTs per channel were cultured in the microfluidic chip over up to 14 days in independent experiments in two different labs. (A) hLiMT diameter was tracked over time and (B) intracellular ATP concentrations were measured on days 7 and 14 ($n = 40 - 80$ hLiMTs per data point; data represented as mean \pm SD).

2.7.2 Supplementary Movies

Supplementary Movie 1: MT loading procedure using a 96-channel semi-automated pipetting system (VIAFLO 96/384, Integra Biosciences, Zizers, Switzerland). 80 MTs could be transferred from 96-well microtiter plates into the microfluidic chip in eight pipetting steps.

Supplementary Movie 2: Fully automated MT loading using a liquid handling robot (Hamilton STAR, Hamilton Bonaduz AG, Bonaduz, Switzerland), equipped with eight pipetting channels. Two types of MTs were transferred from individual 96-well microtiter plates for a co-culture configuration on the microfluidic chip.

Supplementary Movie 3: Rotating 3D animation of a tumor MT consisting of GFP-tagged MDA-MB-361 cells. The image stack was obtained on chip using an Olympus FV-MPERS system, equipped with a Newport SpectraPhysics DS+ 2-photon-laser and a XLPLN25XSVM (25x, NA 1.0) water-immersed lens. ($\lambda_{\text{Ex}} = 900 \text{ nm}$). The spatial resolution was $0.63 \times 0.63 \times 2 \mu\text{m}^3$. 119 images were acquired along the z-direction to cover the entire spheroid.

2.8 References

1. Marx, U., et al., Biology-inspired microphysiological system approaches to solve the prediction dilemma of substance testing. *ALTEX*, **33**, 272-321 (2016).
2. Bhatia, S.N. and D.E. Ingber, Microfluidic organs-on-chips. *Nature Biotechnology*, **32**, 760 (2014).
3. Benam, K.H., et al., Small airway-on-a-chip enables analysis of human lung inflammation and drug responses in vitro. *Nat Methods*, **13**, 151-157 (2016).
4. Esch, M.B., et al., Modular, pumpless body-on-a-chip platform for the co-culture of GI tract epithelium and 3D primary liver tissue. *Lab Chip*, **16**, 2719-2729 (2016).
5. Bauer, S., et al., Functional coupling of human pancreatic islets and liver spheroids on-a-chip: Towards a novel human ex vivo type 2 diabetes model. Vol. 7.(2017)
6. Edington, C.D., et al., Interconnected Microphysiological Systems for Quantitative Biology and Pharmacology Studies. *Sci Rep*, **8**, 4530 (2018).
7. Balijepalli, A. and V. Sivaramakrishnan, Organs-on-chips: research and commercial perspectives. *Drug Discov Today*, **22**, 397-403 (2017).
8. Ewart, L., et al., Navigating tissue chips from development to dissemination: A pharmaceutical industry perspective. *Exp Biol Med (Maywood)*, **242**, 1579-1585 (2017).
9. Zhang, B. and M. Radisic, Organ-on-a-chip devices advance to market. *Lab Chip*, **17**, 2395-2420 (2017).
10. Wang, Y.I., et al., Multiorgan Microphysiological Systems for Drug Development: Strategies, Advances, and Challenges. *Advanced Healthcare Materials*, **7**, (2018).
11. Berthier, E., E.W. Young, and D. Beebe, Engineers are from PDMS-land, Biologists are from Polystyrenia. *Lab Chip*, **12**, 1224-1237 (2012).
12. Ren, K., J. Zhou, and H. Wu, Materials for Microfluidic Chip Fabrication. *Accounts of Chemical Research*, **46**, 2396-2406 (2013).
13. Esch, E.W., A. Bahinski, and D. Huh, Organs-on-chips at the frontiers of drug discovery. *Nature reviews. Drug discovery*, **14**, 248-260 (2015).
14. Maass, C., et al., Multi-functional scaling methodology for translational pharmacokinetic and pharmacodynamic applications using integrated microphysiological systems (MPS). *Integrative biology : quantitative biosciences from nano to macro*, **9**, 290-302 (2017).

15. Prantil-Baun, R., et al., Physiologically Based Pharmacokinetic and Pharmacodynamic Analysis Enabled by Microfluidically Linked Organs-on-Chips. *Annual review of pharmacology and toxicology*, **58**, 37-64 (2018).
16. Kim, J.Y., et al., 96-well format-based microfluidic platform for parallel interconnection of multiple multicellular spheroids. *J Lab Autom*, **20**, 274-282 (2015).
17. Kim, J.Y., et al., 3D spherical microtissues and microfluidic technology for multi-tissue experiments and analysis. *J Biotechnol*, **205**, 24-35 (2015).
18. Drewitz, M., et al., Towards automated production and drug sensitivity testing using scaffold-free spherical tumor microtissues. *Biotechnology Journal*, **6**, 1488-1496 (2011).
19. Fennema, E., et al., Spheroid culture as a tool for creating 3D complex tissues. *Trends in Biotechnology*, **31**, 108-115 (2013).
20. Lin, R.Z. and H.Y. Chang, Recent advances in three-dimensional multicellular spheroid culture for biomedical research. *Biotechnol J*, **3**, 1172-1184 (2008).
21. Young, E.W., Cells, tissues, and organs on chips: challenges and opportunities for the cancer tumor microenvironment. *Integrative biology : quantitative biosciences from nano to macro*, **5**, 1096-1109 (2013).
22. Moshksayan, K., N. Kashaninejad, and M. Saidi, Inventions and Innovations in Preclinical Platforms for Cancer Research. *Inventions*, **3**, 43 (2018).
23. van Midwoud, P.M., et al., Comparison of biocompatibility and adsorption properties of different plastics for advanced microfluidic cell and tissue culture models. *Analytical chemistry*, **84**, 3938-3944 (2012).
24. Wang, J.D., et al., Quantitative Analysis of Molecular Absorption into PDMS Microfluidic Channels. *Annals of Biomedical Engineering*, **40**, 1862-1873 (2012).
25. van Meer, B.J., et al., Small molecule absorption by PDMS in the context of drug response bioassays. *Biochemical and Biophysical Research Communications*, **482**, 323-328 (2017).
26. Kozyra, M., et al., Human hepatic 3D spheroids as a model for steatosis and insulin resistance. *Scientific Reports*, **8**, 14297 (2018).
27. Wikswo, J.P., Markov, Dmitry A., Samson, Philip C., Block III, Frank E., Schaffer, David K., Reiserer, Ronald S., Interconnections of multiple perfused engineered tissue constructs and microbioreactors, multi-microformulators and applications of the same. Vanderbilt University (Nashville, TN, US): United States. (2018)

28. Song, H., Y. Wang, and K. Pant, System-level simulation of liquid filling in microfluidic chips. *Biomicrofluidics*, **5**, 24107 (2011).
29. Marimuthu, M., et al., Multi-size spheroid formation using microfluidic funnels. *Lab Chip*, **18**, 304-314 (2018).
30. Heo, Y.S., et al., Characterization and resolution of evaporation-mediated osmolality shifts that constrain microfluidic cell culture in poly(dimethylsiloxane) devices. *Anal Chem*, **79**, 1126-1134 (2007).
31. Frohlich, E., et al., Comparison of two in vitro systems to assess cellular effects of nanoparticles-containing aerosols. *Toxicol In Vitro*, **27**, 409-417 (2013).
32. Yu, J., et al., Quantitative Systems Pharmacology Approaches Applied to Microphysiological Systems (MPS): Data Interpretation and Multi-MPS Integration. *CPT Pharmacometrics Syst Pharmacol*, **4**, 585-594 (2015).
33. Zeilinger, K., et al., Scaling Down of a Clinical Three-Dimensional Perfusion Multicompartment Hollow Fiber Liver Bioreactor Developed for Extracorporeal Liver Support to an Analytical Scale Device Useful for Hepatic Pharmacological In Vitro Studies. *Tissue Engineering Part C: Methods*, **17**, 549-556 (2011).
34. Tostões, R.M., et al., Human liver cell spheroids in extended perfusion bioreactor culture for repeated-dose drug testing. *Hepatology*, **55**, 1227-1236 (2012).

3 PREDICTING METABOLISM-RELATED DRUG- DRUG INTERACTIONS USING A MULTI-TISSUE MICROPHYSIOLOGICAL SYSTEM

Manuscript in preparation for submission.

Christian Lohasz,* Flavio Bonanini,* Kasper Renggli, Olivier Frey, and Andreas Hierlemann.

*Both authors contributed equally.

3.1 Abstract

Drug-drug interactions (DDIs) occur, when the pharmacological activity of one drug is altered by a second drug. As multimorbidity and polypharmacotherapy are becoming more and more common due to the increasing age of the population, the risk of DDIs is massively increasing. DDIs mostly involve multiple organs in the human body, so that novel in vitro testing methods are needed to capture such multi-organ-level events. Here, we present a microfluidic chip for culturing 3D microtissues (MTs) that are fluidically connected through the culture medium. Human liver microtissues (hLiMTs) were combined with tumor microtissues (TuMTs) and treated with drug combinations that are known to cause DDIs in vivo. We showed that our testing system was able to capture and quantify DDIs upon co-administration of the anti-cancer prodrugs Cyclophosphamide or Ifosfamide with the antiretroviral drug Ritonavir. Dosage of Ritonavir inhibited hepatic metabolization of the two prodrugs to different extents and decreased their efficacy in acting on the TuMTs. The flexible MT compartment design, the use of polystyrene as chip material, and the assembly of several chips in stackable plates render the system a promising tool to test a broad variety of drug combinations with the aim to identify possible DDIs during drug development.

3.2 Introduction

Drug-drug interactions (DDIs) describe events, when the pharmacological activity of one drug is altered by the concomitant administration of a second drug. As multimorbidity, and thus polypharmacotherapy, is becoming more and more common with increasing age of the population, the risk of DDIs is also massively rising.¹ In fact, DDIs are accountable for 10 – 20% of adverse drug reactions (ADRs) in developed countries, which result in an increased number and/or duration of hospitalizations.²⁻⁵

Pharmacokinetic DDIs arise upon modulation of the absorption, distribution, and metabolism or excretion (ADME) properties of one drug by co-administration of another drug, and can lead to several-fold changes of drug plasma concentrations with potentially life-threatening consequences.⁶ Most commonly, a perpetrator drug modulates the metabolism of a victim drug by chemical inhibition or transcriptional induction of drug-metabolizing enzymes. In both cases, such an interaction leads to an altered metabolic fate of the victim drug.⁷ The clinical implications of such interactions can result in a lack of efficacy, especially in the context of so-

called prodrugs. Prodrugs are drug variants with enhanced solubility or lifetime, which rely on *in vivo* bioconversion to exert their pharmacological activity.⁸ Positive treatment outcomes in prodrug therapies strongly depend on the ability of the patient to endogenously bio-activate the prodrug compound to its pharmacologically active metabolite(s).⁹

Drug metabolism predominantly occurs in the liver and is mainly catalyzed by enzymes of the Cytochrome P450 (CYP) family. These enzymes oxidize, reduce and hydrolyze a wide range of drugs or chemical entities. Therefore, it does not come as a surprise, that inhibition or induction of CYP enzymes is largely involved in clinical DDIs and has led to severe ADRs and the withdrawal of multiple drugs from the market.¹⁰ In many cases, DDIs manifest themselves in secondary organs, to which liver-generated metabolites are transported through systemic circulation. Such tissues include kidney, heart, brain, gut and lungs, and drug target tissues, such as tumors.¹¹

Oncology patients are considered especially prone to toxic DDI events owing to (i) the wide use of anticancer prodrugs,^{12, 13} (ii) the inherent toxicity of anticancer agents, and their very narrow therapeutic index, (iii) the likelihood of cancer patients to receive many different medications for the management of other illnesses,¹⁴ and (iv) the increasing use of combination therapies with more than one anti-cancer medication.¹⁵ Hence, clinicians are confronted with the growing risk of prescribing drug combinations that can inadvertently lead to severe clinical implications.¹⁶ Additionally, genetic polymorphisms in the liver can lead to individual patterns of CYP metabolism for different patients.¹⁷ Management of DDIs is, therefore, crucial in oncology therapy, where the altered metabolic competence of patients can lead to potentially life-threatening clinical scenarios.^{14, 18}

In response to the occurrence of DDIs, pharmaceutical companies are required to incorporate extensive pre-clinical metabolic investigations to predict possible hazardous drug combinations. However, current conventional pre-clinical methodologies often fail to obtain information relevant for use with human patients. This shortcoming is mostly attributed to the limited potential of animal models in predicting clinical DDIs as a result of differences in metabolization enzymes and transporters.¹⁹ Human cell-based *in vitro* systems are, therefore, routinely used alongside animal models in an attempt to predict possible DDIs.²⁰ In line with a guidance document on *in vitro* DDI, released by the US Food and Drug Administration, these testing systems usually make use of liver microsomes, isolated CYP enzymes, or single cell types in static two-dimensional (2D) cultures.²¹ These systems often fail to recapitulate many

of the complex biological and systemic phenomena associated with clinical DDI events. As a promising alternative to conventional *in vitro* models, emerging organ-on-a-chip systems offer the potential to reproduce key aspects of human organs, such as three-dimensional (3D) tissue architecture, cellular composition, and mechanical cues. Given the key role of hepatic drug metabolism in determining therapy outcomes, significant efforts have been devoted to developing more predictive *in vitro* liver models by integrating hepatocytes with non-parenchymal cells and introducing oxygen/nutrient gradients and shear stress.²² However, these liver models still do not include complex interactions between different tissues of the body, which limits their potential to accurately predicting DDIs that occur on a systemic level.^{11, 23} Including and interfacing multiple organs in advanced *in vitro* co-culture systems enables to capture a large number of biological effects exerted by biologically active compounds and their metabolites.²⁴ Such multi-organ devices have been used to simultaneously evaluate drug efficacy and safety aspects on a systemic level.²⁴ Multi-organ systems represent a potential solution to capture the full extent – ranging from metabolizing organs to drug target organs – of complex DDI events and to predict the safety of critical drug combinations.

Here, we present the application of a previously described microfluidic multi-organ chip to detect and predict metabolism-related DDIs.^{25, 26} Taking anticancer therapies as a prime example for DDIs, we combined primary human liver microtissues (hLiMTs), featuring metabolic competence, with human cell line-derived HCT116 tumor microtissues (TuMTs) as a drug target organ. Two commonly used anticancer prodrugs, Cyclophosphamide (CP) and Ifosfamide (IFF),^{27, 28} were administered in combination with Ritonavir (RTV). RTV is widely used as part of highly active antiretroviral therapy (HAART) against HIV and is known for its potent inhibition of the CYP isoform 3A4.²⁹ This inhibition was previously reported to affect the bioactivation of CP and IFF treatment.³⁰⁻³² We show that our testing system was capable to accurately detect DDIs between the compounds. Furthermore, the differential severity of DDI between CP+RTV and IFF+RTV, which is based on different activation mechanisms of CP and IFF, could be quantified by analysis of the TuMTs. The usage of a gravity-driven microfluidic device for the application here renders the system user-friendly and scalable, which facilitates an implementation in industrial settings.

3.3 Materials and methods

3.3.1 Cell culture

The human colorectal cancer cell line HCT116 (ATCC, Manassas, VA, USA) was maintained in cell-culture medium consisting of RPMI 1640 (Gibco, Thermo Fisher Scientific, Steinhausen, Switzerland) with 10% fetal bovine serum (Sigma-Aldrich, Buchs, Switzerland) and 1% penicillin/streptomycin (Sigma-Aldrich). To form tumor microtissues (TuMTs), the cells were seeded into Akura™ 96-well plates (InSphero AG, Schlieren, Switzerland) with an initial density of 200 cells per well. The plates were centrifuged at $250 \times g$ for 2 min to accumulate the cells at the bottom of the wells. The plates were then positioned at an angle of approx. 20° to center all cells in one corner of the wells. The cells adhered to each other and formed uniform TuMTs within three days of incubation.

3D InSight™ Liver Microtissues (hLiMTs) consisting of primary human hepatocytes were generated by InSphero AG and were provided ready to use in 96-well microtiter plates. They were maintained in human liver maintenance medium TOX (InSphero AG).

Both MT types were cultured under mammalian cell culture conditions (37°C , 5% CO_2 , 90% humidity) with medium exchanges every 48 to 72 h. On-chip experiments in this study generally started 2 – 4 days after complete aggregation of cells into microtissues.

3.3.2 Microfluidic chip operation

The microfluidic chips used for this study were provided by InSphero AG. They were received sterilized and coated with a hydrophilic and cell-repellent coating to avoid MT attachment. The microfluidic chip design and development was already described in detail elsewhere.²⁶ Briefly, the chip features two parallel, independent channels. The channels interconnect ten MT compartments each and feature medium reservoirs at both ends. The MT compartments are open at the top, which facilitates loading, manipulation, and harvesting of MTs. Perfusion through the channels is gravity-driven upon tilting of the chip owing to a height difference between the two opposing reservoirs as previously described.^{33, 25, 34, 26} MTs were transferred into the chip in a standard micropipette tip. Upon touching the top of the MT compartment with the pipette tip, the MT sediments through the liquid column to the bottom of the compartment. After loading of all MT compartments, medium was exchanged by tilting the chip and removing

all medium from the lower reservoir. A standard operation volume of 150 μ L of fresh cell-culture medium was then added to the reservoir. Visual checks confirmed the presence of all MTs within the respective MT compartments and their integrity before sealing the chip with custom-cut, pressure-sensitive adhesive film to avoid medium evaporation. The adhesive film featured holes enabling access to the reservoirs and allowing for medium exchanges and drug treatments during the experimental runs. Parallelized experiments were achieved by assembling four chips into a handling frame (microfluidic ChipShop, Jena, Germany) so that ANSI/SLAS standards in terms of microplate footprint dimensions³⁵ and well positions³⁶ were met. Up to four assembled plates were then stacked and operated on a single, programmable tilting stage (InSphero AG), allowing for experiments with 320 MTs distributed over 32 individual channels under identical or variable culturing conditions. During experiments, the chips were repeatedly tilted in both directions by 20°, with a waiting time of 7 min at the maximum tilting angles and a tilting time of 25 sec from one side to the other.

3.3.3 Drug treatment of microtissues

All drugs used for experiments were obtained from Sigma-Aldrich. A stock solution of Cyclophosphamide (CP) was prepared in water. Due to its lower solubility, Ifosfamide (IF) was dissolved directly in cell-culture medium. Ketoconazole (KCZ) and Ritonavir (RTV) were dissolved in *N,N*-dimethylformamide (DMF; Sigma-Aldrich). CP and IF stock solutions were prepared once and stored at -80° C. 1000x stock solutions of KCZ and RTV were prepared once a week and were stored at 4° C.

For drug treatments, single drugs or drug combinations were prepared in cell-culture medium and diluted to the respective experimental concentrations. All treatment conditions were equilibrated to the DMF concentrations used for the conditions including KCZ or RTV. The maximum DMF concentration used was 0.1%. The compound-supplemented cell-culture medium was administered to MTs on microwell plates or in microfluidic chips through a complete medium exchange. Over the given experimental period, the medium was exchanged every two to three days. When exchanging medium, the medium was collected and stored at -20° C for further analysis.

3.3.4 Biochemical assays

Human albumin – a marker of general liver functionality – was quantified in the supernatant that was collected upon exchanging the medium. For albumin quantification, samples were frozen at different time points and stored for complete analysis using a Human Albumin ELISA Kit (Bethyl Laboratories, Inc., Montgomery, TX, USA) following the manufacturer's protocol. Cytochrome P450 (CYP) 3A4 activity of hLiMTs was measured using the P450-Glo™ CYP3A4 Assay (Promega, Dübendorf, Switzerland) with Luciferin-IPA as substrate. CYP3A4 activity was measured on static microwell plates, or directly on chip under perfusion conditions, following the manufacturer's guidelines. As a lytic endpoint assay, intracellular adenosine triphosphate (ATP) concentrations were measured to have an indicator for MT viability with the CellTiter-Glo® 3D Cell Viability Assay (Promega). MTs were transferred from the chips back into microwell plates directly before performing the assay according to the manufacturer's protocol.

3.3.5 CYP activity measurements

CYP activity was measured by conversion of CYP-isoform-specific substrates. Stock solutions of these substrates in DMF were reconstituted in hLiMM-TOX directly before use. At the defined days, hLiMTs were incubated in hLiMM-TOX containing 26 μ M Phenacetin, 9 μ M Diclofenac, 9 μ M Bufuralol and 3 μ M Midazolam, or 100 μ M Bupropion, 5 μ M Coumarin and 20 μ M Mephrelynoin. After 24 h of incubation time, 50 μ L of the supernatant was snap-frozen and stored until all samples were shipped to Pharmacelsus GmbH, Saarbrücken, Germany, where the compound metabolites were quantified by liquid chromatography – mass spectrometry (LC-MS).

3.3.6 Imaging

Bright-field images of MTs in microwell plates or on chip were acquired using one of the following systems: (i) an inverted microscope (DMI-6000B; Leica Microsystems AG, Heerbrugg, Switzerland) with a 5 \times objective, a CCD camera (DFC-340-FX; Leica), and a stage top incubator enabling long-term life imaging, or (ii) a Cell³iMager Neo cc-3000 (Screen Holdings Co., Ltd, Kyoto, Japan). Images acquired with both systems were processed using ImageJ software.

3.3.7 Mass Spectrometry

To assess hepatic metabolism of CP and IFF, hLiMTs in microwell plates were incubated in 25 μ L hLiMM-TOX containing 1 mM CP or IFF, with or without RTV. Supernatant samples were taken after 24, 48, and 72 h from individual wells: 5 μ L of supernatant was snap-frozen into 45 μ L of hLiMM-TOX on dry ice. All samples were shipped to Admescope Oy, Oulu, Finland, where they were semiquantitatively analyzed by ultra-performance liquid chromatography – mass spectrometry (UPLC-MS).

3.3.8 Statistics

Datasets are generally presented as mean values with error bars representing the standard deviation (SD), unless otherwise indicated. If no error bars are shown, the SD is smaller than the symbol indicating the mean value. Sample sizes are mentioned within the respective figure captions. Pairs of treatment groups were compared using t-tests ($\alpha = 0.05$). Raw effect sizes were determined by calculation of the difference between group means, and their 95% confidence intervals are given.

3.4 Results

3.4.1 Microfluidic chip system

To establish an *in vitro* testing system for the prediction of metabolism-related drug-drug-interaction, a previously characterized microfluidic chip was used.²⁶ The chip was fabricated by injection molding using polystyrene to limit unspecific adsorption and/or absorption of soluble molecules, and to allow for standardized fabrication. The chip design was specifically optimized for the culturing and analysis of 3D microtissues under perfusion conditions. Several different organotypic microtissue types can be inserted into the microtissue compartments along a channel, which enables molecule exchange and signaling through the liquid phase. The selection and combination of a set of relevant organotypic microtissues enables an *in vitro* recapitulation of healthy processes or diseases in a human body involving key organs. Off-chip generation of microtissues in microwell plates allows for quality control of each MT before transfer into the chip. Perfusion is achieved by tilting, which yields a gravity-driven,

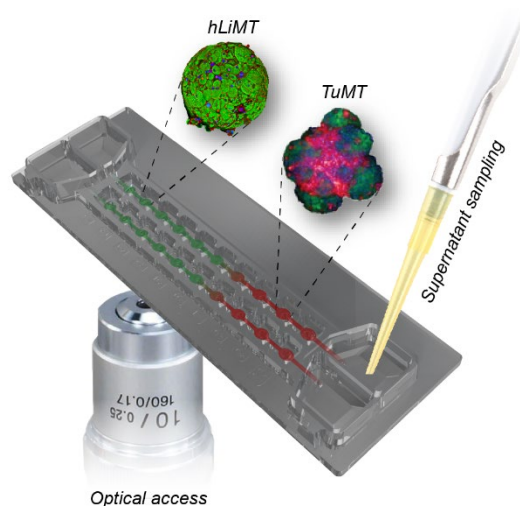


Figure 1: Illustration of the microfluidic microtissue culture chip. Different microtissue models, such as human liver microtissues (hLiMTs; green) and tumor microtissues (TuMTs; red) can be loaded into designated compartments along microfluidic channels (indicated in red and green). Microtissues are monitored on-chip using microscopy, or by analyzing the supernatant that can be sampled from the reservoirs.

bidirectional flow in the channel between the two reservoirs at the ends, as has previously been described.^{33, 26} The maximum tilting angle of the chip was set to 20°, resulting in a flow rate of approx. 20 $\mu\text{L}/\text{min}$. On-chip monitoring of the state of the MTs was possible by bright-field microscopy and by sampling of the supernatant from the medium reservoirs. Moreover, off-chip analyses were performed after harvesting the MTs for lytic endpoint assays.

3.4.2 Characterization of microtissue models

As the liver is the organ that predominantly metabolizes drugs in the human body, liver microtissues are a crucial component of an *in vitro* testing system to predict metabolism-related drug effects. We used human liver microtissues (hLiMTs) consisting of primary hepatocytes. To limit donor-to-donor variability and to ensure reproducibility of experiments, hLiMTs were formed from a pool of ten hepatocyte donors (5 male and 5 female). To ensure the metabolic capacity of the multi-donor hLiMTs, as it has previously been described for static culture conditions,³⁷ their viability and functionality were assessed for 14 days on chip under perfusion conditions. The obtained data were compared to those of hLiMTs cultured in parallel under static conditions in microwell plates (Figure 2).

ATP-dependent viability of hLiMTs was measured two days prior to loading the hLiMTs into the microfluidic device and in 7 day-intervals after loading. Intracellular ATP concentrations showed similar values for static and perfusion conditions with a peak after 7 days of culturing (Figure 2A). Secreted albumin concentrations in the cell culture supernatant slightly decreased over the 14-day culturing period under static and perfusion conditions. The decrease was more pronounced for the hLiMTs cultured in the microfluidic chip (Figure 2B). Size measurements

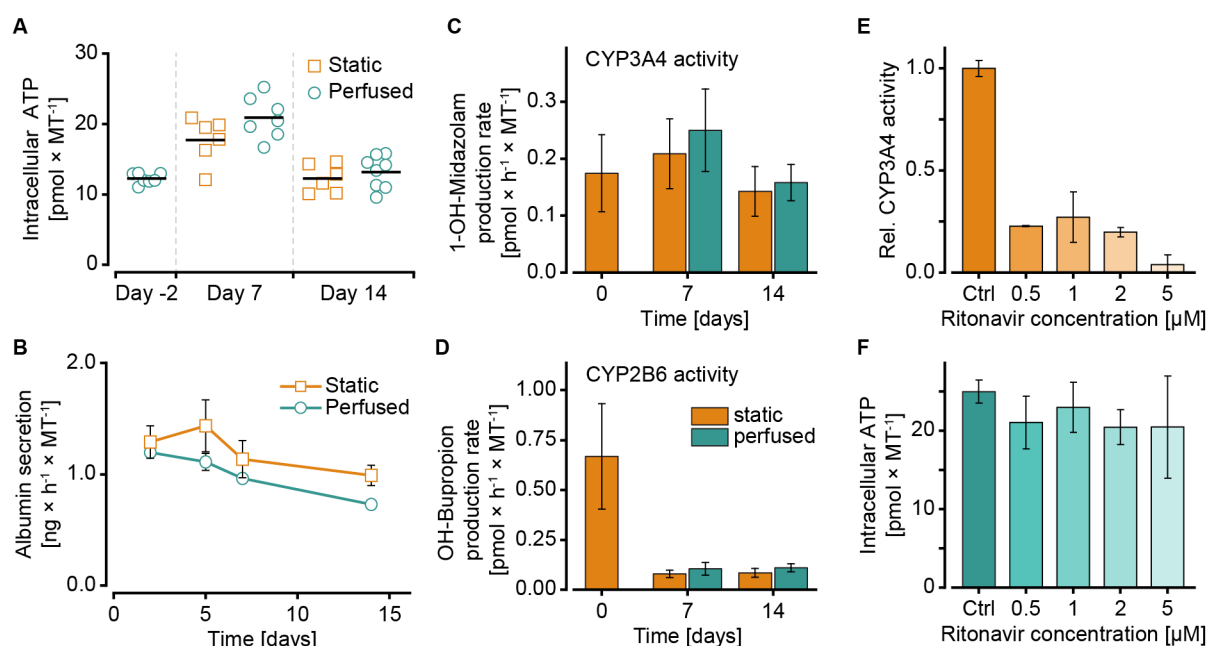


Figure 2: Characterization of primary human liver microtissues (hLiMTs) under static well-plate conditions and under perfusion conditions on chip over 14 days. **(A)** ATP-dependent viability of hLiMTs ($n = 6 - 8$ hLiMTs; — = mean). **(B)** Albumin secretion, measured in supernatant samples ($n = 4$ samples; data represented as mean \pm SD). **(C)** Cytochrome P450 (CYP) 3A4 activity, measured by conversion of Midazolam to 1-OH-Midazolam, and **(D)** CYP2B6 activity, measured conversion of Bupropion to OH-Bupropion. Generated metabolites were quantified by LC-MS analysis ($n = 3 - 6$ samples; data represented as mean \pm SD). **(E)** Inhibition of CYP3A4 activity and **(F)** ATP-dependent viability of hLiMTs after three days of exposure to Ritonavir (RTV; $n = 3 - 4$ hLiMTs; data represented as mean \pm SD).

of hLiMTs also showed a similar trend (decreasing size) as observed in albumin measurements (Suppl. Figure 1).

The activity of the most relevant cytochrome P450 (CYP) isoenzymes was measured in terms of conversion rate of CYP-isoform-specific substrates over a 24 h incubation period. Two CYP isoforms, 3A4 and 2B6, are predominantly involved in the metabolism of Cyclophosphamide and Ifosfamide and are, hence, of special interest. CYP3A4 activity remained stable over a culture period of 14 days and exhibited similar values under static and perfused conditions (Figure 2C). CYP2B6 activity rapidly decreased between day 0 and day 7 and then stabilized at low activity levels until day 14 under both culture conditions (Figure 2D). The specific activity of additional CYP isoforms that are involved in xenobiotic metabolism is shown in Suppl. Figure 2. Perfusion conditions increased the activity of CYP1A2, CYP2C9, and CYP2C19 in comparison to static conditions, while CYP2C8 and CYP2D6 showed similar activity under both culture conditions.

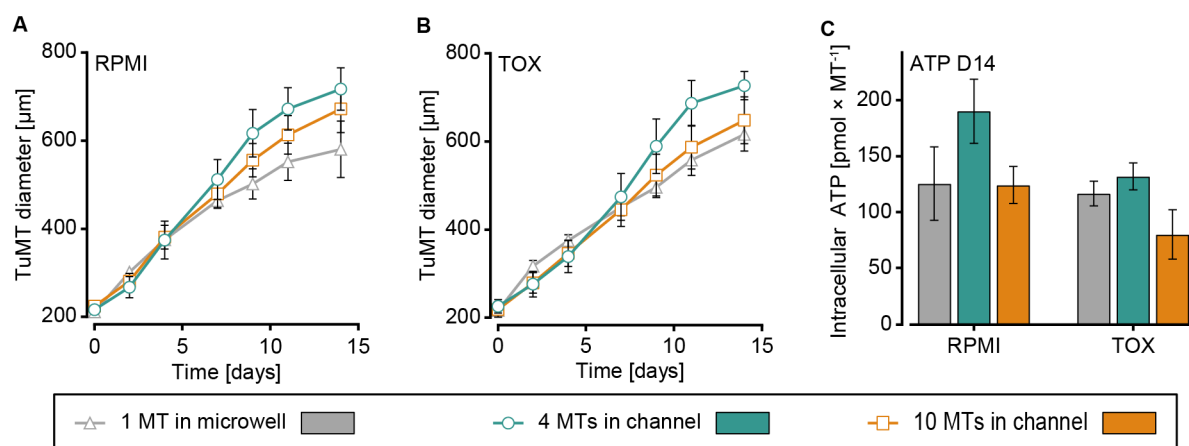


Figure 3: Characterization of tumor microtissues (TuMTs) over 14 days under static conditions with one MT per microwell, or perfusion conditions with four or ten MTs per channel. **(A)** Growth of TuMTs in their standard RPMI-based cell-culture medium, and **(B)** in human-liver-maintenance medium (hLiMM) TOX. **(C)** ATP-dependent viability of TuMTs after 14 days of culturing in different media and under static or perfusion conditions ($n = 6 - 30$ TuMTs in 6 independent microwells or 3 independent channels; data represented as mean \pm SD).

A major trigger of pharmacokinetic DDIs is the xenobiotic inhibition or induction of CYP enzymes. To assess the sensitivity of our hLiMTs to such modulating stimuli, we measured CYP3A4 activity after three days of microtissue exposure to different doses of Ritonavir and Ketoconazole, which are both known CYP3A4 inhibitors. Both compounds exhibited potent inhibitory effects at doses starting at $0.5 \mu\text{M}$ (Figure 2E and Suppl. Figure 3). Ritonavir concentrations up to $5 \mu\text{M}$ did not affect hLiMT viability (Figure 2F), while a dose-dependent decrease of hLiMT viability was observed upon exposure to Ketoconazole at concentrations of up to $15 \mu\text{M}$ (Suppl. Figure 3).

As a second tissue type, human-cell-line-derived HCT 116 tumor microtissues (TuMTs) were used as an *in vitro* model for cancer tissue in our testing system. The most characteristic feature of tumor tissue is the lack of contact inhibition and, therefore, its uncontrolled growth. Hence, we characterized the property of our TuMTs to grow over 14 days. As we wanted later to combine tumor with liver tissue models in the microfluidic chip, we assessed the tumor growth behavior in two different cell culture media: (i) in standard RPMI-based growth medium, and (ii) in serum-free human liver maintenance medium (hLiMM)-TOX. For both media, static culture conditions with single TuMTs in microwells were compared to perfusion culture conditions on chip with four or ten TuMTs in microfluidic channels. Figure 3 shows the TuMT diameters measured over a period of 14 days. The growth characteristics of TuMTs were similar in both culture media. Under all culture conditions, the growth curves overlapped during the

first seven days. After these initial seven days, slight differences between the growth curves became apparent for the different culture conditions: TuMTs cultured statically in microwell plates increased in size 2.7-fold (RPMI) and 2.8-fold (TOX). Perfusion culture conditions with four MTs per channel yielded a 3.3-fold (RPMI) and 3.2-fold (TOX) size increase, while a 3-fold increase was observed in both culture media in a system featuring ten MTs per channel. ATP-dependent viability of TuMTs on day 14 of the experiment showed similar trends for the two media, with largest growth values obtained for MTs cultured under perfusion conditions with four MTs in a channel. Notably, perfused TOX conditions produced lower intracellular ATP values than perfusion RPMI conditions, while microwell conditions were similar for both media.

3.4.3 Interaction of multiple organs on chip

After independent characterizations of hLiMTs and TuMTs, both cell models were combined in the microfluidic chip using hLiMM-TOX as the common cell-culture medium. The channels of our microfluidic chip were loaded with six hLiMTs as metabolizing organs, and four TuMTs

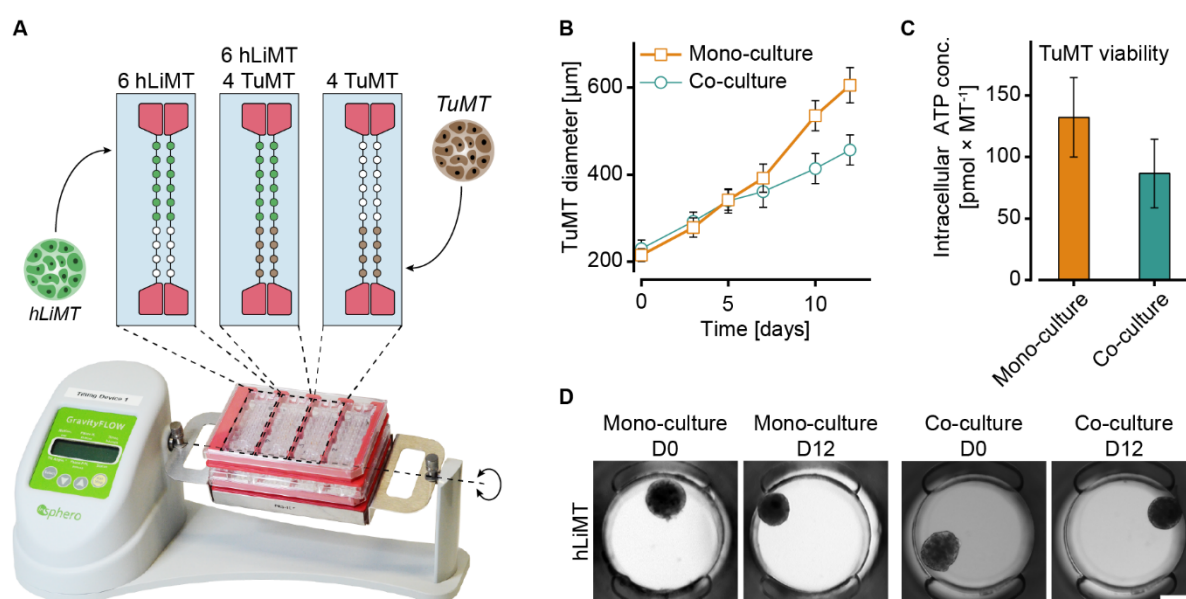


Figure 4: Combination of microtissue (MT) models on microfluidic chip. **(A)** Arrangement of human liver MTs (hLiMTs) and tumor MTs (TuMTs) on microfluidic chips under monoculture and co-culture conditions. Up to four chips can be assembled into plates, which then can be stacked onto automated tilting platforms. **(B)** Growth of TuMTs over twelve days under monoculture or co-culture conditions (data represented as mean \pm SD). **(C)** ATP-dependent viability of TuMTs on day twelve (data represented as mean \pm SD). **(D)** Representative on-chip images of hLiMTs on day 0 and day 12 under monoculture and co-culture conditions (scale bar = 200 μm).

as drug target tissues (Figure 4A). The co-culture characteristics were compared to mono-culture control conditions with six hLiMTs or four TuMTs per microfluidic channel. Under co-culture conditions, TuMT growth was 0.75-fold lower over a time period of 12 days as compared to mono-culture conditions (Figure 4B). Analysis of intracellular ATP concentrations of TuMTs on day 12 supported this observation, as lower ATP concentrations were found in TuMTs co-cultured with hLiMTs. Comparison of bright-field images of hLiMTs on day 0 and day 12 showed no morphological differences between mono-culture and co-culture conditions (Figure 4D).

To further assess the metabolic functionality of hLiMTs and their interaction with TuMTs, we administered two prodrugs, Cyclophosphamide (CP) and Ifosfamide (IFF), to the system. While the two parent compounds themselves have no effect on tumor growth, their hepatic metabolites exhibit cytostatic anticancer activity. Prodrug metabolism by the hLiMTs was assessed by monitoring the growth of TuMTs cultured in the same channel with the hLiMTs. Figure 5 shows and Table 1 summarizes the initial and final TuMT diameters for culturing during 12 days under three different conditions: (i) in mono-culture in static microwells on a 96-well plate, (ii) in mono-culture without hLiMTs in the microfluidic chip, and (iii) in co-culture with hLiMTs in the microfluidic chip (complete growth curves are shown in Suppl. Figure 4). TuMTs were 2.0 – 2.3-fold larger on day 12 than on day 0 under static conditions (Figure 5A), and 2.4 – 2.8-fold larger under perfusion mono-culture conditions (Figure 5B), regardless of the presence of prodrugs. Under perfusion co-culture conditions, the size of control TuMTs without the prodrug increased 2.0-fold over 12 days,

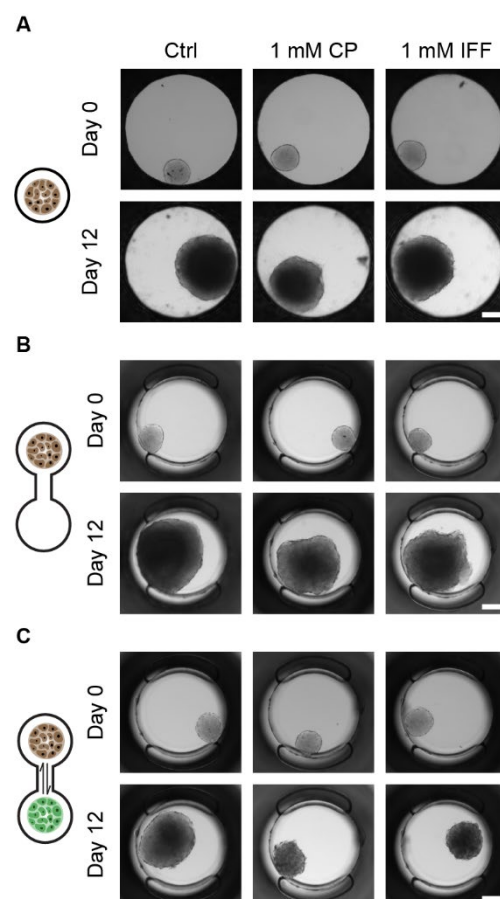


Figure 5: Hepatic bioactivation of Cyclophosphamide (CP) and Ifosfamide (IF). Representative images show tumor microtissues (TuMTs) on day 0 and day 12 under (A) static well-plate conditions, (B) perfusion conditions, and (C) perfusion conditions in combination with human liver microtissues (hLiMTs). Control (ctrl) microtissues were cultivated in plain cell culture medium. Treatment conditions included 1 mM CP or 1 mM IFF during 12 days (scale bars = 200 μ m).

Table 1: TuMT diameters after 12 days of exposure to 1 mM cyclophosphamide (CP) or 1 mM ifosfamide (IFF) under static or perfusion culture conditions and in the absence (monoculture) or presence (co-culture) of hLiMTs (n = 5 – 15 TuMTs; data represented as mean \pm SD).

	Ctrl		CP		IFF	
	Day 0	Day 12	Day 0	Day 12	Day 0	Day 12
Mono-culture Static	240.9 μ m (\pm 8.1)	545.2 μ m (\pm 29.3)	239.5 μ m (\pm 10.6)	518.1 μ m (\pm 40.1)	254.6 μ m (\pm 8.5)	521.2 μ m (\pm 27.8)
Mono-culture Perfused	215.0 μ m (\pm 14.7)	605.5 μ m (\pm 40.8)	212.1 μ m (\pm 27.0)	521.3 μ m (\pm 63.2)	196.2 μ m (\pm 17.2)	478.6 μ m (\pm 56.8)
Co-Culture Perfused	230.0 μ m (\pm 20.1)	456.2 μ m (\pm 35.3)	219.4 μ m (\pm 18.5)	246.9 μ m (\pm 22.7)	223.9 μ m (\pm 17.0)	276.1 μ m (\pm 14.4)

while the presence of 1 mM CP or IFF reduced the growth to 1.1-fold or 1.2-fold, respectively (Figure 5C). The reduced TuMT growth, caused by enzymatic bioactivation of the two compounds through CYP3A4 and CYP2B6 activity, demonstrated the metabolic functionality of the hLiMTs in the presence of TuMTs in the same microfluidic channel. The experiments confirmed that tumor growth can be used as a reliable indicator for treatment efficacy in our testing system.

3.4.4 In vitro prediction of drug-drug interactions

To test the system for its capacity to detect and predict potential drug-drug interactions, we combined each of the two anticancer prodrugs, CP and IFF, with the antiretroviral drug Ritonavir (RTV). hLiMTs and TuMTs in the microfluidic chip were subjected to 1 μ M RTV, 1 mM CP and 1 mM IFF as single compounds, and to combinations of CP + RTV and IFF + RTV at the same concentrations (Figure 6A).

Again, TuMT growth, their final size, and their ATP-dependent viability on day 12 of the experiment provided meaningful readouts to estimate the treatment efficacy (Figure 6). Analysis of the raw data from the chip cultivation channel and the culture plate of MTs showed similar variability in MT size between TuMTs, cultured within the same channel or in different channels under the same treatment conditions (Suppl. Figure 5). Therefore, all MTs cultured under the same treatment condition were pooled into one sample group.

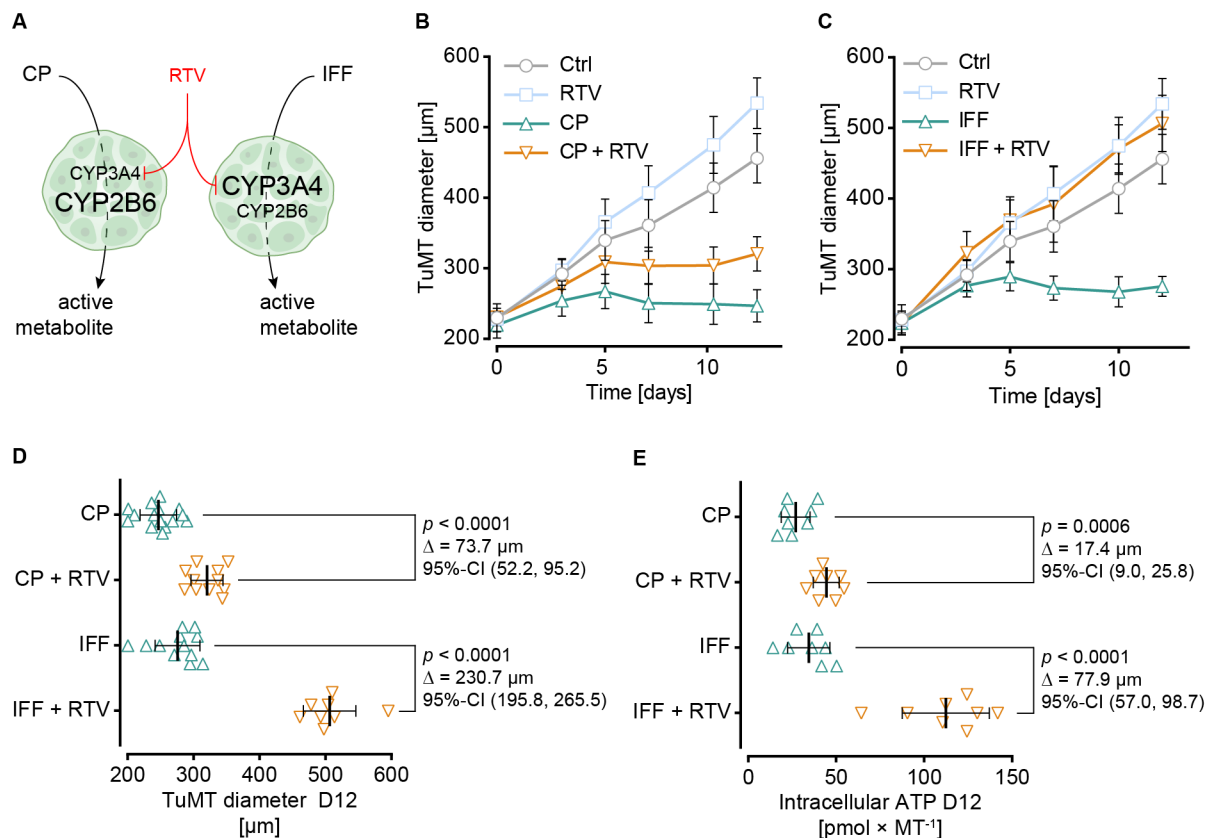


Figure 6: Detection of drug-drug-interaction in a tumor-liver co-culture system. **(A)** Metabolic activation pathway of Cyclophosphamide (CP) and Ifosfamide (IFF) through CYP3A4 and CYP2B6 in the liver. Ritonavir (RTV) is a potent CYP3A4 inhibitor. **(B)** Growth of tumor microtissues (TuMTs) over twelve days under exposure to Cyclophosphamide (CP) ± Ritonavir (RTV), or **(C)** Ifosfamide (IFF) ± RTV. **(D)** Comparison and analysis of diameter, and **(E)** intracellular ATP of TuMTs treated for 12 days with single prodrugs and a prodrug/RTV combination ($n = 7 - 15$ TuMTs; all data represented as mean \pm SD; statistical analysis by t-tests ($\alpha = 0.05$), followed by a calculation of the raw effect sizes, Δ , and their 95% confidence intervals).

RTV alone did not substantially influence TuMT growth as compared to the untreated control MTs. TuMTs under both conditions constantly grew over the experimental culture period of 12 days. CP treatment successfully stopped tumor growth in the system (Figure 6B). Concomitant administration of RTV still yielded a drastically reduced growth of TuMTs in comparison to untreated control conditions. However, the impact on TuMT growth was not as high as upon treatment with CP only. Treatment with IFF resulted in growth inhibition of TuMT, similar to the one observed when treated with CP (Figure 6C). In contrast to CP, however, a combination of IFF and RTV reduced the anticancer effect of IFF and led to a growth curve similar to that of untreated control TuMTs. The same trend of responses to the different treatment conditions was seen in ATP-dependent viability measurements on day 12 of the experiment (Suppl. Figure 6A). ATP measurements of hLiMTs on day 12 revealed similar concentrations under all

conditions, indicating that none of the drug treatments had an impact on hLiMT viability (Suppl. Figure 6B). Mono-culture control TuMTs in microwell plates or in the microfluidic chip in the absence of hLiMTs did not respond to treatment with any of the compounds or their combinations (Suppl. Figure 7).

The change in prodrug efficacy upon co-administration with RTV was statistically analyzed using a t-test and a calculation of the raw effect sizes, Δ . Each prodrug MT group was individually compared to its respective drug-combination MT group. Treatment with CP and IFF as single drugs resulted in significantly smaller TuMTs on D12 than in combination with RTV ($p < 0.0001$; Figure 4D). Differences between CP and CP+RTV treatment ($\Delta = 73.7 \mu\text{m}$; 95%-CI (52.2, 95.2)) were, however, much smaller than between IFF and IFF+RTV treatment ($\Delta = 230.7 \mu\text{m}$; 95%-CI (195.8, 265.5)). Comparison of ATP-dependent viability values on day 12 yielded similar results: prodrug-treated TuMTs were significantly smaller than the TuMTs treated with the respective drug combinations. Again, the differences between IFF-treated and IFF+RTV-treated TuMTs were larger than the ones between CP-treated and CP+RTV-treated

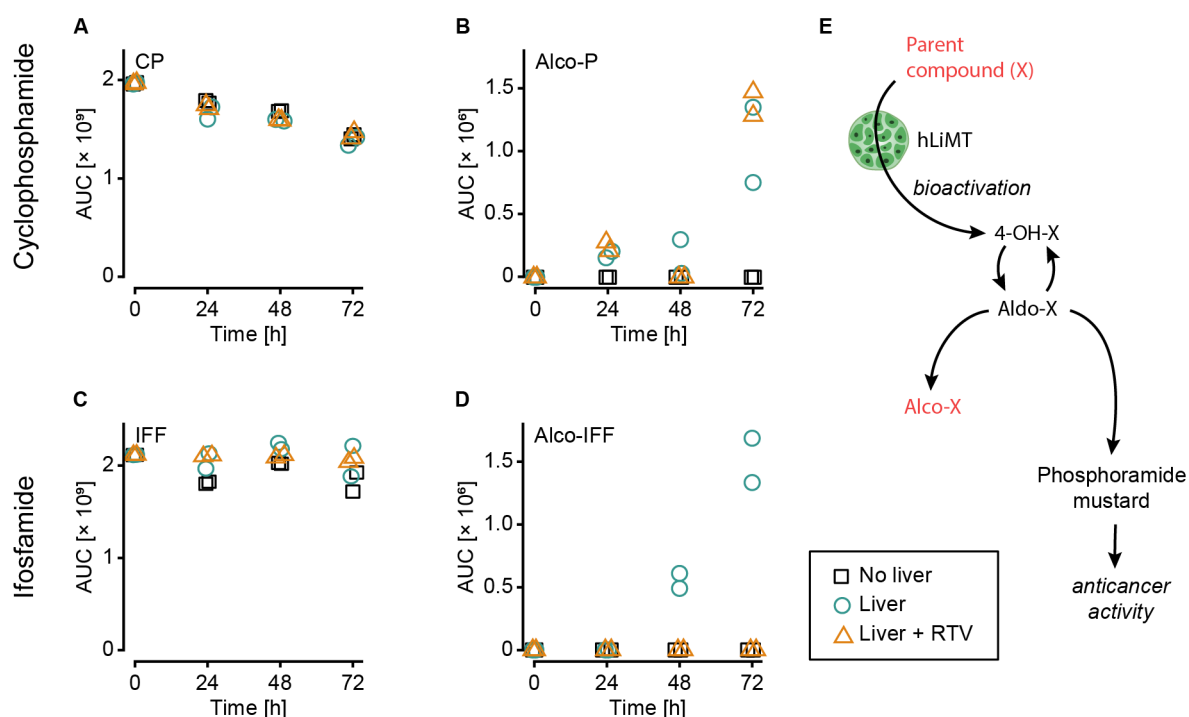


Figure 7: Quantification of the parent compounds by mass spectrometry (A) Cyclophosphamide (CP) and (C) Ifosfamide (IFF), as well as their hepatic metabolites (B) Alcohosphamide (Alco-P) and (D) Alco-ifosfamide (Alco-IFF) by mass spectrometry. Substance concentrations were monitored over 72 h in the presence or absence of human liver microtissues and Ritonavir (RTV). (E) Activation pathway of CP and IFF with the detected substances indicated in red.

MTs ($p = 0.0006$, $\Delta = 17.4 \text{ pmol} \times \text{MT}^{-1}$; 95%-CI (9.0, 25.8) for CP conditions and $p < 0.0001$, $\Delta = 77.9 \text{ pmol} \times \text{MT}^{-1}$; 90%-CI (57.0, 98.7) for IFF conditions).

To confirm the differential drug-drug interactions of RTV with CP and IFF in our testing platform, we exposed hLiMTs to CP or IFF, with and without RTV, and analyzed their metabolic footprint over 72 h. We chose 72 h, since this was the maximum time interval before the cell-culture medium is routinely changed during an experiment. Figure 7A – D shows the measured relative concentrations of the parent compounds and one of their metabolites for incubation under three different conditions: (i) in the absence of hLiMTs, (ii) in the presence of a hLiMT, and (iii) in the presence of a hLiMT and RTV. The metabolic pathways of CP and IFF and some of their most important metabolites are depicted in Figure 7E. The concentrations of both parent compounds were not affected by the presence of hLiMTs or RTV. While the CP concentration slightly decreased over time, no differences between the three treatment conditions were observed (Figure 7A). The concentration of IFF remained constant over 72 h (Figure 7C). For both prodrugs, the two analogous metabolites Alcophosphamide (Alco-P) and Alcoifosfamide (Alco-IFF) could be identified. In the activation pathway of CP and IFF, Alco-metabolites appear after the biotransformation step through liver-resident CYP-enzymes and are, therefore, an indicator of successful hepatic bioactivation.³⁸ Alco-P was first detected after 24 h and was further enriched if hLiMTs or hLiMTs and RTV were present. Without hLiMTs, no Alco-P could be detected (Figure 7B). Alco-IFF was first detected after 48 h in the presence of hLiMTs. However, as soon as RTV was dosed, Alco-IFF generation in the hLiMTs decreased to an undetectably low amount (Figure 7D). Other identified metabolites included Carboxycyclophosphamide (CO-CP), Dechloroethylcyclophosphamide (DC-CP), 2-dechloroethylifosfamide (2-DC-IFF), and 3-dechloroethylifosfamide (3-DC-IFF; see Suppl. Figure 8). Metabolites originating from CP were generated in similar amounts under both conditions including the presence of hLiMTs, and the respective concentrations were not affected by the dosage of RTV. IFF metabolites, on the other hand, were produced in lower amounts upon dosage of RTV as compared to conditions without RTV.

3.5 Discussion

We aimed to develop a human-tissue-based *in vitro* testing system for the prediction of metabolism-induced interactions of pharmacologically active substances (DDIs). As DDIs can occur on one organ, such as the metabolizing organ (e.g., liver), and then affect other organs

that are targeted by the drug tissues, a suitable in-vitro system needs to include several tissue types and ensure their interaction and crosstalk. Moreover, the in-vitro system should not only enable to selectively and specifically identify DDIs but also to quantify the respective effects. For the establishment of a reliable working platform, we here used drugs that undergo metabolic conversion in the liver (prodrugs CP and IFF) to become active on their target tissue, which was a tumor. Moreover, we used an antiretroviral drug (RTV), which affected metabolic processes in the liver.

3.5.1 Metabolic competence of the liver in the testing system

Characterization of hLiMTs in microwell plates under static conditions and in the perfused system evidenced similar functionality and viability for both culture conditions, which renders hLiMTs suitable for our testing system. Intracellular ATP concentrations remained stable (Figure 2A), whereas albumin secretion slightly decreased proportionally to hLiMT size over 14 days under both culture conditions (Figure 2B and Suppl. Figure 1). In contrast, the metabolic capacity of hLiMTs was found to be stable over the experimental period, which is important for our test system. The decreasing CYP2B6 activity of primary hepatocytes in culture is a common behavior that has been previously described.³⁹ Nevertheless, the CYP isoform maintained the potential to be pharmacologically induced with compounds, such as phenobarbital or CP.^{39, 40} Some CYP isoforms even increased their activity under perfusion conditions (Figure 2C and D, and Suppl. Figure 2). The obtained results suggest that the viable liver cell mass sufficed as metabolizing unit in the testing system, which was confirmed through the fact that hLiMTs were able to successfully generate cytostatic metabolites of CP and IFF that then suppressed TuMT growth over an experimental period of 12 days (Figures 5 and 6). The possibility to modulate the metabolic activity of hLiMTs was shown through inhibition of CYP3A4 activity by dosage of RTV and KCZ (Figure 2E, and Suppl. Figure 3). Both drugs led to an almost complete inhibition of CYP3A4 activity. The dynamics of CYP3A4 activity in the system were demonstrated through the activity increase upon dosage of CP and IFF (Suppl. Figure 5B).

3.5.2 Tumor as drug target tissue and multi-tissue configuration

TuMTs were used to investigate DDIs, and their growth was used as functional readout for drug treatment efficacy. Comparison of TuMTs, cultured under static and perfusion conditions, revealed different growth behavior for the two conditions. We attributed the different growth characteristics to differences in nutrient availability: (i) nutrient diffusion and distribution to the culturing compartment and (ii) maximally available medium volume and nutrients per MT. Both factors will be briefly explained.

- (i) Under static culturing conditions in a microwell plate, the nutrient availability is limited through diffusion along a concentration gradient with the lowest concentration at the location of the MT, where nutrients are consumed. Depending on the MT size, the consumption rate may become larger than the diffusion rate of nutrients to the MT location, which then limits MT growth. In contrast, active perfusion through the channels constantly provides nutrients to the MTs in the culturing chip through agitated flow. The result is a lower growth rate of TuMTs under static conditions in both cell-culture medium types (Figure 3A and B).
- (ii) The volume ratio of medium and MT and, hence, of nutrients and MT is largest in microwell plates (70 μL per MT). This ratio decreases with an increasing number of MTs per culture channel (37.5 μL per MT for four MTs per channel and 15 μL per MT for ten MTs per channel). The lower the medium volume per MT, the more likely is a nutrient depletion of the medium between two subsequent medium exchanges. This effect explains the lower growth rate of having ten MTs in a channel as compared to four MTs per channel.

The influence of both factors became visible after 7 days of culturing and showed a dependence on MT size. The growth rate of smaller MTs (diameter less than approx. 450 μm) was not limited by diffusive transport in microwells and was independent of the number of MTs in the microfluidic channels, as there were sufficient nutrients under all circumstances. Between days 7 and 14 of TuMT culturing, a MT diameter larger than approx. 450 μm was reached, so that the growth curves began to diverge (see, e.g., Figure 3), as a larger cell mass required more nutrients.

In terms of microtissue configurations, the growth dynamics using an arrangement of ten MTs in one channel of the microfluidic chip (15 μ L medium per MT) were still large enough to provide a reliable readout of anticancer-drug efficacy. This finding was confirmed by the chemotherapeutic drug treatment of TuMTs in co-culture with hLiMTs, as the effects of CP and IFF on TuMTs became clearly visible by monitoring the TuMT diameters (Figure 5). Since growth inhibition did not occur without hLiMTs, we assumed that the effect of CP and IFF on tumor growth was caused by metabolites that were generated by the hLiMTs.

Another frequently encountered challenge in setting up a multi-tissue *in vitro* system is to find a common cell-culture medium that is suitable to maintain the specific functions of all included tissues.⁴¹ For the combination of TuMTs with hLiMTs, we tested the human liver maintenance medium for its suitability to maintain and grow TuMTs. The liver maintenance medium was chosen instead of the standard RPMI-based TuMT-culture medium due to its defined, serum-free formulation and due to the higher sensitivity of hLiMTs to changes in medium composition. Similar growth characteristics of TuMTs, cultured in the two different cell culture media, demonstrate the suitability of hLiMM-TOX as a common cell-culture medium.

3.5.3 Identification of DDIs between IFF and RTV

The identification of DDIs was tested by administering two anticancer prodrugs. We selected CP and IFF, which are structurally very similar and feature similar activation pathways and mode of actions. However, the CYP isoforms that catalyze the bioactivation of the two prodrugs are significantly different. While CP is mainly metabolized by CYP2B6 and, to a lower extent, by CYP3A4 (Figure 6A), the bioactivation of IFF relies mostly on CYP3A4.⁴² To test for DDIs in our system, the two prodrugs were administered in combination with a known CYP3A4 inhibitor. Initially, we tested KCZ and RTV for their suitability. Due to the negative impact of higher concentrations of KCZ on hLiMT health (Suppl Figure 2), we selected RTV as CYP3A4 inhibitor for all DDI experiments. Based on previous experiments we used CP and IFF concentrations of 1 mM.²⁵ Maximum blood-plasma concentrations in patients, depending on the administration route and dosing regimen, were reported to range between 80 and 157 μ M for CP⁴³⁻⁴⁵ and between 75 and 350 μ M for IFF.⁴⁶⁻⁴⁸ RTV successfully inhibited CYP3A4 at concentrations of 1 μ M, while reported blood plasma concentrations in HIV patients were between 10 and 22 μ M.⁴⁹ Compared to the *in vivo* situation, our testing system required 10-fold higher prodrug concentrations but a comparably low RTV concentration to obtain full CYP3A4 inhibition. These observations can be explained by the lower metabolic capacity of the *in vitro*

system in comparison to the *in vivo* situation. Still, our device was able to capture effects at drug doses closer to the physiologically relevant concentration range in comparison to other *in vitro* microfluidic liver-tumor systems that detected effects at CP doses of 2.7 – 10 mM.^{50, 51}

Successful anticancer drug treatment in our system was evidenced by inhibition of TuMT growth but not by shrinkage of TuMTs. This observation is in line with the reported cytostatic activity of CP and IFF. Such alkylating agents are known to crosslink DNA strands, leading to apoptosis of cells that undergo cell division.⁵² The quiescent cell population, however, can cope with the induced damage and survive.⁵³ Tracking the growth behavior of the TuMTs showed a loss of IFF anticancer activity when co-administered with RTV, which indicates DDIs between the two drugs. CP treatment, on the other hand, was much less impacted upon co-administration with RTV (Figure 6). The different effects of RTV co-dosage on TuMT growth were related to the role of CYP3A4 in the bioactivation of the two prodrugs: According to a study conducted by Huang, Roy⁴², who quantified the involvement of different CYP isoenzymes in the bioactivation of the two prodrugs, CYP3A4 accounts for 24.7% of CP activation and for 64.8% of IFF activation.

ATP measurements of TuMTs treated under these four conditions showed results similar to those of the size measurements, however with significantly larger variability between individual MTs. This variability can be explained by the existence of necrotic cores in large MTs with diameters of approx. 500 μm ,⁵⁴ the volume of which may largely vary. In a proliferating microtissue, the necrotic core grows proportionally to the overall microtissue size.⁵⁵ Necrotic cores contribute to the size of the TuMTs, however, do not contribute to the measured ATP content. In large MTs, cell proliferation or pharmacological inhibition may, therefore, be better represented by MT size measurements than ATP measurements. In this study, we thus prevalingly used the size or diameter of TuMTs as readout for DDI predictions.

More detailed analysis of the hepatic prodrug metabolization by mass spectrometry showed the generation of CP and IFF metabolites, which can be assigned to two categories: (i) metabolites of the drug-activation pathway (Alco-P, CO-P, and Alco-IFF), and (ii) metabolites of the drug-deactivation pathway (DC-P, 2-DC-IFF, and 3-DC-IFF).

Metabolites of the (i) activation pathway were detected in samples without RTV (Figure 7 and Suppl. Figure 8). These metabolites do not feature anticancer activity. Their detection, however, suggests a metabolization pathway via the Aldo-metabolite (Aldo-X). While Aldo-X are the

precursors of CO-P and Alco-X, they can also generate phosphoramidate/ifosforamidate mustard by β -elimination of acrolein (Figure 7E).³⁸ Phosphoramidate and ifosforamidate mustard, which exhibit anticancer activity, are very short-lived and were, therefore, not detected by MS analysis. However, the detection of Alco-metabolites and the inhibition of TuMT growth in the co-culture experiments provide strong evidence of the presence and activity of the two equivalent mustard agents. Co-administration of RTV decreased the metabolites of IFF to undetectably low concentrations, while CP-metabolites were still generated. These results confirmed DDIs of RTV with the two prodrugs mediated by CYP3A4, which had been observed in TuMT size measurements.

The deactivation pathway (ii) and its metabolites do not contribute to anticancer activity (Suppl. Figure 8A). In contrast, the involved metabolites are known to be neurotoxic and nephrotoxic and a major contributor to reported side effects of the drugs.^{56, 57} Interestingly, the deactivation pathways were unaffected by RTV exposure, which confirms the active role of other CYP-isoforms, such as CYP2B6.⁵⁶ The presence of 2-DC-IFF and 3-DC-IFF in IFF+RTV-treated samples indicated that the co-administration of IFF and RTV may lead to the conversion of a major fraction of the dosed IFF to neuro-/nephrotoxic metabolites. Co-administration of IFF and RTV may not only lead to inefficiency of the anticancer treatment but may also cause severe side effects for the patients.

The MS analysis further showed that metabolite concentrations exponentially increased during the 72 h incubation time with hLiMTs. The initial growth of CP- and IFF-treated TuMTs within the first 3 to 5 days can, thereby, be explained by the time that is needed to reach a certain threshold concentration of anti-cancer prodrug metabolites to affect TuMT growth. This delayed anti-cancer effect, however, can only be seen in the initial period of the 12-day experiment, since CP and IFF induce CYP expression.^{58, 59} This induction of CYP3A4 activity could be measured in our co-culture system: the enzymatic activity of CYP3A4 in hLiMTs after 12 days of treatment with CP or IFF was 4-fold higher as compared to untreated hLiMTs (Suppl. Figure 6B). Once induced, CYP-enzyme-mediated conversion was more efficient, and the production of toxic metabolites was faster than during the initial days, which resulted in maintenance of the required threshold concentration for anticancer activity, even upon medium exchanges.

3.5.4 Potential of the testing system

In our proof-of-concept experiments, we showed the combination and interaction of hLiMTs with TuMTs in our microfluidic platform. While this combination was relevant for the selected DDIs between anticancer and antiretroviral drugs, other organs may come into play for other DDIs. Examples of drug combinations and details of their interactions have been reported in literature.^{60, 61}

In vitro systems show promise for detecting DDIs, which provides important information for the drug development process. DDIs could be previously identified in single-organ systems.⁶²⁻⁶⁴ Perfused co-cultures of primary human hepatocytes and Kupffer cells were used to assess liver inflammation in response to specific drug combinations.⁶² Moreover, a perfused, cell line-based co-culture of hepatocytes with non-parenchymal cells was used to detect hepatotoxic effects of drug mixtures after 24 h of treatment.⁶⁴ All these systems used the metabolization capacity of the liver. Another *in vitro* system for the identification of DDIs included cardiomyocytes on microelectrode arrays to assess the effects of a drug combination on their beating frequency.⁶³ In all cases, the effects of drug combinations on a single-organ were investigated without taking into account hepatic metabolization of drugs or potential effects on other organs.

Combinations of two or more organs in microfluidic systems were proposed to assess drug safety and efficacy. A liver-heart combination was used to detect metabolism-related efficacy and off-target toxicity of anticancer drugs.⁶⁵ However, only effects of single drugs on one or several organs were shown. Moreover, many microfluidic systems are custom-designed for specific organs and organ combinations so that their applicability is limited.

The system presented here offers the opportunity to set up customized experiments with an organ selection that is relevant for the drug combination of interest. Owing to the generic design of the microfluidic chip and the availability of a variety of transferrable 3D organ models (spheroidal microtissues),⁴¹ a testing platform with different organ combinations can be configured. The system could even be utilized to personalize combinatorial drug treatments according to a patient's metabolic constitution if the relevant patient cells would be available. The selection of readouts may encompass comparably basic methods, e.g., bright-field imaging and size measurements, or more sophisticated analyses of, e.g., supernatants, or the use of omics-methods on the MT itself. The developed methodology constitutes a scalable approach

to assess and quantify potential DDIs using an all-human system, and we are confident that the system can be used to study a large spectrum of DDIs.

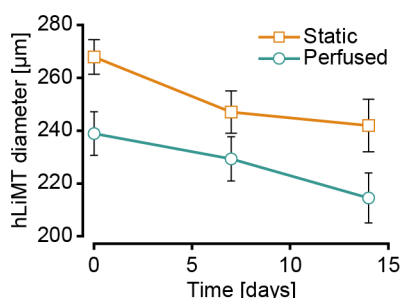
3.6 Conclusion

We established an *in vitro* testing system, consisting of metabolically active hLiMTs and TuMTs as drug target tissues in a microfluidic chip, which can be used to specifically assess and predict metabolism-related drug-drug interactions. Our proof-of-principle experiments show that the presented system can detect altered drug efficacies of CP and IFF when co-administered with RTV. Further, size measurements of TuMTs proved to be a straightforward readout to assess the severity of the respective DDIs. The flexible MT compartment design, the use of polystyrene as chip material, and the assembly of several chips in stackable plates render the system a promising tool to test a broad variety of drug combinations with the aim to identify possible DDIs during drug development.

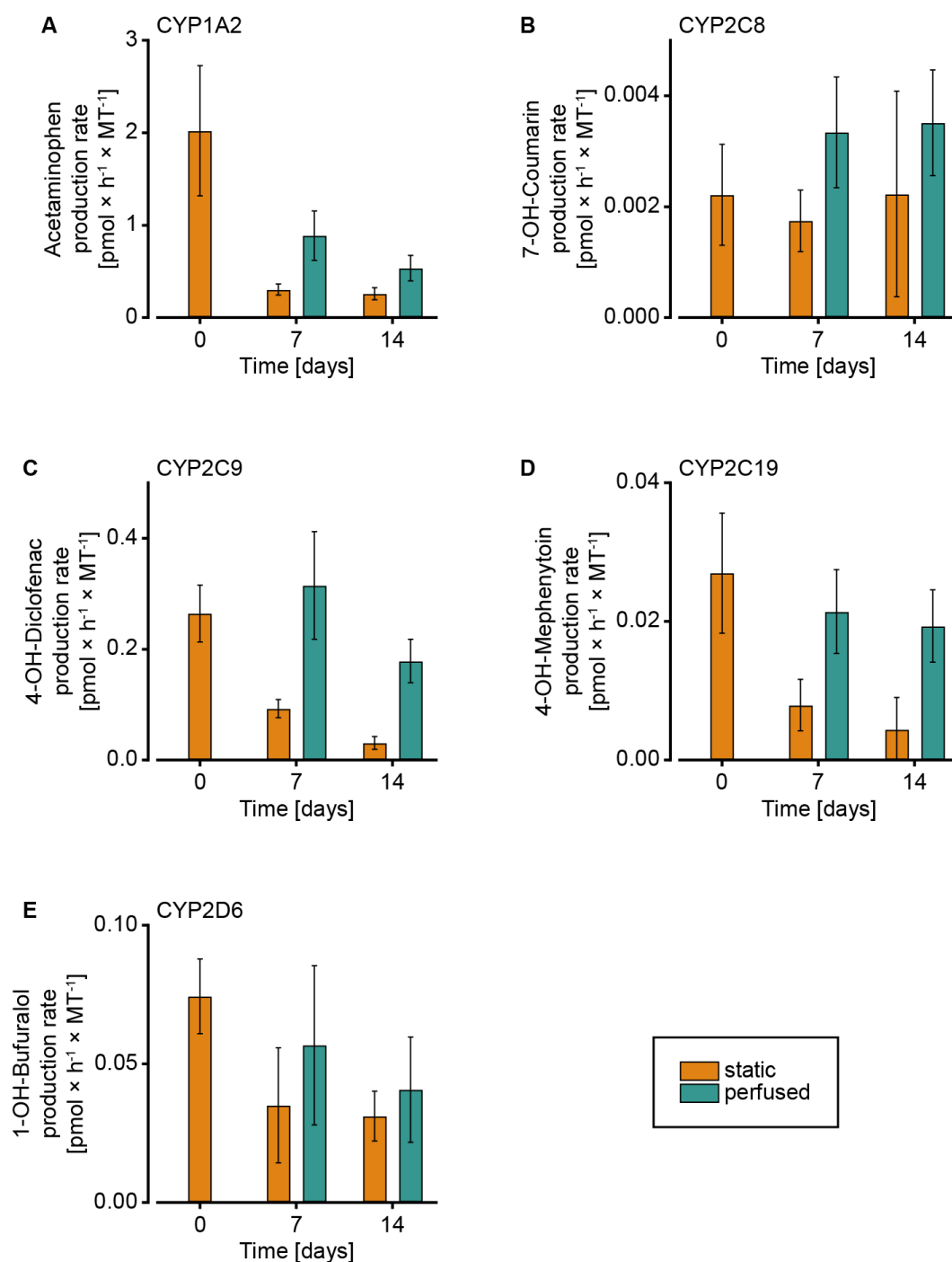
3.7 Acknowledgements

The work was financially supported by the Swiss CTI grant 18024.1 PFLS-LS. We thank Fabrizio Hürlimann (InSphero AG, Schlieren, Switzerland) for data on human liver microtissue characterization. Further, we thank Dr. Hans-Michael Kaltenbach (ETH Zurich, D-BSSE, Basel, Switzerland) for his support regarding statistical analyses of results, and Dr. Mario M. Modena (ETH Zurich, D-BSSE) for his advice for conceptualization of this manuscript.

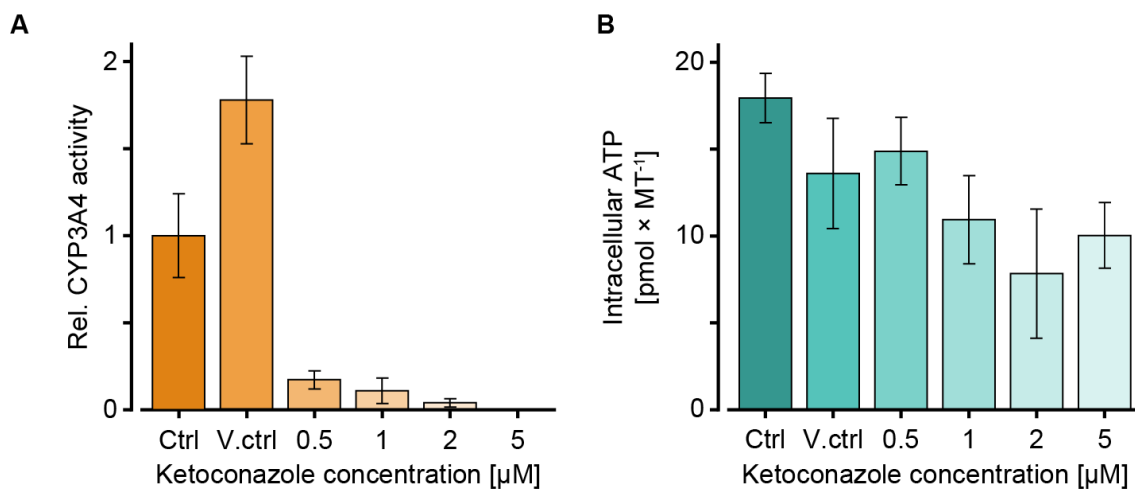
3.8 Supporting Information



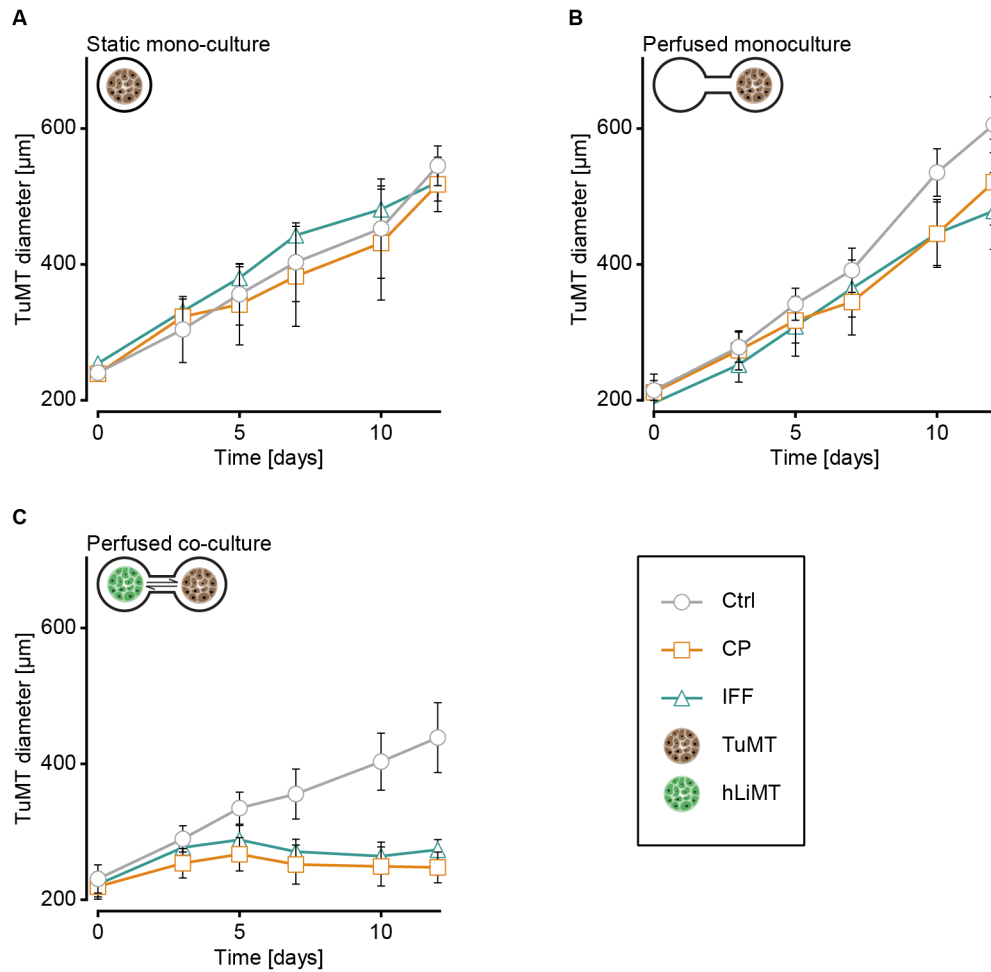
Supplementary Figure 1: Human liver microtissue (hLiMT) diameter over time under static culturing conditions in a microwell plate and under perfusion conditions in the microfluidic chip ($n = 16 - 30$ hLiMTs; data represented as mean \pm SD).



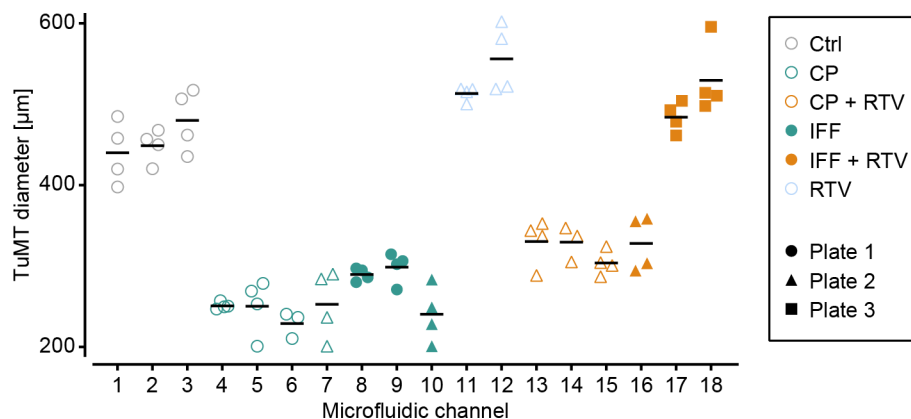
Supplementary Figure 2: Metabolic cytochrome P540 (CYP) activity of human liver microtissues (hLiMTs) under static and perfusion conditions over 14 days. CYP isoform-specific activity has been measured by conversion of (A) Phenacetin to Acetaminophen for CYP1A2, (B) Coumarin to 7-OH-Coumarin for CYP2C8, (C) Diclofenac to 4-OH-Diclofenac for CYP2C9, (D) Mephenytoin to 4-OH-Mephenytoin for CYP2C19, and (E) Bufuralol to 1-OH-Bufuralol for CYP2D6. For measurements, hLiMTs were incubated with a cocktail of these substances for 24 h. The CYP isoform-specific metabolites were quantified by liquid chromatography-mass spectrometry (n = 3 – 6 hLiMTs; data represented as mean ± SD).



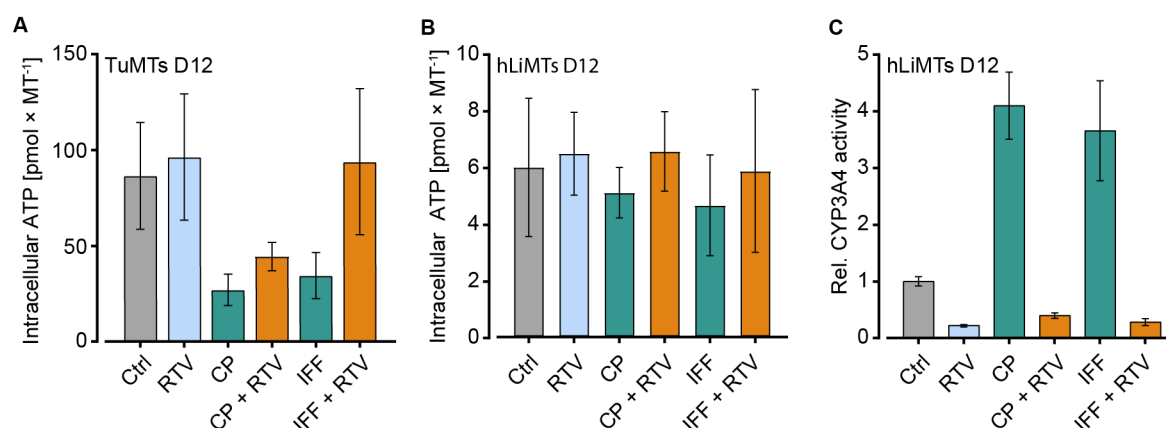
Supplementary Figure 3: Inhibition of the enzymatic activity of cytochrome P450 3A4 (CYP3A4) with the antifungal substance ketoconazole (KCZ). **(A)** Measurement of the relative CYP3A4 activity after three days of exposure to different doses of KCZ under static microtiter plate conditions. CYP3A4 activity was measured using the P5450-GloTM CYP3A4 assay (Promega, Dübendorf, Switzerland) with Luciferin-IPA as substrate. **(B)** The ATP-dependent viability was measured for the same microtissues using the CellTiter-Glo® 3D Cell Viability assay (Promega; n = 3 – 4 hLiMTs; data represented as mean ± SD).



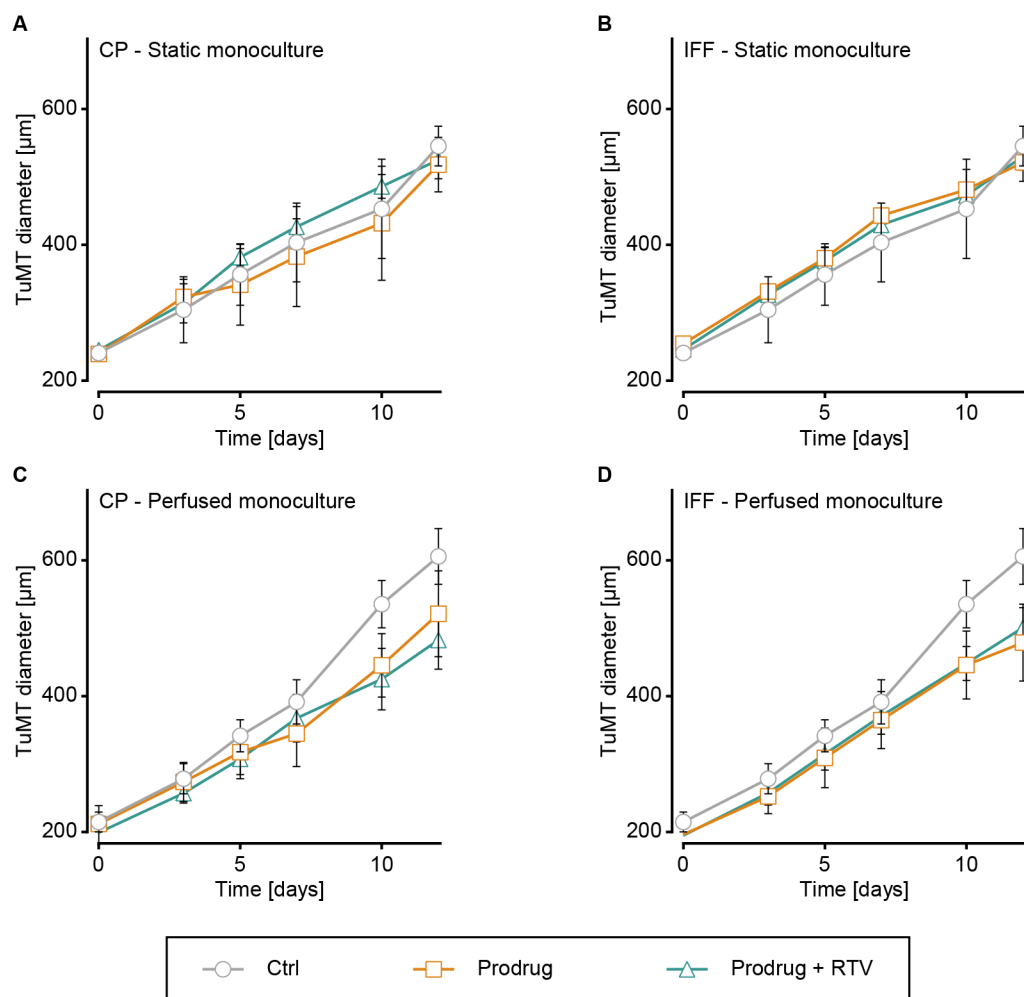
Supplementary Figure 4: Growth of tumor microtissues (TuMTs) during 12 days under exposure to 1 mM cyclophosphamide (CP) or 1 mM ifosfamide (IFF). TuMTs were cultured under (A) static mono-culture conditions with individual TuMTs in the wells of a microtiter plate, (B) perfusion mono-culture conditions with 4 TuMTs in a microfluidic channel, or (C) perfusion co-culture conditions with 6 human liver microtissues (hLiMTs) and 4 TuMTs in a microfluidic channel. TuMT diameter was measured on microscopic images taken on the respective days ($n = 5 - 15$ TuMTs, data represented as mean \pm SD).



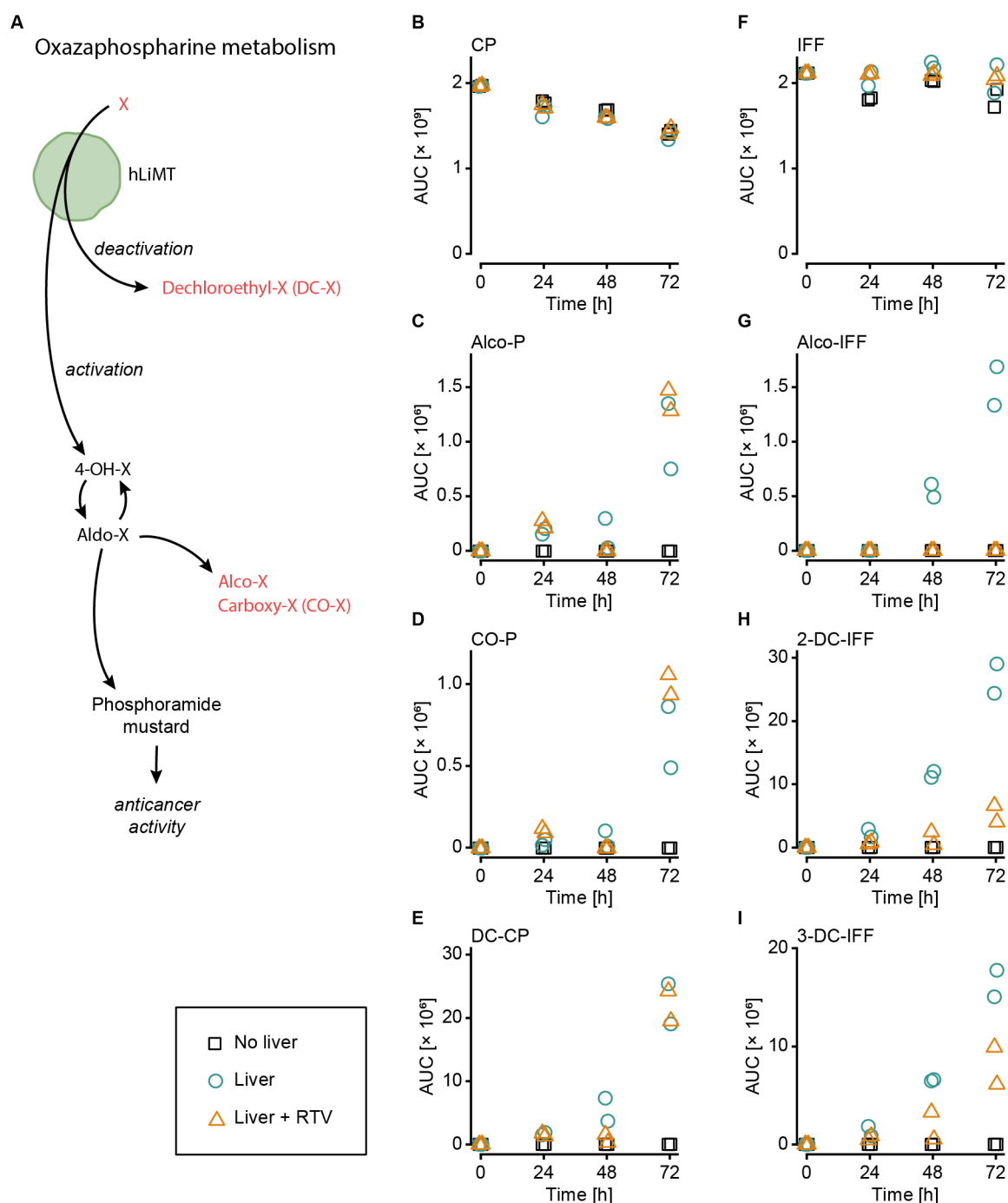
Supplementary Figure 5: Representation of the raw data of TuMT diameters after 12 days of exposure to 1 mM Cyclophosphamide (CP), 1 mM Ifosfamide (IFF), or combinations of these drugs with 1 μ M Ritonavir (RTV) under perfusion co-culture conditions with human liver microtissues (hLiMTs). TuMTs were arranged according to their microfluidic culture channel (X-axis), and the culture plate, on which four microfluidic chips were mounted (shape of data points). Channel-to-channel differences and plate-to-plate differences within one treatment group were smaller than within-channel differences. Therefore, all MTs cultured under the same treatment condition were pooled into one sample group. The diameters of TuMTs under treatment with IFF + RTV in the microfluidic channel 16 substantially differed from those of the other MTs within the same treatment group and reached a size similar to the one of the CP + RTV group. Given their position on the culture plate in proximity to the channel subjected to CP + RTV treatment, this result is due to a pipetting error and false treatment for channel 16. We, therefore, excluded channel 16 from the statistical analysis of the results.



Supplementary Figure 6: Additional readouts of the drug-drug interaction experiment. Four tumor microtissues (TuMTs) were co-cultured with six human liver microtissues (hLiMTs) in microfluidic chips. Measurements were performed after 12 days of exposure to 1 mM Cyclophosphamide (CP), 1 mM Ifosfamide (IFF), or a combination of one of the drugs with 1 μM Ritonavir (RTV). ATP-dependent viability of **(A)** TuMTs and **(B)** hLiMTs was assessed using the CellTiter-Glo® 3D cell viability assay (Promega; $n = 5 - 15$ TuMTs; data represented as mean \pm SD). **(C)** CYP3A4 activity of hLiMTs was measured using the P450-Glo™ CYP3A4 assay (Promega) with Luciferin-IPA as substrate ($n = 12 - 16$ hLiMTs; data represented as mean \pm SD).



Supplementary Figure 7: Growth of tumor microtissues (TuMTs) during 12 days under exposure to 1 mM Cyclophosphamide (CP), 1 mM Ifosfamide (IFF), or combinations of these drugs with 1 μ M Ritonavir (RTV). TuMTs were cultured under **(A, B)** static mono-culture conditions with individual TuMTs in the wells of a microtiter plate, or **(C, D)** perfusion mono-culture conditions with 4 TuMTs interconnected in a microfluidic channel ($n = 7 - 15$ TuMTs, data represented as mean \pm SD).



Supplementary Figure 8: Metabolic footprint upon hepatic metabolism of the prodrugs Cyclophosphamide (CP) and Ifosfamide (IFF) in the presence or absence of the cytochrome P450 3A4 inhibitor Ritonavir (RTV). **(A)** General activation pathway of oxazaphosphorine drugs, such as CP and IFF, by the liver. Detected metabolites are indicated in red. Upon metabolism of **(B)** CP, its metabolites **(C)** Alco-CP, **(D)** Carboxy-CP (CO-CP), and **(E)** Dechloroethyl-CP (DC-CP) were detected. Upon metabolism of **(F)** IFF, its metabolites **(G)** Alco-IFF, **(H)** 2-Dechloroethyl-IFF (2-DC-IFF), and **(I)** 3-Dechloroethyl-IFF (3-DC-IFF) were detected. hLiMTs were exposed to the drugs during 72 h in a static microtiter plate. Samples were taken from individual wells for each time point. Compounds and their metabolites were

semiquantitatively analyzed using ultra-performance liquid chromatography – mass spectrometry.

3.9 References

1. Juurlink, D.N., et al., Drug-drug interactions among elderly patients hospitalized for drug toxicity. *JAMA*, **289**, 1652-1658 (2003).
2. Muirhead, G.J., et al., Pharmacokinetic interactions between sildenafil and saquinavir/ritonavir. *Br J Clin Pharmacol*, **50**, 99-107 (2000).
3. Bordet, R., et al., Analysis of the direct cost of adverse drug reactions in hospitalised patients. *European journal of clinical pharmacology*, **56**, 935-941 (2001).
4. Gareri, P., et al., Venlafaxine-propafenone interaction resulting in hallucinations and psychomotor agitation. *The Annals of pharmacotherapy*, **42**, 434-438 (2008).
5. Gilard, M., et al., Influence of omeprazole on the antiplatelet action of clopidogrel associated with aspirin: the randomized, double-blind OCLA (Omeprazole CLopidogrel Aspirin) study. *Journal of the American College of Cardiology*, **51**, 256-260 (2008).
6. Backman, J.T., et al., The area under the plasma concentration-time curve for oral midazolam is 400-fold larger during treatment with itraconazole than with rifampicin. *European journal of clinical pharmacology*, **54**, 53-58 (1998).
7. Volpe, D.A. and P.V. Balimane, Application of in vitro CYP and transporter assays to predict clinical drug-drug interactions. *Bioanalysis*, **10**, 619-623 (2018).
8. Rautio, J., et al., The expanding role of prodrugs in contemporary drug design and development. *Nature reviews. Drug discovery*, **17**, 559-587 (2018).
9. Tirkkonen, T. and K. Laine, Drug interactions with the potential to prevent prodrug activation as a common source of irrational prescribing in hospital inpatients. *Clinical pharmacology and therapeutics*, **76**, 639-647 (2004).
10. Kumar, S., R. Sharma, and A. Roychowdhury, Modulation of cytochrome-P450 inhibition (CYP) in drug discovery: a medicinal chemistry perspective. *Current medicinal chemistry*, **19**, 3605-3621 (2012).
11. Bale, S.S., et al., Emerging In Vitro Liver Technologies for Drug Metabolism and Inter-Organ Interactions. *Tissue Eng Part B Rev*, **22**, 383-394 (2016).
12. Giang, I., E.L. Boland, and G.M. Poon, Prodrug applications for targeted cancer therapy. *AAPS J*, **16**, 899-913 (2014).
13. Zhang, X., et al., Prodrug strategy for cancer cell-specific targeting: A recent overview. *European journal of medicinal chemistry*, **139**, 542-563 (2017).
14. Beijnen, J.H. and J.H. Schellens, Drug interactions in oncology. *Lancet Oncol*, **5**, 489-496 (2004).

15. Al-Lazikani, B., U. Banerji, and P. Workman, Combinatorial drug therapy for cancer in the post-genomic era. *Nat Biotechnol*, **30**, 679-692 (2012).
16. Tornio, A., et al., Clinical Studies on Drug-Drug Interactions Involving Metabolism and Transport: Methodology, Pitfalls, and Interpretation. *Clinical pharmacology and therapeutics*, **105**, 1345-1361 (2019).
17. Zhou, S.F., J.P. Liu, and B. Chowbay, Polymorphism of human cytochrome P450 enzymes and its clinical impact. *Drug metabolism reviews*, **41**, 89-295 (2009).
18. Chan, A., et al., Clinically significant drug-drug interactions between oral anticancer agents and nonanticancer agents: a Delphi survey of oncology pharmacists. *Clinical therapeutics*, **31 Pt 2**, 2379-2386 (2009).
19. Yoshida, K., et al., In Vitro-In Vivo Extrapolation of Metabolism- and Transporter-Mediated Drug-Drug Interactions-Overview of Basic Prediction Methods. *Journal of pharmaceutical sciences*, **106**, 2209-2213 (2017).
20. Jaiswal, S., et al., Novel pre-clinical methodologies for pharmacokinetic drug-drug interaction studies: spotlight on "humanized" animal models. *Drug metabolism reviews*, **46**, 475-493 (2014).
21. Food and Drug Administration. *In Vitro Metabolism- and Transporter- Mediated Drug-Drug Interaction Studies Guidance for Industry*. 2017, October 26; Available from: <https://www.fda.gov/regulatory-information/search-fda-guidance-documents/vitro-metabolism-and-transporter-mediated-drug-drug-interaction-studies-guidance-industry>.
22. Beckwitt, C.H., et al., Liver 'organ on a chip'. *Experimental cell research*, **363**, 15-25 (2018).
23. Sung, J.H., et al., Recent Advances in Body-on-a-Chip Systems. *Anal Chem*, **91**, 330-351 (2019).
24. Esch, M.B., et al., How multi-organ microdevices can help foster drug development. *Advanced drug delivery reviews*, **69-70**, 158-169 (2014).
25. Kim, J.Y., et al., 3D spherical microtissues and microfluidic technology for multi-tissue experiments and analysis. *J Biotechnol*, **205**, 24-35 (2015).
26. Lohasz, C., et al., Scalable Microfluidic Platform for Flexible Configuration of and Experiments with Microtissue Multiorgan Models. *SLAS Technology*, **24**, 79-95 (2019).
27. Emadi, A., R.J. Jones, and R.A. Brodsky, Cyclophosphamide and cancer: golden anniversary. *Nat Rev Clin Oncol*, **6**, 638-647 (2009).

28. Wang, D. and H. Wang, Oxazaphosphorine bioactivation and detoxification The role of xenobiotic receptors. *Acta Pharm Sin B*, **2**, 10.1016/j.apsb.2012.1002.1004 (2012).
29. Rock, B.M., et al., Characterization of ritonavir-mediated inactivation of cytochrome P450 3A4. *Mol Pharmacol*, **86**, 665-674 (2014).
30. Antoniou, T. and A.L. Tseng, Interactions between antiretrovirals and antineoplastic drug therapy. *Clin Pharmacokinet*, **44**, 111-145 (2005).
31. Torres, H.A., et al., Efficacy and safety of antiretrovirals in HIV-infected patients with cancer. *Clin Microbiol Infect*, **20**, O672-679 (2014).
32. Berretta, M., et al., Drug-Drug Interactions Based on Pharmacogenetic Profile between Highly Active Antiretroviral Therapy and Antiblastic Chemotherapy in Cancer Patients with HIV Infection. *Front Pharmacol*, **7**, 71 (2016).
33. Kim, J.Y., et al., 96-well format-based microfluidic platform for parallel interconnection of multiple multicellular spheroids. *J Lab Autom*, **20**, 274-282 (2015).
34. Lohasz, C., et al., Tubing-Free Microfluidic Microtissue Culture System Featuring Gradual, in vivo-Like Substance Exposure Profiles. *Front Bioeng Biotechnol*, **7**, 72 (2019).
35. ANSI/SLAS, ANSI/SLAS 1-2004: Microplates - Footprint Dimensions. (2004)
36. ANSI/SLAS, ANSI/SLAS 4-2004: Microplates - Well Positions. (2004)
37. Roessger, K., et al., Characterization and application of 3D Multi-Donor Human Liver Microtissues for predictive DILI testing and mechanistic investigations. *Toxicology Letters*, **258**, S150-S150 (2016).
38. Li, F., et al., Comparative metabolism of cyclophosphamide and ifosfamide in the mouse using UPLC-ESI-QTOFMS-based metabolomics. *Biochem Pharmacol*, **80**, 1063-1074 (2010).
39. Messner, S., et al., Transcriptomic, Proteomic, and Functional Long-Term Characterization of Multicellular Three-Dimensional Human Liver Microtissues. *Applied In Vitro Toxicology*, **4**, 1-12 (2018).
40. Boos, J.A., et al., Microfluidic Multitissue Platform for Advanced Embryotoxicity Testing In Vitro. *Advanced Science*, **6**, 1900294 (2019).
41. Renggli, K., et al., Integrated Microphysiological Systems: Transferable Organ Models and Recirculating Flow. *Advanced Biosystems*, **0**, 1900018 (2019).

42. Huang, Z., P. Roy, and D.J. Waxman, Role of human liver microsomal CYP3A4 and CYP2B6 in catalyzing N-dechloroethylation of cyclophosphamide and ifosfamide. *Biochem Pharmacol*, **59**, 961-972 (2000).
43. Struck, R.F., et al., Plasma pharmacokinetics of cyclophosphamide and its cytotoxic metabolites after intravenous versus oral administration in a randomized, crossover trial. *Cancer Res*, **47**, 2723-2726 (1987).
44. McCune, J.S., et al., Population pharmacokinetics of cyclophosphamide and metabolites in children with neuroblastoma: a report from the Children's Oncology Group. *Journal of clinical pharmacology*, **49**, 88-102 (2009).
45. Yang, L., et al., Pharmacokinetics and safety of cyclophosphamide and docetaxel in a hemodialysis patient with early stage breast cancer: a case report. *BMC Cancer*, **15**, 917 (2015).
46. Kurowski, V., et al., Metabolism and pharmacokinetics of oral and intravenous ifosfamide. *J Cancer Res Clin Oncol*, **117 Suppl 4**, S148-153 (1991).
47. Jahnke, K., et al., Pharmacokinetics and efficacy of ifosfamide or trofosfamide in patients with intraocular lymphoma. *Ann Oncol*, **16**, 1974-1978 (2005).
48. Willits, I., et al., Pharmacokinetics and metabolism of ifosfamide in relation to DNA damage assessed by the COMET assay in children with cancer. *Br J Cancer*, **92**, 1626-1635 (2005).
49. Gatti, G., et al., The relationship between ritonavir plasma levels and side-effects: implications for therapeutic drug monitoring. *AIDS (London, England)*, **13**, 2083-2089 (1999).
50. Li, A.P., A. Uzgaré, and Y.S. LaForge, Definition of metabolism-dependent xenobiotic toxicity with co-cultures of human hepatocytes and mouse 3T3 fibroblasts in the novel integrated discrete multiple organ co-culture (IdMOC) experimental system: Results with model toxicants aflatoxin B1, cyclophosphamide and tamoxifen. *Chemico-biological interactions*, **199**, 1-8 (2012).
51. Tong, S., et al., Establishment and assessment of a novel in vitro bio-PK/PD system in predicting the in vivo pharmacokinetics and pharmacodynamics of cyclophosphamide. *Xenobiotica; the fate of foreign compounds in biological systems*, **48**, 368-375 (2018).
52. Hall, A.G. and M.J. Tilby, Mechanisms of action of, and modes of resistance to, alkylating agents used in the treatment of haematological malignancies. *Blood Reviews*, **6**, 163-173 (1992).

53. Ponticelli, C., R. Escoli, and G. Moroni, Does cyclophosphamide still play a role in glomerular diseases? *Autoimmun Rev*, **17**, 1022-1027 (2018).
54. Mehta, G., et al., Opportunities and challenges for use of tumor spheroids as models to test drug delivery and efficacy. *Journal of Controlled Release*, **164**, 192-204 (2012).
55. Conger, A.D. and M.C. Ziskin, Growth of mammalian multicellular tumor spheroids. *Cancer Res*, **43**, 556-560 (1983).
56. Granvil, C.P., et al., Role of CYP2B6 and CYP3A4 in the in vitro N-dechloroethylation of (R)- and (S)-ifosfamide in human liver microsomes. *Drug metabolism and disposition: the biological fate of chemicals*, **27**, 533-541 (1999).
57. Springate, J., et al., Toxicity of ifosfamide and its metabolite chloroacetaldehyde in cultured renal tubule cells. *In vitro cellular & developmental biology. Animal*, **35**, 314-317 (1999).
58. Lindley, C., et al., The effect of cyclophosphamide with and without dexamethasone on cytochrome P450 3A4 and 2B6 in human hepatocytes. *Drug metabolism and disposition: the biological fate of chemicals*, **30**, 814-822 (2002).
59. Wang, D., et al., The role of constitutive androstane receptor in oxazaphosphorine-mediated induction of drug-metabolizing enzymes in human hepatocytes. *Pharmaceutical research*, **28**, 2034-2044 (2011).
60. Scripture, C.D. and W.D. Figg, Drug interactions in cancer therapy. *Nat Rev Cancer*, **6**, 546-558 (2006).
61. Palleria, C., et al., Pharmacokinetic drug-drug interaction and their implication in clinical management. *J Res Med Sci*, **18**, 601-610 (2013).
62. Long, T.J., et al., Modeling Therapeutic Antibody-Small Molecule Drug-Drug Interactions Using a Three-Dimensional Perfusable Human Liver Coculture Platform. *Drug metabolism and disposition: the biological fate of chemicals*, **44**, 1940-1948 (2016).
63. Millard, D.C., et al., Identification of Drug-Drug Interactions In Vitro: A Case Study Evaluating the Effects of Sofosbuvir and Amiodarone on hiPSC-Derived Cardiomyocytes. *Toxicol Sci*, **154**, 174-182 (2016).
64. Deng, J., et al., A cell lines derived microfluidic liver model for investigation of hepatotoxicity induced by drug-drug interaction. *Biomicrofluidics*, **13**, 024101 (2019).
65. McAleer, C.W., et al., Multi-organ system for the evaluation of efficacy and off-target toxicity of anticancer therapeutics. *Sci Transl Med*, **11**, eaav1386 (2019).

4 TUBING-FREE MICROFLUIDIC CULTURE SYSTEM FEATURING GRADUAL, IN VIVO-LIKE SUBSTANCE EXPOSURE PROFILES

Christian Lohasz, Olivier Frey, Flavio Bonanini, Kasper Renggli and Andreas Hierlemann. Tubing-free microfluidic microtissue culture system featuring gradual, in vivo-like substance exposure profiles. *Frontiers in Bioengineering and Biotechnology*, 7, 72 (2019).

DOI: 10.3389/fbioe.2019.00072

4.1 Abstract

In vitro screening methods for compound efficacy and toxicity to date mostly include cell or tissue exposure to preset constant compound concentrations over a defined testing period. Such concentration profiles, however, do not represent realistic *in vivo* situations after substance uptake. Absorption, distribution, metabolism and excretion of administered substances in an organism or human body entail gradually changing pharmacokinetic concentration profiles. As concentration profile dynamics can influence drug effects on the target tissues, it is important to be able to reproduce realistic concentration profiles in *in vitro* systems. We present a novel design that can be integrated in tubing-free, microfluidic culture chips. These chips are actuated by tilting so that gravity-driven flow and perfusion of culture chambers can be established between reservoirs at both ends of a microfluidic channel. The design enables the realization of *in vivo*-like substance exposure scenarios. Compound gradients are generated through an asymmetric Y-junction of channels with different hydrodynamic resistances. Six microtissues (MTs) can be cultured and exposed in compartments along the channel. Changes of the chip design or operation parameters enable to alter the dosing profile over a large range. Modulation of, e.g., the tilting angle, changes the slope of the dosing curves, so that concentration curves can be attained that resemble the pharmacokinetic characteristics of common substances in a human body. Human colorectal cancer (HCT 116) MTs were exposed to both, gradually decreasing and constant concentrations of Staurosporine. Measurements of apoptosis induction and viability after 5 h and 24 h showed different short- and long-term responses of the MTs to dynamic and linear dosing regimes

4.2 Introduction

In the last decades, microphysiological systems (MPSs) have been proven to better mimic human *in vivo* physiology in *in vitro* cell cultures. MPSs, often referred to as “organs on chips”, are *in vitro* platforms designed to model the spatial, chemical, structural, and physiological elements of *in vivo* cellular environments. In most cases, they include a combination of advanced cell culture models and microfluidic technology. In the last couple of years, a plethora of new, specialized systems have been presented by both, academia and industry ¹. The list of different systems ranges from single- to multi-organ platforms and include tissues in healthy or diseased states ². All these systems commonly include defined microchannel structures that enable fluidic interconnection. Perfusion enables to (i) precisely control the microenvironment

directly at the cell culture site, (ii) constantly deliver nutrients, oxygen, and other substances, (iii) establish a communication route between individual modules, i.e., organs or microtissues, and (iv) wash away cellular waste products. A precise liquid-flow and temperature control, as well as the possibility to very closely mimic *in vivo* situations make these tools very promising candidates for efficacy and/or toxicity testing of substances for the pharmaceutical industry, in particular as they allow to investigate processes in a more systemic way^{1, 3}. As those systems become better and better in reproducing *in vivo* situations in the human body, one of the remaining challenges that has been largely neglected in setting up an efficacy and toxicity screening pipeline is pharmacokinetics (PK).

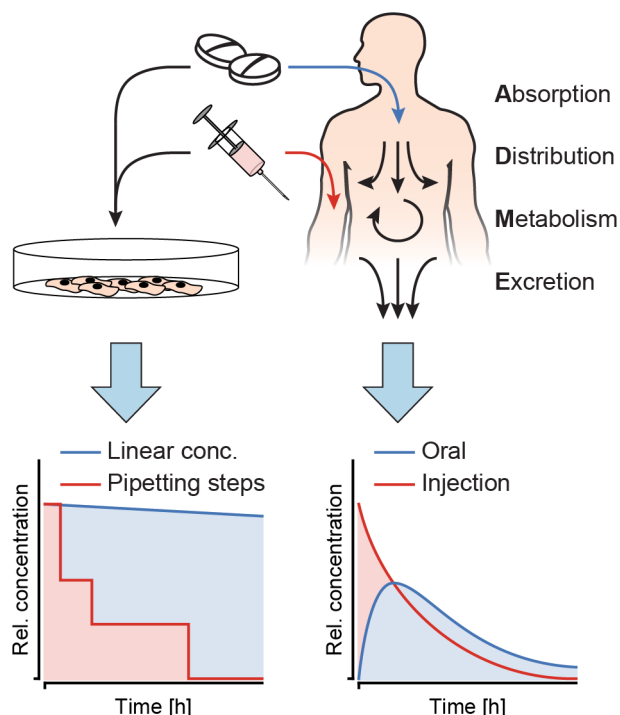


Figure 1: Substance concentration profiles in *in vitro* experiments as opposed to *in vivo*. Cell culture models *in vitro* are exposed to constant concentrations or sudden substance concentration steps generated by pipetting, while in the human body, the interplay of absorption, distribution, metabolism and excretion (ADME) produces distinct, dynamic substance concentration profiles upon oral administration or injection of a substance.

PK describe the fate of a substance, once it enters the human body. Upon entering, there are four key processes that happen with the substance (Figure 1): (i) absorption into the body through an epithelial barrier, (ii) distribution of the substance within the body or certain tissues, (iii) metabolization of the substance, and (iv) excretion of the substance itself and/or its metabolites. These four processes are summarized by the acronym ADME, and their interplay results in distinct concentration profiles over time in the human body, which highly depend on the nature of the substance and its administration. The concentration dynamics of a substance can also impact its efficacy and/or toxicity, since those dynamics define the exposure duration above a specific effective/toxic threshold concentration^{4, 5}. While *in vitro* model systems have been used to extract specific ADME parameters, only very few systems allow for exposure of

target organ models to such dynamic concentration profiles of a substance of interest. On the contrary, *in vitro* studies routinely include dosage of constant substance concentrations over a defined time, which are not representative of the *in vivo* situation. Figure 1 illustrates the differences between (left) *in vitro* substance concentration profiles, which are mostly linear, or, in some cases, more complex and then realized through precisely-timed, stepwise pipetting, and (right) dynamically and gradually changing *in vivo* concentration profiles. Studies showed that simplified protocols often lead to false positive results during toxicity and efficacy testing ⁶.

To attain an improved representation of pharmacokinetics in *in-vitro* systems, there are two major thrusts that are currently pursued and implemented. In a first thrust, a majority of the relevant organs that are involved in ADME are included and inter-linked in a single chip or microfluidic system ⁷⁻⁹. Substantial efforts are required for finding the appropriate organ ratio and for combining all organ surrogates so that they are functional at the same time in a common culture medium. This approach, therefore, entails very high biological complexity ¹⁰, which may compromise experimental reproducibility and throughput. In a second approach, pharmacokinetic concentration profiles are generated through rather complex external devices, for example, by a combination of multiple precision pumps that enable a defined temporal modulation of the substance concentration for specific single organs of interest ¹¹. There have been several attempts to use such systems and apply spatial and temporal gradients of substances on biological samples, such as *Xenopus* embryonic tissue ¹², or lymphoid tissue explants ¹³. Further, Song, Ryu¹⁴ investigated exposure of single cells to pulsatile and gradually ramped concentration profiles of growth factors. Another solution to expose cancer cells to pulses of tumor necrosis factor (TNF) without the need for external pumps, has been presented by Lee, Qasaimeh¹⁵. Perfusion in their chip was gravity-driven, and pulses of TNF were induced by manually elevating the dosing reservoir.

Here, we developed a new approach to generate dynamic substance concentration profiles in microfluidic cell culture systems. The proposed design and working principle can be integrated into tubing-free microfluidic platforms, which feature gravity-driven flow perfusion upon platform tilting. The specific new design feature consists of an asymmetric Y-junction, connected to three medium reservoirs ¹⁶. Upon repeated tilting of the chip, the liquids from the reservoirs mix, which gradually changes the substance concentration at the cell culture sites. The slope of the concentration profile can be modulated by changing the channel dimensions, the initial volume of the substance solution, or the tilting angle.

As a proof on concept, we integrated the new design feature into a microfluidic microtissue culture chip with 6 compartments that was similar to a previously presented approach^{17, 18}. Human colorectal tumor microtissues (HCT 116) were loaded into the MT compartments of the chip and exposed to Staurosporine. Staurosporine features strong, promiscuous kinase inhibitor properties by competitive binding to the ATP-binding site of kinases¹⁹. Therefore, it is frequently used as an anti-cancer tool compound for *in vitro* studies. The tumor microtissues (TuMTs) were exposed to a physiologically relevant concentration profile, which resembled that after an injection of a substance in a human body. This profile could be recreated by the chip system. The results were compared to constant-concentration drug dosing schemes. We saw that the TuMTs responded differently to *in vivo*-like drug dosing with decreasing concentrations in comparison to traditionally applied, constant concentrations.

4.3 Materials and Methods

4.3.1 Design principle

A microfluidic channel design was developed, that enables a gradual change of substance concentrations over time at the cell or MT culturing site. Prerequisite for the integration of the proposed design feature is a chip system with medium reservoirs at both ends of a main channel and a flow actuation upon tilting of the system. Cell or MT models are cultured in compartments along the main channel and perfused upon tilting the chip back and forth. The specific new design feature consists of an asymmetric Y-junction, which is connected to three medium reservoirs, two reservoirs at one end of the main channel and a third reservoir at the other end of the channel (see Figure 2).

To produce a gradually changing concentration profile in the main channel, the two reservoirs left of the Y-junction in Figure 2A are filled with two different medium compositions, e.g., plain cell culture medium and medium containing a substance of interest. Upon tilting of the chip so that the 2 reservoirs left of the Y-junction are higher, the two liquids in the reservoirs start flowing and combine in the Y-junction to flow along the common main channel. The different cross-sections of the two left channels entail different hydrodynamic resistances and different flow rates through the two channels into the main channel. Upon tilting in the opposite direction so that the reservoir at the right side is higher, a flow backwards to the Y-junction is

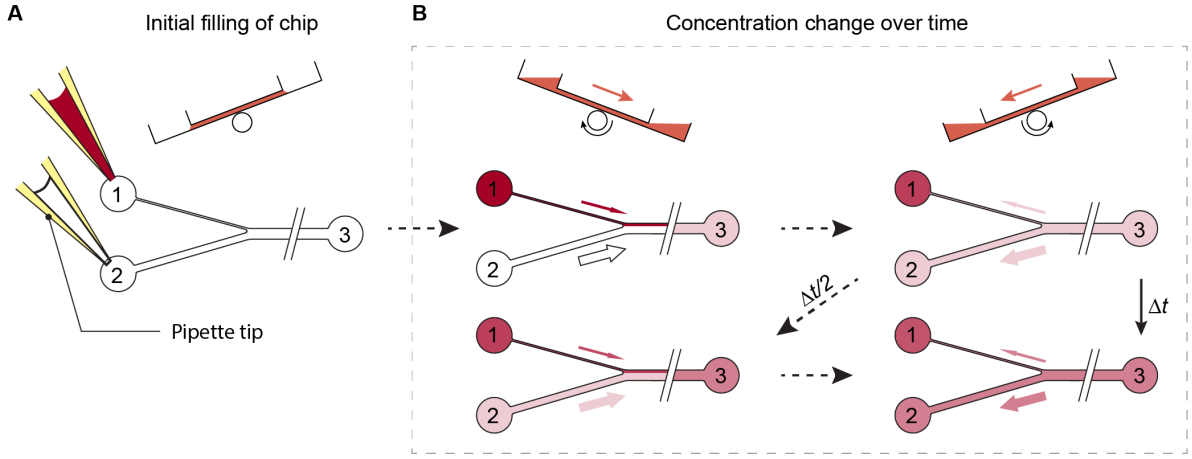


Figure 2: Working principle of the device. **(A)** Reservoirs 1 and 2 are filled with substance-loaded and plain cell culture medium. **(B)** Upon tilting of the chip, unequal volumes of liquid flow through the differently sized channels. While the substance concentration is, with each tilting interval Δt , gradually enriched in reservoirs 2 and 3, the substance is diluted in reservoir 1, until a concentration equilibrium is reached.

initiated. The liquid in the main channels then splits up at the Y-junction at the same volume ratio at which it entered the common channel before. Repeated tilting of the device with a defined tilting angle slowly mixes the media originating from the two reservoirs at the left side over time, until an equilibrium in the main channel is reached (Figure 2B). If, for example, a substance is added into the reservoir that is connected to the channel featuring the lower flow rate, and plain cell culture medium is applied to the other one, the substance concentration in the main channel is gradually enriched over time (Figure 2B).

The change in the substance concentration in the main channel depends on the different flow rates through the channels at the left side and the resulting total liquid volumes that are fed into the main channel per tilting interval (Figure 3B). Flow rates, in turn depend on the height difference or hydrostatic pressure difference between the upper and lower reservoirs of the tilting system. The tilting angle α and the distance L between the opposite ends of the channel define the height difference Δh between the two reservoirs, to which the height of the liquid column in the upper reservoir h_{up} is added and from which the liquid column height in the lower reservoir h_{low} is subtracted.

$$\Delta h = L \cdot \sin \alpha + h_{up} - h_{low} \quad (1)$$

In a rectangular channel, the hydrodynamic resistance R_h is dependent on the liquid viscosity and the channel dimensions, as described by Bruus²⁰:

$$R_h \approx \frac{12 \cdot \eta \cdot L}{w \cdot h^3 \cdot \left(1 - 0.63 \cdot \frac{h}{w}\right)} \quad (2)$$

with η denoting the liquid viscosity and L , w , and h ($w > h$) describing the length, width and height of the channel, respectively.

Using the tilting-dependent hydrostatic pressure difference

$$\Delta P = \rho \cdot g \cdot \Delta h \quad (3)$$

and the hydrodynamic resistance R_h (equation 2) of each section of the channel, the volumetric flow rates Q in each section of the channel can be calculated as:

$$Q = \frac{\Delta P}{R_h}. \quad (4)$$

The flow rates in the three channels connected to the Y-junction then are determined by:

$$Q_1 + Q_2 = Q_3 \quad (5)$$

with Q_1 and Q_2 referring to the differently sized channels joining into the common channel featuring a flow rate Q_3 (Figure 3B).

To establish unequal flow rates in the two channels left of the Y-junction, their hydrodynamic resistances or geometric dimensions can be adjusted. Thus, a change of dimensions, such as the channel widths of the two channels, allows for simple adjustment of their specific hydrodynamic resistances. Figure 2 shows a schematic view of the microfluidic-channel layout with an integrated, asymmetric Y-junction. To predict the substance concentration in the common channel, the dilution equation:

$$C_x \cdot V_x = C_y \cdot V_y \quad (6)$$

was used and adjusted to calculate the concentration resulting from mixing three liquids:

$$C_3(t) = \frac{C_1 \cdot V_1(t) + C_2 \cdot V_2(t) + C_3(t_0) \cdot V_3(t_0)}{V_1(t) + V_2(t) + V_3(t_0)}. \quad (7)$$

C_3 refers to the concentration in the common channel and reservoir 3 at time point t after tilting of the chip. C_1 and C_2 represent the concentrations of the liquids in the differently sized channels upstream of the Y-junction, and V_1 and V_2 are the liquid volumes flowing into the main channel during time t . $C_3(t_0)$ and $V_3(t_0)$ denote the concentration and volume of the liquid phase already present in the main channel before initiation of the tilting cycle. The liquid volumes V_1 and V_2 can further be described by:

$$\begin{aligned} V_1(t) &= Q_1 \cdot t, \text{ and} \\ V_2(t) &= Q_2 \cdot t \end{aligned} \quad (8)$$

with t denoting the time, during which the flow rates Q_1 and Q_2 are present in the two differently sized channels and during which the liquid flows into the common channel.

Equation (7), combined with equations (4) and (8), was then used to derive the time-dependent recurrence relation for calculating the concentrations in the system, when the chip is tilted towards reservoir 3:

$$C_3(t + \Delta t) = \frac{C_1(t) \cdot Q_1 \cdot \Delta t + C_2(t) \cdot Q_2 \cdot \Delta t + C_3(t_0) \cdot V_3(t)}{Q_1 \cdot \Delta t + Q_2 \cdot \Delta t + V_3(t)}. \quad (9)$$

When tilting the chip into the opposite direction, the concentrations in reservoirs 1 and 2 can be calculated using:

$$C_1\left(t + \Delta \frac{t}{2}\right) = \frac{C_3(t) \cdot Q_3 \cdot \Delta t + C_1(t) \cdot Q_1 \cdot \Delta t}{Q_3 \cdot \Delta t + Q_1 \cdot \Delta t}, \text{ and} \quad (10)$$

$$C_2\left(t + \Delta \frac{t}{2}\right) = \frac{C_3(t) \cdot Q_3 \cdot \Delta t + C_2(t) \cdot Q_2 \cdot \Delta t}{Q_3 \cdot \Delta t + Q_2 \cdot \Delta t}. \quad (11)$$

Here, Δt denotes the interval between two successive tilting cycles into the same direction, and $\Delta t/2$ between two tilting steps into the opposite direction (Figure 2B). $C_1(t)$, $C_2(t)$, and $C_3(t)$ are the time-dependent concentrations in reservoirs 1 to 3, and $V_3(t)$ is the time-dependent liquid volume within the main channel and in reservoir 3. At $t = 0$, all channels are assumed to be filled with plain cell culture medium. Equations (9) to (11) allow for simple calculations of the analyte concentration in the main channel and in the reservoirs at discrete times.

4.3.2 Chip fabrication

The chip was fabricated using polydimethylsiloxane (PDMS) and conventional soft lithography methods. The bottom structures comprised the channel structures and were fabricated using a two-layer SU-8 master on a 4-inch silicon wafer (Supplementary Figure 1). For the first layer with the perfusion channel designs, SU-8 100 photoresist (Microchem Corp., Newtown, MA, USA) was spin-coated onto the wafer in a 100- μm thick layer and was exposed to UV through a transparency mask featuring the designed pattern. The second 25- μm -thick layer of SU-8 25 photoresist (Microchem Corp.) comprising the mixing structures was coated on top of the first layer and was exposed a second time to UV through a transparency mask.

For the top structures of the chip, a positive mold of the chip was designed and 3D-printed (Protolabs, Feldkirchen, Germany). The structures comprised the top part of the MT compartments and the reservoirs. The positive mold was then used to cast a flexible, negative mold out of PDMS (Dow Corning, Midland, MI, USA). A 7:1 ratio of polymer and curing agent were used for better stability, and the cast was cured at room temperature for 24 h to reduce heat-induced shrinking of PDMS as much as possible²¹. The SU-8 bottom mold and the PDMS top mold were then placed in a desiccator and treated with trichloro(1H, 1H, 2H, 2H-perfluorooctyl)silane (Sigma-Aldrich Chemie GmbH, Buchs, Switzerland) to prevent fusion with the final chip and to enable multiple usage of both molds.

Designated alignment structures enabled the easy and fast alignment of the two molds, before PDMS was filled and cured in a vacuum oven at 80 °C for 4 h. Subsequently, the casted PDMS devices were removed from the molds and cut into their final size of 23 mm × 73 mm. To close the channels at the bottom side, the PDMS devices were O₂-plasma-bonded to microscopy glass slides that were previously spin-coated with a thin layer of PDMS (30 s, 2000 rpm). The PDMS layer on the glass slide was needed to achieve uniform coating properties of all four channel surfaces. The glass slides enabled easy device handling and use with standard inverted microscopy setups. After the assembly, all channels and surfaces to be exposed to liquids or cells were coated with Biolipidure 206 (NOF America Corporation, White Plains, NY, USA) to render them hydrophilic and to prevent MTs from attaching to the surfaces.

4.3.3 Device operation

The devices were operated in a handling frame (Microfluidic ChipShop, Jena, Germany) holding four chips in parallel. To limit evaporation, a custom-cut adhesive polyester film with small holes for oxygen exchange was attached to cover the MT compartments and the medium reservoirs. Further, a lid (Microfluidic ChipShop), fitting to the handling frame, was used to close the chips and enabled stacking of multiple frames.

Channels and reservoirs were initially flooded with plain cell culture medium to a level that standing drops formed within the top rim of the MT compartments. Throughout the experiment, these standing drops remained stable at the top rim structure of the MT compartments. Surface tension stabilized the standing drops, which resulted in a constant volume in the compartment. Next, preformed spherical MTs were transferred into the corresponding compartments. They

were harvested from a 96-well microtiter plate with a pipette. After sedimentation of the MTs to the opening of the pipette tip, the tip was brought into contact with the standing drop. The MT then sedimented down – driven by gravity – to the bottom of the designated compartment.

Before starting an experiment, the frame was tilted along its long axis with the branched side facing down while the upper reservoir on the other side was completely emptied of medium. The channels did not completely drain due to capillary forces at the connections to the reservoirs. The medium in the two lower reservoirs was then removed and replaced with the required volume of plain medium and medium containing a substance of interest at a predefined concentration. The reservoirs could hold a maximum volume of 100 μL . To achieve dosing curves with increasing concentration, the substance was administered into the reservoir connected to the narrow channel. For dosing curves featuring decreasing concentrations, the reservoir connected to the wide channel was loaded with the substance. After loading, repetitive tilting was started and the experiment began.

The assembled and loaded handling frame was operated on a programmable tilting stage (InSphero AG, Schlieren, Switzerland), as shown in Supplementary Figure 2. The stage allows for precise adjustment of positive and negative tilting angles, for defining resting times at tilted or horizontal positions and transition times between positive and negative angles. The entire experimental setup including the tilting stage and a stack of handling frames was operated in a standard cell-culture incubator at mammalian cell culture conditions (37 °C, 5% CO₂, 95% humidity).

4.3.4 Measurements of concentration curves

To track concentration curves over time, cell culture medium containing amaranth red dye (Sigma-Aldrich, Buchs, Switzerland) was used to mimic a drug solution. 100 μL of the dye solution were loaded into one reservoir at the branched side of the channel and 100 μL of plain cell culture medium were added to the other one at the same side of the chip. While repeatedly tilting the chip, 1 μL of the mixed liquid was removed from the shared reservoir on the other side of the chip, and its absorbance at a wavelength of 520 nm was measured in reference to the initially loaded solution of amaranth red using a NanoDrop2000 (Life Technologies Europe B.V., Zug, Switzerland).

For the realization of concentration profiles that resembled *in-vivo* concentrations after injection of a substance, cell culture medium containing 15 μ M 5-fluorouracil (5-FU; Sigma-Aldrich) was used, along with plain cell culture medium in the chip. To measure the concentration profile, medium-filled chips with and without tumor microtissues (TuMTs) were used. 25 μ L of drug-containing medium were loaded into the reservoir, connected to the wide channel, and 75 μ L of plain medium were loaded into the reservoir with the narrow channel. The concentration profile was induced by tilting the chip at a tilting angle of 20° with waiting times of 2 min and 30 s at the tilted positions and transition times of 30 s. Samples of 10 μ L were taken from the common reservoir after 3, 15, 33, 63, 123 min and after 24 h. For each time point, individual chips were used. The samples were diluted with 40 μ L of plain medium and snap-frozen on dry ice. 5-FU was externally quantified by ultra-performance liquid chromatography, coupled to mass spectrometry UPLC-MS (Admescope Oy, Oulu, Finland).

4.3.5 Cell culturing

HCT 116 colorectal tumor cells (ATCC®, LGC Standards GmbH, Wesel, Germany) were used for cell culture experiments. The cells were maintained in RPMI-1640 basal medium (Gibco, Fisher Scientific, Illkirch Cedex, France), supplemented with 10% fetal bovine serum (FBS, Sigma-Aldrich) and 1% penicillin/streptomycin (Life Technologies Europe B.V.). Cells were passaged at 80% confluency. To form MTs with a diameter of 200 – 250 μ m, 70 μ L of medium, containing 300 cells, were transferred into each well of an Akura™ 96-well plate (InSphero AG) and centrifuged for 2 min at 250 \times g. The plate was then placed in a tilted position in an incubator to collect cells in one corner of the wells and to promote MT formation. Cells were used for further experiments after 96 h.

4.3.6 Dosing experiments

For physiological dosing experiments, previously formed and equally sized MTs were transferred into the six MT compartments of the microfluidic chip. Briefly, MTs were aspirated together with 3 μ L of cell culture medium using a standard micropipette. Upon sedimentation of the MT by gravity to the opening of the pipette tip, the MT was transferred into the MT compartment by contact transfer.

To produce gradually decreasing concentrations over time, which are representing concentration profiles, e.g., upon intravenous injection of a drug, 25 μL of the drug solution containing the maximum concentration ($C_{\text{max}} = 0.75 \mu\text{M}$ Staurosporine) were loaded into the reservoir, connected to the wide channel, while 75 μL of plain cell culture medium were loaded into the reservoir connected to the thin channel. The unequal amounts of input liquids enabled to decrease the compound concentration to 25% of the initial concentration. Side by side to the gradually changing concentration profile, MTs were exposed to a constant concentration of 0.75 μM Staurosporine. Control groups were cultured without compound in the chip under identical perfusion conditions and under static conditions in 96-well microtiter plates. The tilting angle was set to 20° , tilting intervals to 2 min 30 s and transition times to 30 s. The chips were then repeatedly tilted. For imaging, the tilting was briefly interrupted, and the plate was transferred onto a microscope. Experiments were performed with at least six MTs per chip and 2 – 4 chips per condition.

4.3.7 Biochemical assays

Intracellular adenosine triphosphate (ATP) was measured using the CellTiter-Glo® 3D Cell Viability Assay (Promega AG, Dübendorf, Switzerland) as a measure of MT viability. The Caspase 3/7-Glo® Assay Systems (Promega AG) was used to assess onset of apoptosis. For both assays, MTs were removed from the chip and transferred into Akura 96-well plates (InSphero AG). MTs were washed with PBS (Life Technologies Europe B.V.), before the assay was performed according to the manufacturer's protocol.

4.3.8 Imaging

Bright-field images of MTs were recorded using an inverted wide-field microscope (DMI-6000B; Leica Microsystems AG, Heerbrugg, Switzerland), equipped with a CCD camera (DFC-340-FX; Leica) and a stage-top cell culture incubator to maintain cell-culture conditions during the imaging process (Life Imaging Services GmbH, Basel, Switzerland). To focus on the elevated microfluidic chips in the handling frame, a distance ring (Thorlabs GmbH, Dachau, Germany) was used to increase the parfocal length of the objective. All images were analyzed using ImageJ/Fiji software.

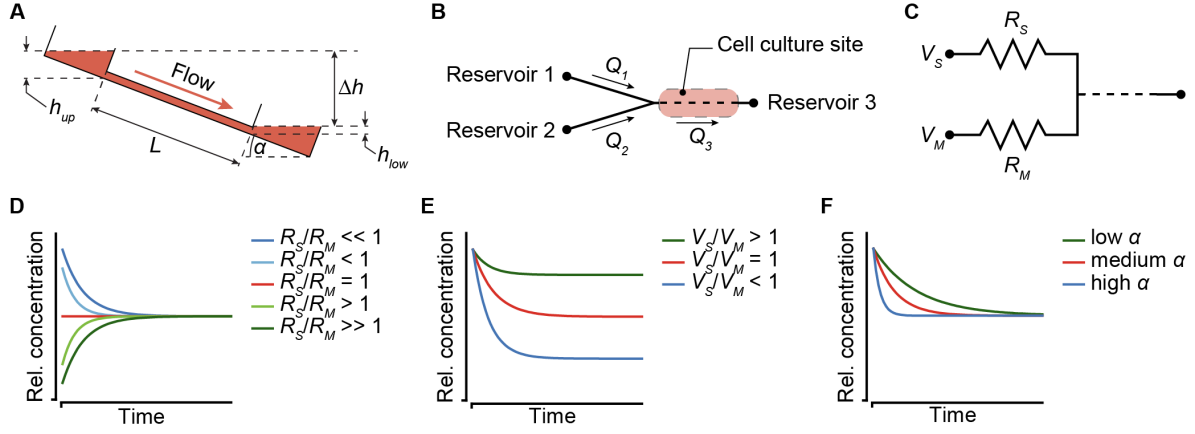


Figure 3: Modulation of concentration profiles. **(A)** Flow in the chip is dependent on the tilting angle α and the resulting height difference Δh between the liquid levels in the reservoirs at the left and right side. **(B)** Two reservoirs that are connected to channels with unequal flow rates Q_1 and Q_2 feed into a Y-junction. The flow-rate difference can be generated by different channel widths or dimensions. A cell culture site is located between the Y-junction and a third reservoir, and can be subjected to dynamic substance concentration profiles. **(C)** The channel resistances R_S and R_M , the initially applied liquid volumes V_S and V_M , and the tilting angle α can be used to modulate the concentration profiles. **(D)** The ratio of resistances can be used to define the time, after which an equilibrium is reached (for constant V and α). **(E)** The ratio of input volumes in reservoirs 1 and 2 defines the concentration, at which an equilibrium is reached (for constant R and α). **(F)** The tilting angle α modulates the slope of the concentration profile (for constant R and V).

4.4 Results

4.4.1 Modulation of the concentration profile

The new microfluidic channel design is aimed at reproducing physiologically relevant drug dosing curves *in vitro*. Operation of the chip was intended to be simple and not to rely on additional equipment, such as tubing and pumps. Therefore, the concept of gravity-driven flow by tilting of the chip was applied. Nevertheless, the new design features great flexibility in producing a variety of substance concentration profiles.

Three parameters can be changed to modulate the shape of the produced dosing curve: (i) the dimensions of the channels, (ii) the liquid volumes in the reservoirs at the beginning of an experiment, and (iii) the tilting angle during an experiment. The influence of these three parameters is illustrated in Figure 3A. The hydrodynamic resistance R_S and the initial input volume V_S denote those of the channel containing medium with a compound, while R_M and V_M denote those of the channel with plain medium. The normalized concentration profile curves

were calculated using equation (10) after each tilting interval. The initial concentrations were set to 0 in V_M and in the main channel, and 1 in V_S .

- (i) Modulation of the channel dimensions (Figure 3D): Equation (4) defines how the flow rates through the channels depend on their hydrodynamic resistance R_h . The resistance, in turn, is determined by the channel dimensions, e.g., the channel width (equation (2)). Thus, the flow rates through the two channels upstream or left of the Y-junction (Figure 3B) can be individually modulated by adjusting their hydrodynamic resistances R_S and R_M . The R_S -to- R_M -ratio influences the mixing ratio of the two liquids originating from the two separate reservoirs. Very large or very small R_S -to- R_M -ratios result in slowly increasing/decreasing concentrations until an equilibrium is reached. The lower the difference of R_S and R_M , the shorter and steeper become the concentration curves. For $R_S/R_M < 1$, a curve with decreasing concentrations is produced, while $R_S/R_M > 1$ yields increasing concentrations. Equal flow resistances in both channels result in linear, stable concentrations over time.
- (ii) Varying the initial volumes in the reservoirs (Figure 3E): The initially applied liquid volumes V_S and V_M determine the equilibrium concentration at the end of the gradual concentration change, i.e., the dilution of the initial substance concentration. For equal volumes in both reservoirs at the beginning of an experiment, the equilibrium is reached at 50% of the initial substance concentration. For $V_S/V_M > 1$, the concentration profile covers only a small range, before equilibrium is reached at a concentration, which is higher than 50% of the initial substance concentration. For $V_S/V_M < 1$, the opposite holds true. Loading unequal amounts of liquid into the reservoirs also results in different Δh between the lower reservoir at the right side and the two upper reservoirs at the left upon first tilting. The different Δh has an effect on the respective flow through the two channels, which also needs to be taken into account for calculating the flow rates and the concentration profile.
- (iii) A variation of the tilting angle of the chip during an experiment can be used to modulate the slope of the dosing curve on demand. The higher the tilting angle, the higher are the flow rates in all channels and, consequently, the steeper becomes the slope of the dosing curve. Figure 3F shows concentration curves at low (~ 5 -

10°), medium (~ 10 - 30°) and high (~ 30 - 50°) tilting angles α , while hydrodynamic resistances and input volumes were kept constant.

The possibility to vary these three parameters leads to a large flexibility in dosing regimens. While the latter two parameters (reservoir filling volume and tilting angle) can be changed during operation, the channel dimensions have to be already defined while designing the microfluidic chip. Practically, the chip has been designed to cover a fairly wide range of dosing curve slopes, which can be fine-tuned by adjusting the input volume and tilting angle to obtain the intended dosing curve.

4.4.2 Design integration into a microfluidic microtissue culture chip

To test the new design, we integrated it into a previously developed microfluidic microtissue culture chip. The original chip features two parallel channels, each with one reservoir at each side and 10 compartments in between, which can be used to culture spherical MTs under constant substance concentrations. The chip is operated by tilting¹⁸. The basic channel and compartment structure of the chip was maintained. On one side, the left side in Figure 4, a second reservoir and the Y-junction were implemented and the number of MT compartments was reduced to six. Further, a mixing structure was added (Figure 4A). As turbulent mixing does not occur at the inherently low Reynolds numbers in microchannels, mixing structures are required to obtain a homogenous substance concentration²². Therefore, we implemented a meander-shaped channel and so-called herring bone structures²³ between the Y-junction and the six MT compartments (Figure 4C). The mixing structure smoothened the sharp spatial gradient originating from the two reservoirs across the channel width to expose all MTs to an almost uniform substance concentration (Supplementary Figure 3 and Supplementary Movie 1). By connecting the chip to syringe pumps and by perfusing it with differently colored solutions, we could show that substance concentrations in all MT compartments change uniformly and in accordance with the concentrations inside the main channel. Furthermore, no differences could be observed between the first and the last MT compartment along the perfusion direction (Supplementary Figure 4 and Supplementary Movie 1).

In addition to the dosing channel with the Y-junction, a control channel was included into each chip. This control channel is similar to the dosing channel, but lacks the Y-junction. Instead, it features a single channel, the design parameters of which were adjusted to obtain similar

hydraulic resistances as in the dosing channel, and one reservoir (Figure 4F). The two differently sized channels leading into the Y-junction were 400 μm and 100 μm wide. The width of the first segment at the left in the control channel was 400 μm wide, and both main channels with MT compartments were 600 μm wide. All channels had a height of 100 μm . Having these two device architectures side by side on the same chip, the effects of a gradually changing concentration profile could be compared to those obtained by applying a linear concentration on the same chip. Twelve MTs were exposed to two different dosing conditions (6 per condition) in each device.

The MT compartments (Figure 4D) are open to the top to facilitate loading of externally produced MTs and their removal after an experiment to be able to individually analyze each MT. Surface tension of the medium generates a liquid-air-interface (*Standing Drop Port*, Fig. 4E) defined by the hydrophobic rim structure of the MT compartment. During experimentation,

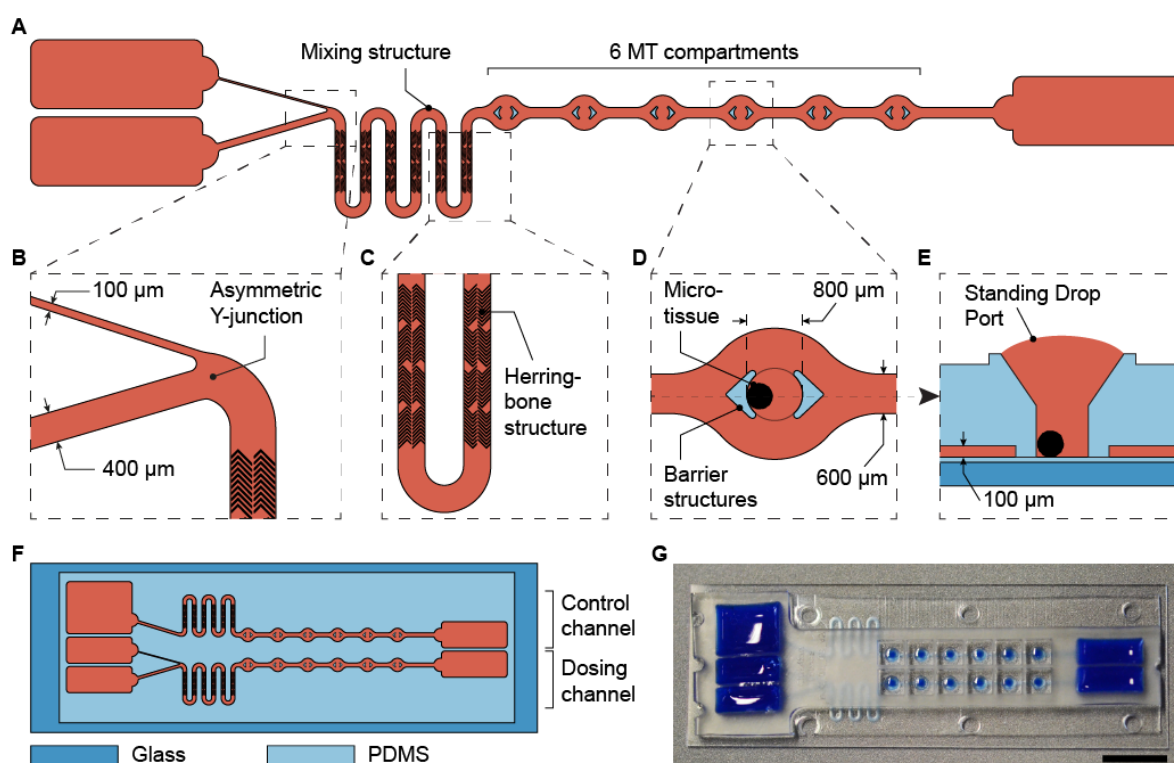


Figure 4: Integration of the asymmetric design into a microfluidic microtissue-culture chip. (A) Microfluidic channel layout with the asymmetric Y-junction, followed by a mixing structure and six microtissue (MT) compartments. Details are shown in (B) the asymmetric Y-junction, (C) the micromixer including herringbone structures in a meander-shaped channel, and (D) the top view of a MT compartment with protective barrier structures and (E) a side view of a MT compartment. (F) Each microfluidic chip has the size of a microscopy slide and includes a dosing channel with a Y-junction, next to a control channel for linear exposure profiles. (G) Photograph of the microfluidic chip the channels and reservoirs of which have been filled with a colored liquid (scale bar: 10 mm).

barrier structures hold the MT in place, and protect them from shear stress as a consequence of the liquid flow (Figure 4D). The barrier structures, however, do not hinder mass transport of biomolecules to the MT culturing site, as confirmed by the streamlines in a flow simulation (Supplementary Figure 2C). The details of the MT compartment design and the flow through the compartment have been thoroughly described and characterized previously^{24, 18}. The MT compartments are 800 μm in diameter and are spaced at a pitch of 4.5 mm. Rectangular reservoirs at the ends of the channels contain up to 150 μL per channel. The chip was fabricated using PDMS, and had a total size of 25 mm x 75 mm.

4.4.3 Concentration profile characterization

We designed a chip that could be used to deliver approximately typical, decreasing blood-plasma concentrations of substances that are administered to patients by injection²⁵. Injection of compounds generally results in initially high-concentration peaks, followed by a decrease over time (Figure 1). For the two channels at the left or upstream of the Y-junction in the dosing device, we used 400 μm width and 100 μm width.

We demonstrated the flexible modulation of the concentration profile on demand upon changing the tilting angle α (Figure 5A) through concentration measurements of amaranth red dye in the shared reservoir at the right side. Dye solution was loaded into the reservoir connected to the narrow channel, while plain medium was loaded into the other one. Repeated tilting resulted in a gradual increase of the dye concentration within the main channel and the shared reservoir. Figure 5A shows the measured curves for tilting angles of 20° and 40° until a concentration equilibrium was reached (after 6.5 h at 20° and after 3.5 h at 40°). The curve was also compared to calculated curves for the respective chip dimensions and a V_S -to- V_M -ratio of 1. The measured concentrations matched the calculated values, however, with a small offset. Furthermore, the curve, obtained with a tilting angle of 20°, showed minor fluctuations between 2 and 4 h. Both features can be explained by medium evaporation due to opening of the chip system at 15-min intervals for sampling. The results show that the concentration increase to a steady state concentration is faster with a steeper slope at higher tilting angles. A modulation of the shape of the dosing curve by changing the tilting angle α was indeed possible.

For obtaining decreasing concentration profiles, the wide channel was used for the substance-containing medium, and the narrow channel for plain medium. By interchanging the two liquids

in the reservoirs, as compared to the first characterization experiment, a R_S -to- R_M -ratio > 1 was achieved. Decreasing concentration profiles could be used to reproduce physiologically relevant conditions upon injection of a compound. For this second characterization experiment, 5-fluorouracil (5-FU) was used. 5-FU is a commonly used anti-cancer drug, which is administered by infusion or injection²⁶. Tilting was started with an angle of 20° , and samples were taken from the shared reservoir at the right side after 15, 33, 63, and 123 min, as well as after 24 h. 5-FU concentrations were measured by mass spectrometry (Figure 5B). The measured points were in good agreement with the calculated concentration profile and a steeply decreasing dosing curve was produced. A steady state at 25% of the initially applied concentration could be reached by applying a V_S -to- V_M -ratio of 0.66. The steady state was reached after approximately 2 h of continuous tilting of the chip.

The results of the two characterization experiments showed that concentration profiles can indeed be modulated by changing parameters, such as tilting angles (Figure 5A), resistances of the channels, or input volumes in the reservoirs (Figure 5B). One major difference between the concentration profiles produced with the device and the ones found *in vivo* is that the final equilibrium substance concentration obtained with the microfluidic chip is defined by the two initial concentrations and volumes in the reservoirs at the left and is always larger than 0, whereas the substance is eliminated completely in the human body in case of a single dosage. A possible solution to also reach a concentration of 0 with the microfluidic chip could include medium exchanges after the intended exposure time. Moreover, most substances are, to a certain amount, metabolized by the respective target tissue, which – depending on the initial substance concentration – might also contribute to decreasing the final concentration to physiological levels.

According to the MT compartment design, all MTs sit under a vertical liquid column of approx. 1 μL , which is not fully subjected to active perfusion from the channels. Alterations of the exposure profile by diffusion effects originating from these liquid columns, however, were considered negligible. This assumption is based on the small volume of the liquid columns in comparison to the continuous active perfusion with flow rates of 10 – 25 $\mu\text{L min}^{-1}$, depending on the tilting angle.

All in all, the proposed chip features large flexibility to produce concentration profiles that resemble those of *in-vivo* scenarios upon injection of a substance. Concentration curves in the chip system could reliably be predicted and reproduced.

4.4.4 Dosing experiments

After the new system had been characterized, it was tested by exposing a tumor MT (TuMT) model to a gradually decreasing, PK-like dosing profile, and, for comparison, to a constant dose (Figure 6A). We used the human colorectal cancer-cell line HCT 116 as a suitable tumor model, based on (i) the possibility to reliably generate uniform TuMTs, and (ii) its sensitivity to Staurosporine. Staurosporine is an anti-cancer tool compound, commonly used for *in vitro* studies. It acts as a potent, promiscuous kinase inhibitor and induces apoptosis in proliferating cancer cells^{27, 19}. The dosing curve that was previously characterized with 5-fluorouracil (5-FU) was applied to the TuMTs over a duration of 24 h. The initial maximum concentration (C_{\max}) of the PK-curve was chosen as constant concentration for comparison. A concentration of 0.75 μM was determined as C_{\max} by a static titration prior to the dosing experiment (Supplementary Figure 5).

After 5 h and 24 h of incubation, caspase 3 and 7 activity was measured to assess the induction of apoptosis as a reaction to the different Staurosporine treatment strategies (Figure 6B). After 5 h of treatment, TuMTs under both treatment conditions showed increased caspase 3/7 activity, as compared to the untreated controls. Moreover, TuMTs treated constantly with the C_{\max} concentration showed higher levels of apoptosis. Measurements of apoptosis after 24 h indicated slightly increased caspase activity for the C_{\max} condition, while caspase levels were similar to those of the control groups for the PK-like dosing regimen. Figure 6C shows intracellular ATP concentrations of the TuMTs as a measure of viability after 5 h and 24 h. The

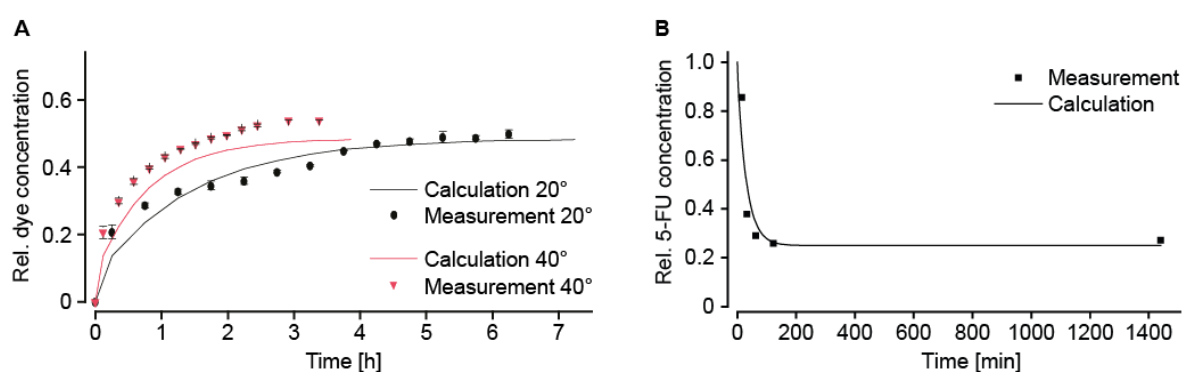


Figure 5: Modulation of the substance concentration profile. **(A)** Amaranth red dye was used to simulate and track substance concentrations in the chip over time. Changing the tilting angle α modulates the slope of the concentration curve ($V_S/V_M = 1$; $R_S/R_M = 4$; $n = 3$ chips). **(B)** Decreasing concentration of 5-fluorouracil (5-FU) in the main channel over time. Peak area and concentration measurements were done by means of ultra-performance liquid chromatography, coupled to mass spectrometry UPLC-MS ($V_S/V_M = 0.66$; $R_S/R_M > 0.25$; $\alpha = 20^\circ$; $n = 1$ chip).

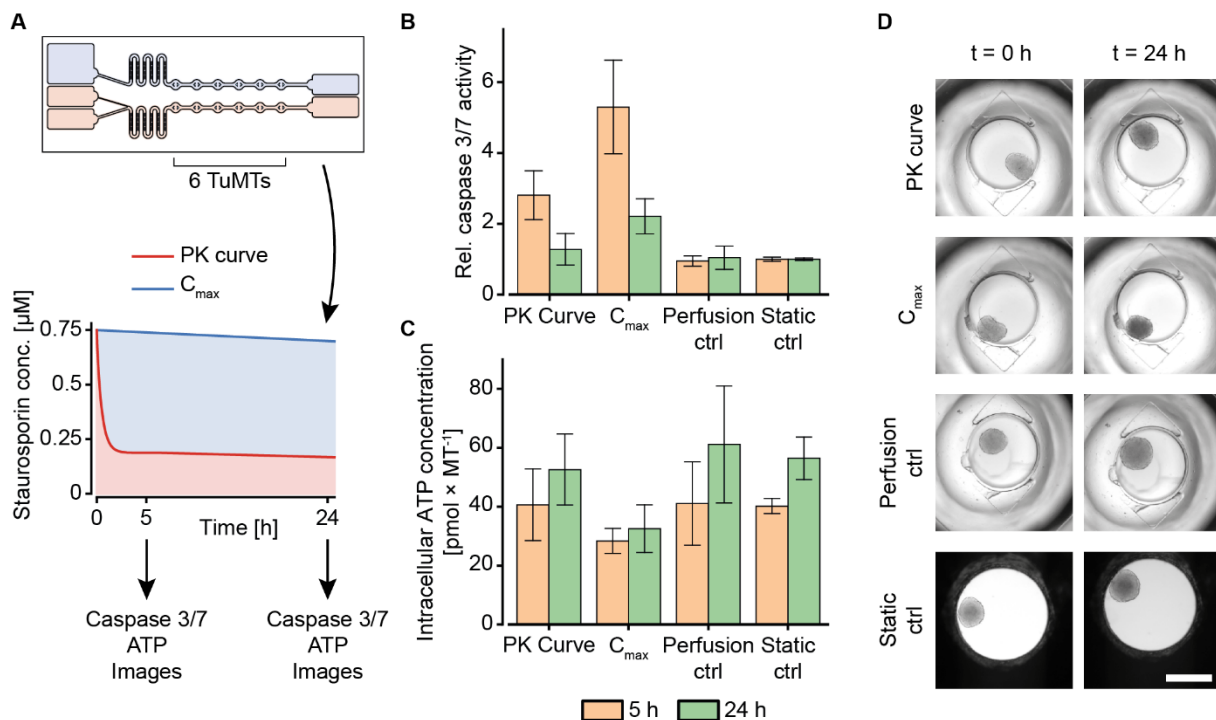


Figure 6: Staurosporine treatment of human colorectal tumor (HCT 116) microtissues (TuMTs) in the microfluidic chip. **(A)** Experimental layout: A chip was used to expose six TuMTs per channel to a PK-like dosing profile or a constant dose. The initial maximum concentration (C_{\max}) of the PK-like profile was chosen as the constant concentration for the second channel. The perfusion control and the static control MTs were cultured without any compound treatment in the chip and in a 96-well microtiter plate, respectively. Readouts were taken 5 h and 24 h after treatment start. **(B)** Relative caspase 3/7 activity, normalized to those of the static control of the respective sampling time points (data represented as mean \pm SD; $n = 6 - 12$ TuMTs). **(C)** Intracellular ATP concentration as a measure of viability (data represented as mean \pm SD; $n = 6 - 12$ TuMTs). **(D)** Representative images of TuMTs on the chip and in the microtiter plate at 0 h and 24 h (scale bar: 500 μm).

increasing ATP concentrations for all conditions over time indicate proliferation of the cancer cells in the TuMTs. While ATP concentrations in the PK-treated and the control MTs increased to a similar extent, they remained almost constant for the C_{\max} -treated MTs. Bright-field images of the conditions at the start of the experiment and after 24 h confirm the ATP findings, as they show slight MT growth for all conditions, except for the C_{\max} -treated ones (Figure 6D). Furthermore, a constant high dose of Staurosporine led to a morphological change of the TuMTs, which appeared darker and denser after 24 h of treatment. Noteworthy, the switch from static to perfusion culture did not affect cell viability and health, as can be seen by comparing the perfusion control to the static control (Figure 6B to 6C). This observation indicates that flow-induced shear stress on the TuMTs does not compromise their characteristics and

behavior, and it evidences that the developed device is suitable for assessing effects of pharmacokinetic substance profiles on TuMTs.

The acquired data indicated, that the different treatment conditions with the same starting concentration may, indeed, yield different results. While the anti-cancer effect of Staurosporine lead to an early onset of apoptosis for the PK-profile, the mid-term and long-term effect was more prominent for the constant high dose. The experiments highlight that a certain threshold concentration of an active compound has to be maintained over the treatment duration in order to obtain the desired effect. Metabolization effects of administered compounds as they occur *in vivo*, however, may decrease the concentration even more rapidly so that it may be difficult to maintain the concentration within the therapeutic window. In any case, it is advantageous for an *in vitro* system that is intended to reproduce the *in vivo* situation as much as possible to have options to adapt the dosing profile to accommodate various effects and maintain critical concentrations.

4.5 Discussion

We presented in this article a technical solution for the exposure of cellular models to temporal gradients of a substance of interest. The concentration profile was achieved by an asymmetrical Y-junction in a microfluidic microtissue culture chip that relied on perfusion by gravity-driven flow. We did not use external pumps and tubing, and we applied SBS Standard ANSI/SLAS 4-2004 for the MT compartments and Standard ANSI/SLAS 1-2004 for the chip handling frames,²⁹ so that our platform meets all criteria for parallelization and automation of experiments.

Other systems featuring dynamic exposure profiles of cellular model systems have been presented in the last couple of years. Song, Ryu¹⁴ presented a system to expose HEK cells to short pulses and gradually ramped profiles of epidermal growth factor (EGF). Their pump-driven microfluidic chip enabled to optically monitor cellular responses at single-cell resolution. Differential pathway activation was detected in an exposure-profile-dependent manner. The application of such pump-driven systems, however, requires technically experienced operators, which limits their broad use, experimental throughput, and the transfer of such systems to nonexpert labs.

Another approach for pulsatile substance exposure of cellular models, was realized by relying on passive, gravity-driven perfusion¹⁵. The proposed microfluidic chip was connected to two inlet reservoirs at different heights, one filled with medium, and the other one filled with substance-containing medium. In their work, the authors cultured cancer cells in a microfluidic chip and exposed them to pulses of tumor necrosis factor (TNF). Pulses were initiated by manually elevating the reservoir containing the substance for the duration of the pulse. Interestingly, their results evidenced higher anticancer effects for using shorter pulses of TNF, which underline the importance of investigating dosage-dependent toxicity and efficacy. The system, however, was only used to generate pulses of TNF, and gradual concentration changes over time were not realized. The system presented here, on the other hand, can be used to produce gradual changes of substance concentrations without the need for manual actuation, while still fully relying on gravity-driven operation. It can be used with a minimum set of specialized equipment. Furthermore, in contrast to other systems, which were designed for culturing 2D monolayers of cells, our chip was devised to culture multiple 3D MTs.

Combining a controlled microfluidic environment with 3D cell culture techniques to enable the realization of PK profiles and modification of the respective parameters, we see great potential for our design for investigating concentration profile-dependent efficacy and/or toxicity of substances.

4.5.1 Future Perspective

As shown in the presented experiments, different concentration profiles could be produced in the microfluidic chip, and tumor MTs could be exposed to dynamically changing concentrations profiles. So far, the chip was used for experimentation with only one type of MTs. The chip, however, is not limited to a single organ surrogate, but also allows for combining several different MTs or organ types. The behavior of different organs upon substance exposure can be monitored simultaneously, which allows for a combined readout of efficacy on the primary target organ and toxicity on a secondary organ. For mimicking cancer treatment, tumor MTs and liver MTs could be combined to assess the side effects of tumor treatment on the liver. The developed device could help to experimentally modify the dosing curve in order to find a dosing strategy with an optimum trade-off between efficacy on the tumor and liver toxicity. Moreover, communication between the two tissue types through secreted molecules, which might further influence their drug and treatment response, could be included in *in-vitro* testing.

In addition to the presented concentration profiles, more complex dosing profiles could be approximated by applying a sequence of different tilting angles and precisely timed medium changes in the reservoirs. We could produce a concentration profile that features the characteristics of a typical plasma concentration over time upon oral administration of a substance²⁵, as we have demonstrated by using amaranth red dye as drug-surrogate (Figure 7). A sequence of precisely timed medium exchanges, or the implementation of capillary stop valves that burst when sufficient pressure is built up at high tilting angles^{30, 31} can be used over longer culturing periods to reproduce long-term substance fluctuations, e.g., repeated drug dosing or circadian hormone profiles. Alternating filling of the reservoir connected to the narrow channel with hormone-containing and plain medium could be used to gradually increase and decrease hormone concentrations in the MT compartments. Since circadian profiles modulate organ functions, they may play an important role in future substance testing and for translating of *in-vitro* organ responses to *in vivo* conditions³².

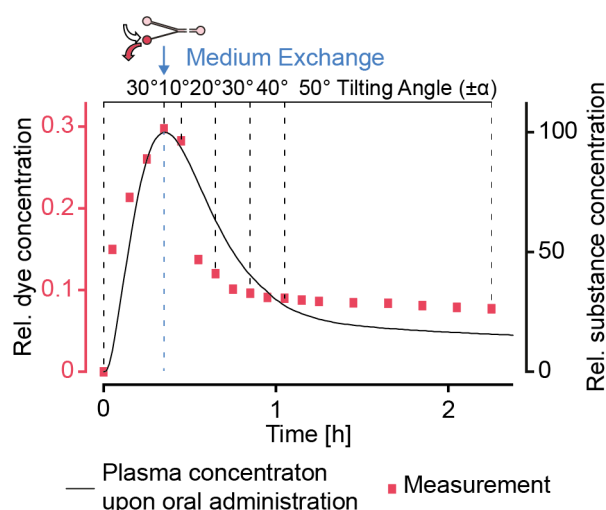


Figure 7: Realization of more complex dosing profiles. A typical concentration profile [Kwon, 2001] upon oral administration of a substance could be approximated by using a sequence of different tilting angles. A medium exchange to replace the substance-loaded medium in the reservoir connected to the narrow channel with plain medium was performed after approx. 20 min. Amaranth red dye was used as drug-surrogate.

4.6 Conclusion

In this article, we presented a novel microfluidic design for the generation of gradually changing substance concentration profiles for an easy-to-use microfluidic tilting system. The integration of the new design into cell culture chips enabled to run dynamically changing concentration profiles and to reproduce, e.g., the dosing curve upon injection of a substance without the need for a series tedious pipetting steps or expensive pumping equipment. By changing design and operation parameters, the dosing curves could be adjusted to experimenters needs, and the dosing curves could be modulated on demand as demonstrated by recreating an oral uptake

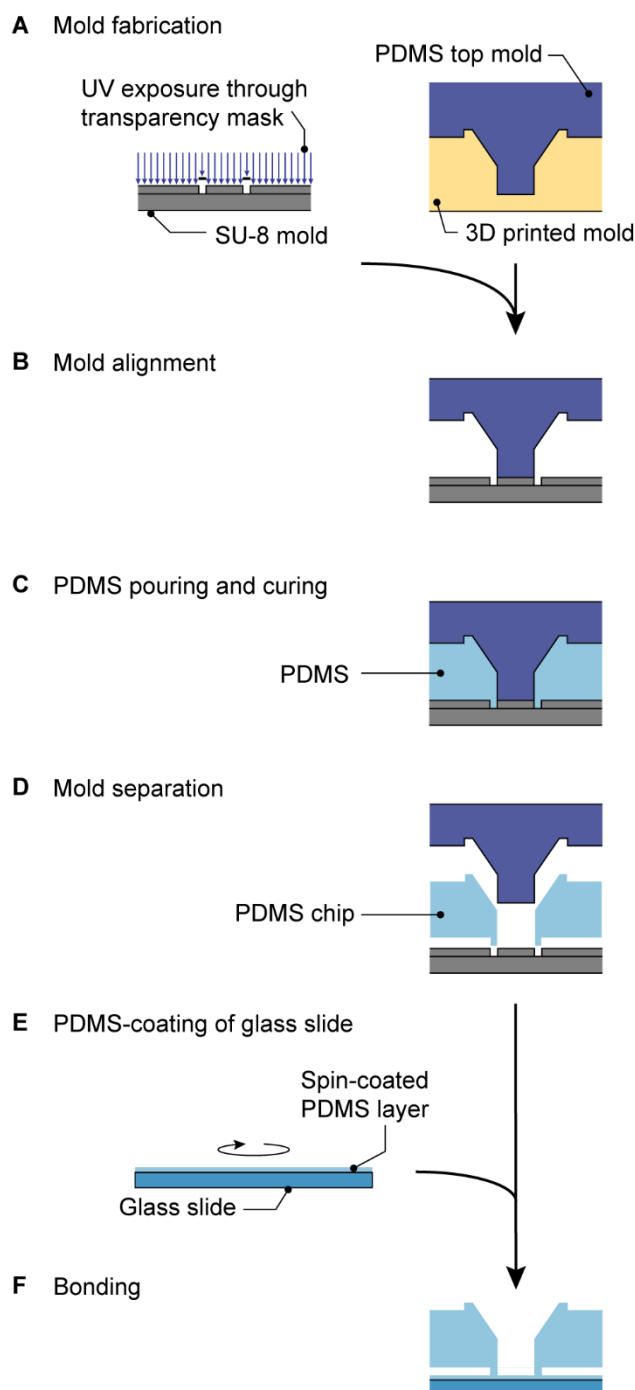
profile. Experiments with colorectal tumor MTs and the cytotoxic substance Staurosporine showed the different short- and long-term responses of the MTs to dynamic and traditional, linear dosing regimes.

4.7 Acknowledgements

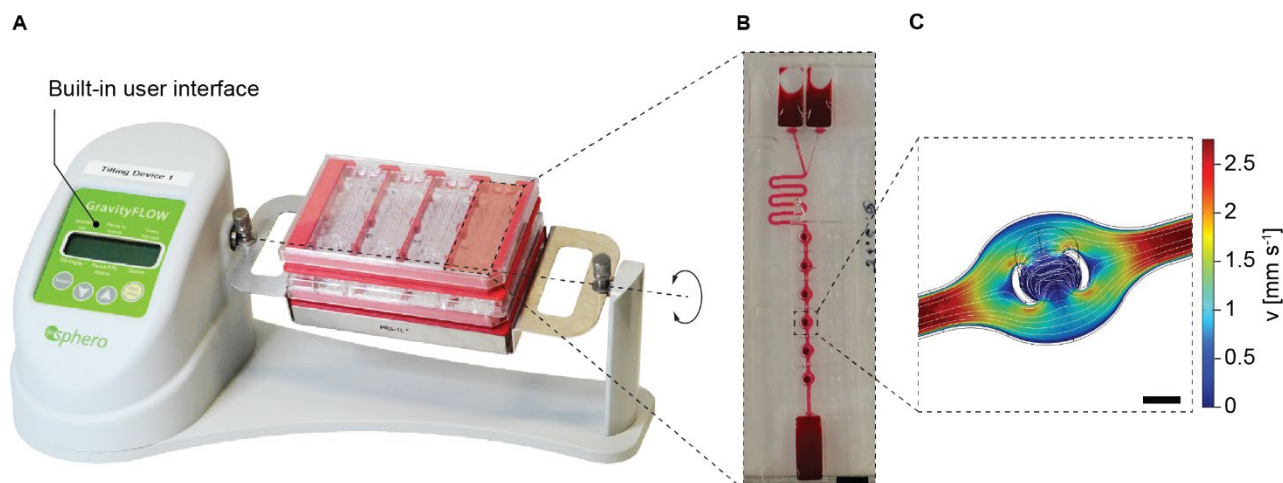
This work was financially supported by CTI grant 18024.1 PFLS-LS.

4.8 Supporting Information

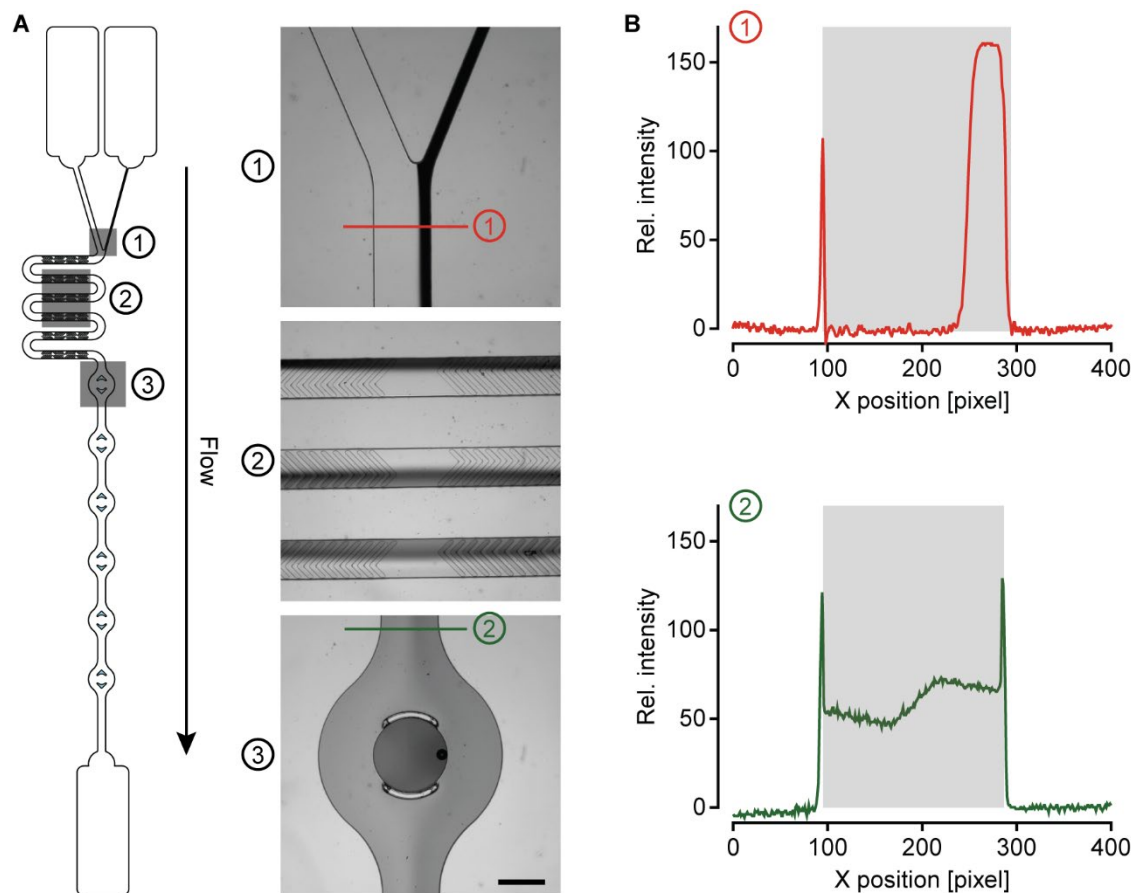
4.8.1 Supplementary Figures



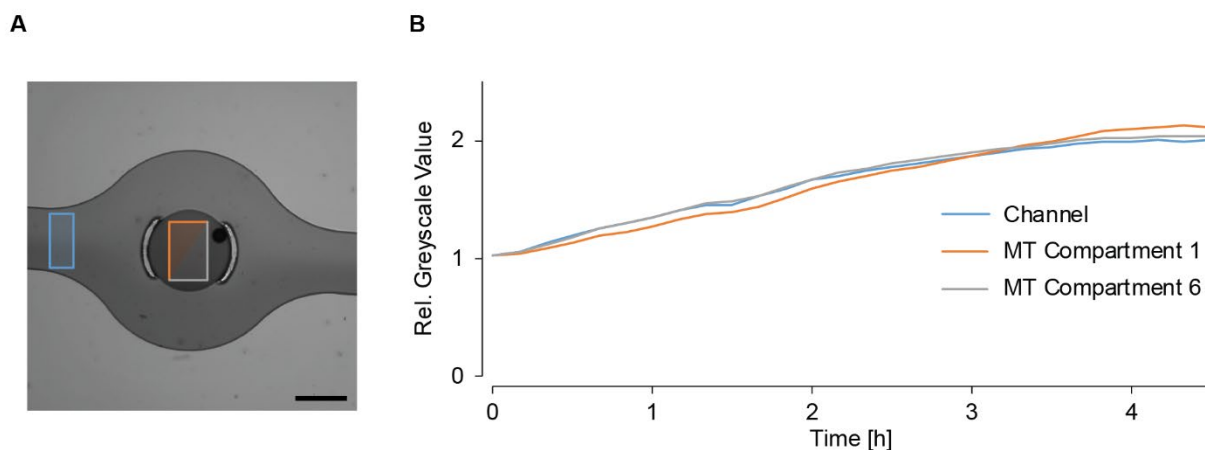
Supplementary Figure 1: Fabrication of the microfluidic chip exemplified for a MT compartment. **(A)** An SU-8 bottom mold was fabricated using standard photolithography methods, and a PDMS top mold was casted using a 3D-printed mold. **(B)** The bottom and top molds were aligned, and **(C)** liquid PDMS was poured between them. **(D)** After PDMS curing, the re-usable molds were separated. **(E)** Microscopy glass slides were spin-coated with a uniform PDMS layer, and **(F)** the chips were O₂-plasma-bonded onto those slides.



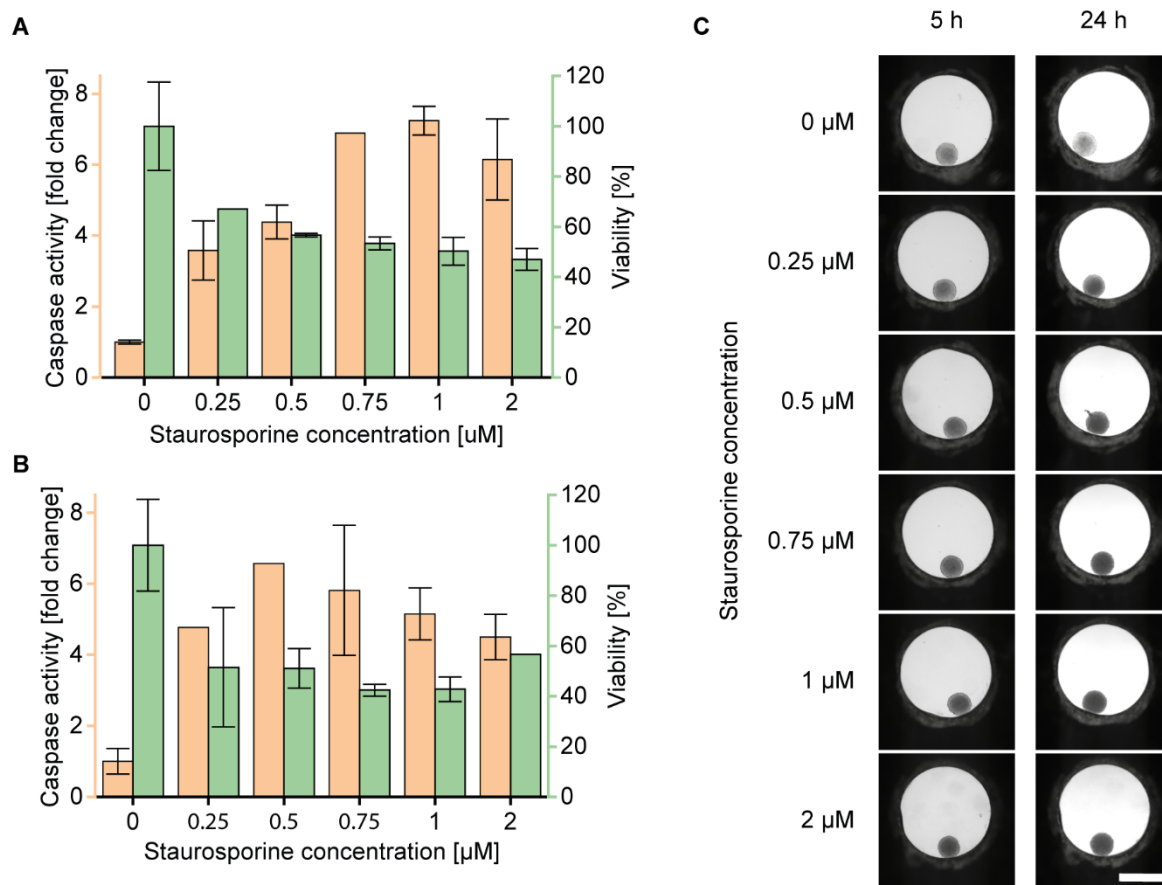
Supplementary Figure 2: Operation of the microfluidic microtissue culture chip by tilting. **(A)** Four chips are assembled in a handling frame, and several handling frames can be stacked onto a programmable tilting stage with a built-in user interface that allows for setting tilting angles, duration of the resting times at tilted positions, and the transition times between positive and negative tilting angles. **(B)** Image of a chip on the tilting stage. Channels of the chip were filled with dye for illustration (scale bar = 5 mm). **(C)** Assessment of the liquid velocity around the microtissue compartment to estimate shear stress and compound delivery into the MT compartment at a flow rate of $10 \mu\text{L min}^{-1}$. Stream lines indicate mass transport of biomolecules into the MT compartment (scale bar = 500 μm).



Supplementary Figure 3: Efficiency of the mixing element in the microfluidic chip. **(A)** Microfluidic channel layout and microscopy bright-field images of the indicated positions. An amaranth red-dye solution was flushed through the narrow channel, while water was flushed through the other one. Along the mixing structure, the two liquid phases mix, before they reach the microtissue compartments (scale bar: 500 μm). **(B)** Relative greyscale intensity along the indicated lines in the microscopy images. After the mixing structure, amaranth red dye was homogeneously distributed across the entire channel width.



Supplementary Figure 4: Concentration change within the channel and the MT compartments over time. **(A)** Microscopic image of a MT compartment under perfusion with amaranth red dye and water from two separate inlets (see also Supplementary Movie 1). Rectangles indicate regions of interest for the channel and the MT compartments (scale bar: 500 μm). **(B)** Normalized mean grey-scale values in the channel, the first MT compartment, and the last MT compartment along the perfusion direction over time as an indicator for changing dye concentrations. The amaranth red concentration is steadily increasing over time, while the flow rate was kept constant at 15 $\mu\text{L min}^{-1}$. Images were taken at 10 min intervals.



Supplementary Figure 5: Titration of Staurosporine with TuMTs under static conditions in a 96-well microtiter plate. Caspase 3/7 activity and ATP-dependent viability were measured **(A)** 5 h and **(B)** 24 h after treatment start. A dose-dependent increase of caspase induction and a decrease of viability could be observed up to a dose of 0.75 μM . Higher doses resulted in a response similar to 0.75 μM (data represented as mean \pm SD). **(C)** Images of TuMTs appear darker and denser upon Staurosporine treatment, slight disintegration is observed after 24 h (scale bar: 500 μm).

4.8.2 Supplementary Movies

Supplementary Movie 1: Different regions of the microfluidic chip under perfusion with amaranth red dye and water from two separate inlets. The amaranth red concentration is steadily increasing over time, while the flow rate was kept constant at 15 $\mu\text{L min}^{-1}$. Images were taken at 10 min intervals.

4.9 References

1. Marx, U., et al., Biology-inspired microphysiological system approaches to solve the prediction dilemma of substance testing. *ALTEX*, **33**, 272-321 (2016).
2. Zhang, B.Y., et al., Advances in organ-on-a-chip engineering. *Nature Reviews Materials*, **3**, 257-278 (2018).
3. Wang, Y.I., et al., Multiorgan Microphysiological Systems for Drug Development: Strategies, Advances, and Challenges. *Adv Healthc Mater*, **7**, (2018).
4. Saif, M.W., et al., Pharmacokinetically Guided Dose Adjustment of 5-Fluorouracil: A Rational Approach to Improving Therapeutic Outcomes. *JNCI: Journal of the National Cancer Institute*, **101**, 1543-1552 (2009).
5. Sejoong, K., et al., Pharmacokinetic profile that reduces nephrotoxicity of gentamicin in a perfused kidney-on-a-chip. *Biofabrication*, **8**, 015021 (2016).
6. Tsaion, K., B.J. Blaauboer, and T. Hartung, Evidence-based absorption, distribution, metabolism, excretion (ADME) and its interplay with alternative toxicity methods. *ALTEX*, **33**, 343-358 (2016).
7. Sung, J.H., C. Kam, and M.L. Shuler, A microfluidic device for a pharmacokinetic-pharmacodynamic (PK-PD) model on a chip. *Lab Chip*, **10**, 446-455 (2010).
8. Maass, C., et al., Multi-functional scaling methodology for translational pharmacokinetic and pharmacodynamic applications using integrated microphysiological systems (MPS). *Integrative biology : quantitative biosciences from nano to macro*, **9**, 290-302 (2017).
9. Edington, C.D., et al., Interconnected Microphysiological Systems for Quantitative Biology and Pharmacology Studies. *Sci Rep*, **8**, 4530 (2018).
10. Prantil-Baun, R., et al., Physiologically Based Pharmacokinetic and Pharmacodynamic Analysis Enabled by Microfluidically Linked Organs-on-Chips. *Annual review of pharmacology and toxicology*, **58**, 37-64 (2018).
11. Wikswo, J.P., Markov, Dmitry A., Samson, Philip C., Block III, Frank E., Schaffer, David K., Reiserer, Ronald S., Interconnections of multiple perfused engineered tissue constructs and microbioreactors, multi-microformulators and applications of the same. Vanderbilt University (Nashville, TN, US): United States. (2018)
12. Kim, Y., et al., Detection of Dynamic Spatiotemporal Response to Periodic Chemical Stimulation in a *Xenopus* Embryonic Tissue. *PLOS ONE*, **6**, e14624 (2011).

13. Ross, A.E., et al., Spatially resolved microfluidic stimulation of lymphoid tissue ex vivo. *Analyst*, **142**, 649-659 (2017).
14. Song, J., et al., Microfluidic platform for single cell analysis under dynamic spatial and temporal stimulation. *Biosensors and Bioelectronics*, **104**, 58-64 (2018).
15. Lee, R.E.C., et al., NF- κ B signalling and cell fate decisions in response to a short pulse of tumour necrosis factor. *Scientific Reports*, **6**, 39519 (2016).
16. Lohasz, C., et al. A Tubing-Free, Microfluidic Platform for the Realization of Physiologically Relevant Dosing Curves on Cellular Models. in *Euroensors*. Paris.(2017)
17. Kim, J.Y., et al., 96-well format-based microfluidic platform for parallel interconnection of multiple multicellular spheroids. *J Lab Autom*, **20**, 274-282 (2015).
18. Lohasz, C., et al., Scalable microfluidic platform for flexible configuration of, and experiments with microtissue multiorgan models. *SLAS Technology*, (2018).
19. Karaman, M.W., et al., A quantitative analysis of kinase inhibitor selectivity. *Nature Biotechnology*, **26**, 127 (2008).
20. Bruus, H., Theoretical microfluidics. Vol. 18. Oxford: Oxford University Press.(2008)
21. Lee, S.W. and S.S. Lee, Shrinkage ratio of PDMS and its alignment method for the wafer level process. *Microsystem Technologies*, **14**, 205-208 (2008).
22. Lee, C.-Y., et al., Microfluidic Mixing: A Review. *International Journal of Molecular Sciences*, **12**, 3263-3287 (2011).
23. Stroock, A.D., et al., Chaotic mixer for microchannels. *Science*, **295**, 647-651 (2002).
24. Kim, J.Y., et al., 3D spherical microtissues and microfluidic technology for multi-tissue experiments and analysis. *J Biotechnol*, **205**, 24-35 (2015).
25. Kwon, Y., Handbook of essential pharmacokinetics, pharmacodynamics and drug metabolism for industrial scientists. New York: Springer Science & Business Media.(2001)
26. Casale, F., et al., Plasma concentrations of 5-fluorouracil and its metabolites in colon cancer patients. *Pharmacological Research*, **50**, 173-179 (2004).
27. Chae, H.-J., et al., Molecular mechanism of staurosporine-induced apoptosis in osteoblasts. *Pharmacological Research*, **42**, 373-381 (2000).
28. ANSI/SLAS, ANSI/SLAS 4-2004: Microplates - Well Positions. (2004)
29. ANSI/SLAS, ANSI/SLAS 1-2004: Microplates - Footprint Dimensions. (2004)

30. Olanrewaju, A.O., et al., Autonomous microfluidic capillarie circuits replicated from 3D-printed molds. *Lab Chip*, **16**, 3804-3814 (2016).
31. Olanrewaju, A., et al., Capillary microfluidics in microchannels: from microfluidic networks to capillarie circuits. *Lab Chip*, **18**, 2323-2347 (2018).
32. Cyr, K.J., O.M. Avaldi, and J.P. Wikswo, Circadian hormone control in a human-on-a-chip: In vitro biology's ignored component? *Experimental Biology and Medicine*, **242**, 1714-1731 (2017).

5 CONCLUSION

The combination of 3D microtissues with microfluidic technology provides a robust and flexible methodology to investigate complex *in vivo* processes involving multiple organs. Gravity-driven perfusion renders the technology robust and scalable for a transfer to industrial settings.

Enabling design features

A very important feature that is preserved across the developed platforms and applications is the operation by means of gravity-driven perfusion. Gravity-driven perfusion is induced by a motion stage that periodically tilts the culture platform back and forth. The flow rates in the device can be predicted with numerical simulations and can be controlled by adjusting the tilting angle of the platform. Furthermore, the closed-loop characteristics of the platform enable the time-dependent enrichment of soluble factors that need to exceed certain threshold concentrations to trigger biological effects or to become measurable through analytical methods.

The semi-open design of the microfluidic channels and the microtissue compartments promotes bubble-free filling of the channels, which is crucial for robust operation of the platform. All microtissue compartments are open and accessible directly from the top, which facilitates the loading of MTs and their harvesting for downstream analyses with standard pipetting equipment. Further, all MT compartments are optically accessible, so that the status of the MTs can be monitored non-invasively by using microscopy. The open reservoirs on both sides of the microfluidic channel allow for periodic sampling of the cell culture supernatant to quantify secreted molecules and metabolites.

This thesis presented the development, characterization and application of gravity-driven microfluidic platforms and included (i) a robust device for the culturing of multiple 3D MTs, (ii) the use of this device to monitor organ interactions under drug exposure, and (iii) the development of a modified channel structure to enable dynamic drug exposure scenarios.

Scalable, microfluidic multi-organ system

A polystyrene-based microfluidic platform for the culturing of multiple 3D MTs was presented. Ten microtissue compartments were integrated along a channel, which ended in medium reservoirs at both ends. Polystyrene as primary material featured low ad- and absorption of hydrophobic molecules in comparison to similar platforms fabricated in PDMS, so that reliable quantitative measurement could be conducted. Compliance of MT compartment locations on the platform with ANSI/SLAS standard well-plate formats supported the automation of the MT loading process using liquid handling robots.

Human liver MTs and cell-line-based tumor MTs were cultured and monitored in the chip. Both MT types remained functional over at least seven days in single-organ and multi-organ configurations. Non-invasive analysis methods, such as light and fluorescence microscopy at single-cell resolution and off-chip analysis of secreted molecules in the cell-culture supernatant, were used. Further, individual MTs could be harvested from the chip for endpoint assays.

The robust and scalable platform offers the potential to cultivate arrays of identical or different MTs over extended periods. To monitor the state of these MTs, a wide range of non-invasive and invasive readouts can be used. The platform can be used to investigate complex biological processes involving the interaction of multiple organs. The possibility to establish series production of the chip by injection molding and the high experimental throughput due to parallelization of the experiments render the platform suitable for substance testing in industrial settings.

Prediction of drug-drug interactions

The chip described in the previous chapter was used in a multi-organ configuration to assess for tissue-tissue interaction upon drug treatment. Anticancer prodrugs were used to demonstrate the importance of hepatic metabolism to release the corresponding pharmaceutically active metabolites.

Primary human liver MTs and tumor MTs were cultured in the microfluidic chip over up to 14 days. Drug combinations including anticancer prodrugs were administered to the system and alterations of the hepatic metabolism and, thus, of the prodrug efficacy were assessed. Drug-

drug interactions for distinct drug combinations were shown through (i) the analysis of the cell-culture supernatant, which revealed changed metabolization properties of the liver MTs; and through (ii) the decreased efficacy of the anticancer treatment, which was detected by imaging-based size measurements of the tumor MTs. Furthermore, changed growth dynamics of the tumor MTs upon drug treatment allowed for an estimation of the severity of drug-drug interactions for the corresponding drug combinations.

In the presented study, we could show that our microfluidic cell-culture platform enabled the communication between different organ types. As the platform facilitates multi-organ configurations, it can help to better characterize potential drugs and administration regimens, especially in cases of combination therapies that involve multiple pharmaceutically active compounds.

Pharmacokinetic drug dosing system

In the last chapter, we described a modification of the channel design, which allowed for the exposure of MTs to physiologically relevant drug dosing scenarios. Pharmacokinetic concentration curves could be generated without the use of external pumps.

Key to the generation of pharmacokinetic concentration curves was the implementation of an asymmetric Y-junction on one side of the chip, and the introduction of a third reservoir connected to the microfluidic channel. The different dimensions of the channels connected to the Y-junction resulted in different hydraulic resistances. The higher hydraulic resistance of the thinner channel caused, e.g., a stepwise release of a drug into the cell culture medium with each tilting cycle. Repeated tilting resulted in a gradual enrichment or dilution of a drug over time depending on which channel was used for drug and/or medium. The dynamics of the concentration changes could be modulated by altering the channel dimensions, the volumes in each medium reservoir, or the tilting angles. Tumor MTs were cultured in the chip and exposed to *in vivo*-like concentration profiles that were similar to those upon intravenous administration of a substance. Different short- and long-term responses of tumor MTs to dynamic dosing regimens of Staurosporine were observed in comparison to those obtained with conventional, linear dosing regimens.

The study showed that carefully designed channel structures can expand the application range of gravity-driven perfusion systems. Modifications of the channel path and resistance can be

used to precisely determine the fluid flow through the channel. This knowledge can be used for other cell-culturing scenarios, in which flow conditions and precise timings of drug dosage play a major role.

In this thesis, I presented the design and application of two microfluidic platforms, which rely on gravity-driven perfusion. The presented platforms were characterized and validated before they were used for proof-of-concept studies that addressed current needs in *in vitro* drug testing. The platforms were specifically designed for the parallelized culturing of interconnected 3D microtissues and for use with a wide range of analytical methods. The modular and flexible nature of the platform and the straightforward microtissue generation render the presented approach widely applicable in drug testing settings, even for rather complex biological scenarios.

6 OUTLOOK

The presented gravity-driven microfluidic systems offer a straightforward method for interconnecting multiple 3D microtissues under perfusion conditions. In this thesis, the platform was used for drug-exposure experiments with primary human liver microtissues and cell line-derived tumor microtissues.

The current chip designs were optimized for the culturing of spherical 3D microtissues. These microtissues can be used to mimic a wide range of organs in *in vitro* experiments. Other organs of the human body, however, may require different arrangements and culturing methods to maintain their physiological function in culture. Barrier tissues, e.g., lung, intestines, or vasculature rely on cell monolayer architectures. The immune system, on the other hand, includes single, free-floating cells. Future chip development will focus on compartment and channel designs that allow for incorporation and addition of organ models with specific culture requirements. The inclusion of such designs will bring the platform a step closer to a so-called “body-on-a-chip” device, which encompasses the most relevant organs of a human body in order to mimic human physiology as closely as possible.

The analysis of microtissue status and functionality in the presented systems was mostly based on microscopy and imaging, the analysis of the cell-culture supernatant upon sampling, and lytic endpoint analyses of the microtissues themselves. To ensure constant culture conditions, interruptions of gravity-driven perfusion for imaging and sampling purposes were kept as short as possible and were performed only as frequently as needed. Consequently, there may be large time stretches between subsequent measurements. Integration of on-line electrochemical sensors into the chip could massively increase the temporal resolution of the measurements. Electrical impedance measurements can be used to assess microtissue sizes, while biochemical sensors can be used to assess their metabolism. Such sensors could close the gaps between subsequent measurement points and provide valuable real-time information.